MULTIVARIATE SIGNAL PROCESSING AND THEORETICAL MODELING FOR THE STUDY OF GASTROINTESTINAL BIOELECTROMAGNETISM

By

Andrei Irimia

Dissertation
Submitted to the Faculty of the
Graduate School of Vanderbilt University
in partial fulfillment of the requirements
for the degree of

DOCTOR OF PHILOSOPHY

in

Physics

December 2007

Nashville, Tennessee

Approved:

Leonard A. Bradshaw

Charles A. Brau

William O. Richards

Richard G. Shiavi

John P. Wikswo, Jr.

The effort to understand the universe is one of the very few things that lifts human life above the level of farce, and gives it some of the grace of tragedy.

Steven Weinberg

ACKNOWLEDGMENTS

Many thanks to my advisors, L. Alan Bradshaw, William O. Richards and John P. Wikswo, Jr. for their continuous guidance, support, encouragement and understanding throughout my graduate years. I would also like to thank my other defense committee members, Drs. Charles A. Brau and Richard G. Shiavi for their useful suggestions and for their encouragement and support. I am very grateful to Michael R. Gallucci for building our GIST Laboratory, our SQUID facilities and for his intense and extremely useful efforts that he provided for data analysis. I am grateful to the Graduate School of Arts and Sciences, to the VIIBRE Institute and to the New England Complex Systems Institute for covering travel expenses to Boston for the NECSI 2006 Conference. Don Berry, Cheryl Cosby, Christy Hinkle, Christie Nichols, Allison Price provided essential support. I also wish to thank Phil Williams and Amy Grant from the Surgical Research Division at the Vanderbilt University Medical Center for their advice and assistance regarding our animal experiments. Richard A. Gray from the Department of Biomedical Engineering at the University of Alabama at Birmingham provided insightful suggestions regarding the nonlinear dynamics portion of this dissertation. I am grateful to Providence, to my family and to the University for providing me with the opportunity of pursuing this degree. Research funding was provided by NIH grants R01 DK58697 and DK58197.

LIST OF PUBLICATIONS

The following publications were based on the material included in the present dissertation.

[1] A Irimia, LA Bradshaw 2004 Theoretical ellipsoidal model of gastric electrical control activity propagation *Phys Rev E* **68** 051905

[2] A Irimia, LA Bradshaw 2004 Theoretical and computational methods for the noninvasive detection of gastric electrical source coupling *Phys Rev E* **69** 051920

[3] A Irimia, JJ Beauchamp, LA Bradshaw 2004 Theoretical and computational multiple regression study of gastric electrical activity using dipole tracing from magnetic field measurements *J Biol Phys* **30** 239-259

[4] A Irimia 2005 The electric field and potential due to a bioelectric current dipole in an ellipsoid *J Phys A* **38** 8123-8138

[5] A Irimia, LA Bradshaw 2005 Ellipsoidal electrogastrographic forward modelling *Phys Med Biol* **50** 4429-4444

[6] A Irimia, LA Bradshaw 2005 Artifact reduction in magnetogastrography using fast independent component analysis *Physiol Meas* **26** 1059-1073

[7] A Irimia, WO Richards, LA Bradshaw 2006 Magnetogastrographic detection of gastric electrical response activity in humans *Phys Med Biol* **51** 1347-1360

[8] LA Bradshaw, A Irimia, JA Sims, MR Gallucci, RL Palmer, WO Richards 2006 Biomagnetic characterization of spatiotemporal parameters of the gastric slow wave *Neurogastroenterol Motil* **18** 619-631

[9] EA Lima, A Irimia, JP Wikswo 2006 The magnetic inverse problem *The SQUID Handbook vol II* (Clarke & Braginski eds) Wiley-VCH 139-267

[10] A Irimia, MR Gallucci, WO Richards, LA Bradshaw 2006 Separation of gastric electrical control activity from simultaneous MGG/EGG recordings using independent component analysis *Proc IEEE EMBS Int Conf New York* 3110-3113

[11] A Irimia 2006 Combinatorial formulae for the differentiation of Lamé functions *Appl Math Comput* **182** 1501-1508

[12] A Irimia, MR Gallucci, JP Wikswo 2006 Comparison of chaotic biomagnetic

field patterns recorded from the arrhythmic heart and stomach *Proc 6th Int Conf Complex Sys Boston Mass* 1-9

[13] A Irimia 2007 Formulae and algorithms for the analytic differentiation of factorized polynomials *Centr Eur J Math* in press

[14] A Irimia 2007 Calculation of the magnetic field due to a bioelectric current dipole in an ellipsoid *Math Appl* in press

[15] A Irimia 2007 Integration of the ellipsoidal surface normalization functions *J Math Anal Appl* in press

[16] A Irimia, WO Richards, LA Bradshaw 2007 Comparison of conventional filtering and independent component analysis for artifact reduction in simultaneous gastric electromyography and magnetogastrography *Physiol Meas* in press

[17] A Irimia, MR Gallucci, WO Richards, LA Bradshaw, JP Wikswo 2006 Biomagnetic procedure for the noninvasive diagnosis of chronic mesenteric ischemia *to be submitted*

[18] KR Swinney, A Irimia, JP Wikswo 2006 The partial independence of the electric and magnetic fields of current sources in conducting media *to be submitted*

[19] A Irimia, JP Wikswo, WO Richards, LA Bradshaw 2006 Gastrointestinal circulatory arrhythmias are associated with significant fluctuations in chaotic attractor dimensionality *to be submitted*

TABLE OF CONTENTS

LIST OF TABLES

LIST OF FIGURES

CHAPTER I

INTRODUCTION

Basic Electrophysiology

It is well known that the fundamental constituents of mammalian cells are the membrane, cytoplasm, and organelles, including the nucleus. The cell membrane consists of a sheetlike phospholipid bilayer, which is two molecule thick. The bilayer acts as an impermeable barrier that prevents the diffusion of water-soluble solutes across the membrane. Embedded in the membrane are ion channels, which are proteins that help establish and control the voltage gradient across the plasma membrane by allowing the flow of ions down their electrochemical gradient. The interior of the cell contains a large number of negatively charged proteins which cannot exit the cell due to their size. Inside the cell there is also a high concentration of K^+ ions and a low concentration of Na^+ ions, while the reverse is true for the cell's exterior. Because of this, a steady in-flux of sodium ions and out-flux of potassium ions exists via specific sodium and potassium ion channels, respectively. To maintain the resting potential, the cell operates Na-K pumps, which use energy to move rougly 3 sodium ions out of the cell for every 2 potassium ions transferred into the cell. In the steady state, the membrane resistance to potassium currents is about thirty times small than the resistance to sodium currents. However, because the force on potassium ions is one thirtieth of the force on sodium ions, a balance is maintained across the membrane.

The transmembrane resting potential of a typical muscle cell is in the range of -70 to -90 mV, hence there is an excess of negative charge inside the membrane and an excess of positive charge outside. The electric field in these two regions vanishes due to the cancellation effect, but within the membrane a field of the order of 10^6 V/m is established as a result of the transmembrane potential.

Of great importance in electrophysiology is the phenomenon of cellular depolarization. This occurs when a mechanical, electric or chemical stimulus induces conformational changes in the gating proteins of the cell. For example, when the potential is raised above a certain threshold (called the stimulation threshold), a conformational change is triggered and the membrane permeability to sodium ions is increased by about two orders of magnitude. This causes a large influx of sodium ions into the cell and thus the membrane potential increases significantly. The region of the cell where this occurs is said to be depolarized.

Complementary to depolarization is the phenomenon of repolarization. About a milisecond after depolarization, sodium ion channels close and thus sodium permeability decreases to the point that no sodium ions can enter the cell any further. In certain cells (such as cardiac or gastrointestinal cells), a secondary inward current of calcium ions is activated at this point via calcium channels, creating an inward current leading to a long depolarization plateau. Finally, a conformational change in the potassium channels allows them to open. Thus, sufficient K^+ can leave the cell so that the transmembrane potential can return to approximately its original value. The remaining imbalance of ions is corrected by the Na-K pump. Because the repolarization currents are about one hundred times weaker than the depolarization currents, the repolarization of the membrane lasts about one hundred times longer than its depolarization.

The depolarization/repolarization front can travel along the membrane and it is called a propagating action potential. Once a stimulus activates the depolarization phase, the passive voltage can only be conducted for a short distance before being shorted out by the leakage pathways of the membrane. This is why, for example, the propagation of gastric or intestinal action potentials is dependent on the presence of an external stimulation source which allows the action potential to travel along the entire cell. In the case of the gastrointestinal (GI) tract, this stimulation source consists of the so-called interstitial cells of Cajal (ICCs).

To explain how ICCs mediate the propagation of the action potential, it is necessary to introduce the concept of intercellular gap junctions. A gap junction (also called a nexus) is a junction between adjacent cells which allow molecules and ions to pass freely from one cell to the next. Groups of cells connected by gap junctions form what is called a syncytium. A junction typically consists of connexins (gap junction proteins) which achieve intercellular coupling by allowing certain ions to pass from one cell to another when they are in certain configurations. These configurations are induced by chemical or electrical stimuli that lead to conformational changes in the connexin structure.

ICCs are stellate cells with long branched processes that are positioned between the smooth muscle layers of the GI tract. When they were first discovered, they were even thought to be special types of interstitial neurons due to their neuron-like appearance. The long processes of the ICCs allow them to spawn smooth muscle layers in all three spatial directions, which makes them ideal initiators and propagators of gastric electrical activity. ICCs have numerous, large mitochondria located in the processes and a high density of gap junctions that connect them to smooth muscle cells. Along the GI tract, there can be as many as four distinct ICC layers, which are positioned between consecutive layers of smooth muscle. Thus, ICCs form a three-dimensional network that initiate and propagate electrical activity in the gut.

Essential for understanding how electrical activity is initiated in the stomach is the pacemaker concept. A pacemaker is a group of cells that together set the pace of electrical activity. The gastric pacemaker exhibits automaticity, just as in the cardiac case. In the stomach, the ICC pacemaker generates small membrane potential oscillations which spread three-dimensionally along both circular and longitudinal muscle layers.

The mechanism behind the activation of gastric electrical activity relies on the fact that, at the resting potential values of the smooth muscle cells, ICCs can still be activated whereas the muscle cells themselves cannot. In other words, the activation threshold of the ICCs is lower than that of the muscle cells. This is because ICCs contain low-threshold Ca^{2+} channels that allow calcium to be released in the extracellular space. As mentioned before, ICCs have numerous and large mitochondria located along their processes. When inositol triphosphate (IP_3 − a messenger molecule used for signal transduction in the cell) binds to mitochondrial membranes, calcium is released from these organelles into the cytoplasm and then to the exterior of the cell. This phenomenon is periodic in nature and it is responsible for GI autorhythmicity.

ICC membranes have a resistance of approximately $10^9\Omega$, whereas that of smooth muscle cells is about 10^5 times lower. Because of the very high ICC membrane resistance, a very feeble current due to calcium channels induces significant cellular depolarization in the ICCs. This leads to an extracellular current that finally reaches the activation threshold required for smooth muscle cell depolarization. Once this has been accomplished, the repolarization plateau of the muscle cells is sustained by the outflux of Ca^{2+} ions from ICC network and absorption of these ions by the muscle cells. After the plateau phase, the potassium channels of the muscle cells allow enough positively charged ions to leave the cell such that the resting potential is restored. However, this outflux of K^+ ions activates the adjacent series of ICCs along the body of the stomach, which in their turn lead to the depolarization of smooth muscle cells located farther and farther away from the original activation site of the pacemaker.

In this fashion, electrical activity is propagated along the syncytium of the stomach and then along the entire GI tract.

Gastrointestinal Electrical Activity

The study of the electrical control activity (ECA) in the stomach is of great interest in the medical field due to the possibility to detect various pathological conditions of this organ from the analysis of gastrointestinal slow wave signals. Although over 60 million Americans are affected by digestive diseases [50], the electrophysiological mechanisms associated with pathological conditions in the gastrointestinal system are only beginning to be understood. One such condition is gastroparesis, which is characterized by abnormally slow gastric emptying rates, dyspepsia, nausea, discomfort and intermittent vomiting [100, 130]. In the past, numerous investigations were carried out to detect phenomena associated with diseases such as gastroparesis and ischemia using the electrogastrogram (EGG) and magnetogastrogram (MGG). Thus, the EGG and MGG are the two most important procedures for measuring and quantifying GEA. Given that the mortality rate of patients suffering from acute mesenteric ischemia−including mesenteric venous thrombosis (MVT)−is at least 50%, the importance of such studies cannot be understated. As explained in the previous section, the peristaltic waves that arise in the muscle tissue layers of the GI tract are produced by the interaction of the enteric nervous system, the interstitial cells of Cajal (ICC) and the smooth muscle cells [138]. Pacemaker ICCs are located within the the Auerbachs plexus, a group of ganglion cells between the circular and longitudinal layers of the *muscularis externa* in the digestive tract. Approximately every 20 seconds, the ICC spontaneously depolarize to initiate the gastric slow wave. Once initiated by the ICC, electrical activity is conducted from fibre to fibre throughout the body of the stomach; muscular contractions are associated with the electrical response activity

(ERA), which is triggered by the depolarization of the cell membrane above threshold [78]. Thus, in humans, GEA consists of an electrical control activity (ECA) that can be recorded as an electrical slow wave and an electrical response activity (ERA) that is characterized by spiking potentials during the plateau phase of the ECA. Because of volume-conductor smoothing of intracellular potentials and sequential phase shifts between adjacent cells, the waveform of the cutaneous EGG waveform resembles a sinusoid.

The transmembrane potentials produced by coupled cells in smooth muscle give rise to dipole moments that vary in frequency and phase according to their anatomical position and configuration, reflecting the fact that slow wave frequencies are location dependent along the GI tract [157, 185]. These slow wave variations in their own turn produce magnetic fields, which can be recorded experimentally. Studies have shown that analyzing these magnetic fields can be useful in detecting pathological states of the stomach in human patients. Moreover, the experimental and computational task of identifying sources of electric current in the GI tract is important because it can allow such conditions to be identified noninvasively.

The gastric slow wave, first recorded in 1921 by Alvarez [6], moves in the direction of the pylorus at a frequency of 3-4 cycles per minute (cpm) in human subjects. Alvarez [6] employed a galvanometer for his recordings; the use of electrodes for the procedure was pioneered by Bozler in 1945 [19]. In 1986, Hamilton *et al.* [67] were the first to use EGG with the purpose of investigating gastric motility disturbances from recordings of ECA potentials in humans. A recently developed theoretical model of the human stomach whose realism and usefulness in studying the GEA has been confirmed by computational and simulation studies [84, 85, 86] suggests that the GEA can be modeled by a ring of current dipoles of approximately equal magnitude and positioned homogeneously at equal distances from each other in the cylindrical body of the stomach. It has been shown both theoretically and experimentally that this dipole ring configuration can be well approximated by a single dipole located at the center of the circumferential ring and whose magnitude is equal to the sum of magnitudes of the smaller dipoles.

Modeling the GEA with accuracy and realism is an interesting theoretical and computational problem. Although a number of models have been proposed to simulate this phenomenon since the time when it was first detected by Alvarez [6], it can be difficult to ascertain which of them captures the characteristics of gastric activity most vividly. For example, coupled relaxation oscillator models are also suitable for studying the time evolution of smooth muscle propagation, while dipole models are more appropriate for the investigation of electrical source uncoupling. In the past, modeling the GEA using electric current dipoles led to two important predictions, namely that the natural GI slow wave frequency gradient may be detected noninvasively using magnetomers and also that slow wave propagation in gastric musculature results in propagating patterns of magnetic fields. In a previous study, GI models were also compared statistically to allow a direct assessment of how many GI electric sources are required to model the GEA realistically [89].

Throughout a typical propagation cycle, the amplitude of the electric potential recorded from a healthy human subject at the surface of the abdomen increases by more than one order of magnitude, while the propagation velocity is thought by some researchers [117] to reach around 6.8 mm/s in the pylorus from the approximate value of 0.3 cm/s at the beginning of the cycle. The slow wave frequency, on the other hand, varies from 3 cpm in the stomach [163] to approximately 12 cpm in the duodenum and 8 cpm in the terminal ileum [47, 127]. Lately, consistent efforts in the direction of modeling the complex phenomenon of gastric electrical activity have led to the development of various analytical and numerical electric wave propagation models that can reproduce EGG recordings [114, 116, 119, 115, 122]. It has thus been found that the frequency of slow wave cycles varies greatly not only depending upon the portion of the GI tract analyzed, but also upon the health state of the organ and other tissue characteristics.

There is significant clinical interest associated with the analysis of gastric and intestinal motility from bioelectric and biomagnetic recordings due to the relationship that has been shown to exist between gastrointestinal (GI) disorders and abnormalities in the characteristics of GEA. The presence of abnormal ECA propagation patterns has been found to be associated with many diseases, including gastroparesis [162], gastric myoelectrical dysrhythmia [140], atrophy and hypertrophy [17] and diabetic gastropathy [101]. Because abnormalities in the propagation of GI bioelectric currents are associated with disease states, a great deal of investigative effort has been invested in the direction of detecting them noninvasively. Experimentally, bioelectric currents have been detected and investigated using the EGG; in recent years, however, a number of inherent difficulties associated with this method−such as the dependence of electric recordings upon tissue conductivity, which attenuates the EGG signal−have suggested the use of the MGG instead, because the magnetic−and not electric−field of the stomach is measured with the latter procedure. This is advantageous because magnetic fields are dependent on tissue permeability, which is nearly equal to that of free space. Investigating the GEA from magnetic field recordings is also encouraging due to the finding that, although magnetic field strengths decrease rapidly with distance from their sources, they do reveal the characteristics of these sources in a more accurate manner.

In fact, the reliability of EGG has been questioned. Liang and Chen [103] showed that the detectability of gastric slow wave propagation from cutaneous EGG is dependent on the thickness of the abdominal wall and on the propagation velocity of the serosal slow wave. Bortolotti [18] pointed out that the practicality of using EGG to detect alterations in slow wave frequency due to tachy- and bradygastria remains problematic in spite of considerable recent progress to improve filtering and analysis methods. Reservations concering the significance of EGG as a diagnosis tool were also expressed by Camilleri *et al.* [32], who indicated that the precise meaning of dysrhythmias, signal amplitude changes and the duration of such abnormalities relative to gastric emptying as quantified by EGG remain to be clarified. In addition, the stability of EGG recordings is affected by a variety of artifacts, such as the overlap of the electrical activities of the colon and stomach in cutaneous EGG recordings [7]. This is why MGG and magnetoenterography (MENG) were developed as non-invasive alternatives to EGG [41, 167, 20]. In 1997, Bradshaw *et al.* showed that a high degree of correlation exists between the ECA frequency values determined using EGG and MGG [21]. EGG signals depend on the conductivities of the tissues where the quasistatic current sources producing them are located; moreover, they also depend on the permittivities of the insulating abdominal layers that are interposed between these current sources and the measurement sensors. Biomagnetic fields, on the other hand, are also dependent on the conductivities of the tissues where their sources are located because current sources are themselves dependent on conductivity. However, a key aspect to be noted here is that, in the case of the multilayered spheroidal model, magnetic fields depend to a far greater extent on the the permeability−rather than permittivity−of the tissues interposed between the sources of these fields and the locations where they are measured. This has been shown by Hämäläinen and Sarvas in [65], where these authors were able to demonstrate that secondary currents on outer interfaces between bioconductors only give negligible contributions to the magnetic field measured from outside the body.

Because the conductivity of the tissues where the sources are located affects only these secondary currents, it can be concluded that permittivity affects the measured magnetic fields less than permeability. It should also be mentioned here that the argument of Hämäläinen and Sarvas applies to our case because the multilayered spheroidal model has been found to be appropriate not only for the brain but also for the stomach [23, 24, 92, 93]. Thus, a distinction arises in this respect between bioelectric and biomagnetic fields in terms of how strongly they depend on the layers of abdominal tissues that are positioned between their sources and the measurement apparatus. Whereas the currents themselves depend on the permittivities of the emitting tissues in both cases, the strength of the magnetic field as measured from the sensor location is affected to a far greater extent by the permeability of the interposed layers than by their permittivity. Because the permeability of these interposed tissues that 'screen out' the field is nearly equal to that of free space (whereas their permittivity is not), it can be argued that there may be significant advantages to the use of MGG for clinical investigations as compared to EGG [24].

Due to the fact that gastric biomagnetic fields are very weak−having strengths of the order of 10^{-12} T−a highly sensitive measurement apparatus is required for experimental data collection. Such an instrument is the Superconducting QUantum Interference Device (SQUID) biomagnetometer, which remains to this date the most sensitive device for the detection and measurement of extremely low-magnitude magnetic fields. In particular, the Tristan 637i biomagnetometer, produced by Tristan Technologies (San Diego, CA), is a highly sensitive, multi-channel SQUID magnetometer system that can detect the bioelectromagnetic activity in the human stomach and intestine. Among others, the SQUID magnetometer has been shown to possess the ability of detecting intestinal ischemia, a disease that is difficult to diagnose and usually fatal. SQUID sensors are able to detect electrical signals resulting from the basic electrical rhythm (BER) of the intestine, whose frequency changes under ischemia. Thus, the potential for the use of SQUIDs in clinical diagnosis is significant.

Clinically, the ability to detect gastric activity noninvasively via a test that can be administered rapidly and efficiently would revolutionize functional gastroenterology. For the first time, reasons exist to hope that the MGG offers the possibility to fulfill this goal. In several important studies conducted in the Gastrointestinal SQUID Technology (GIST) Laboratory at Vanderbilt University, recordings from normal and divided pig stomachs were used to perform a comparative study of how propagation is affected in the latter case by deliberate damage of the smooth muscle tissue. It was then shown that SQUID magnetometers are capable of detecting abnormal characteristics of the GEA and of obtaining new and meaningful information that may help in the early diagnosis of gastroparesis. Because SQUID measurements are performed noninvasively, abnormal changes in the electrical signal of the GI tract can be detected without surgical intervention and the patient diagnosis process can be carried out rapidly, avoiding extensive patient preparation [174].

SQUID Magnetometry

SQUIDs have a long history of use for nondestructive evaluation (NDE) and testing (NDT), in which technical methods are used to examine materials or components in a manner that does not impair their future usefulness and serviceability [187]. In biomagnetism, these instruments were first used in 1970 by Edgar Edelsack, Jim Zimmerman and David Cohen, who recorded the magnetocardiogram (MCG) from the heart of a subject at the National Magnet Laboratory at the Massachusetts Institute of Technology (MIT). Later on, Cohen used SQUIDs to develop a novel technique called the magnetoencephalogram (MEG); his accomplishments prompted numerous other investigators to record signals due to a variety of other sources in the human

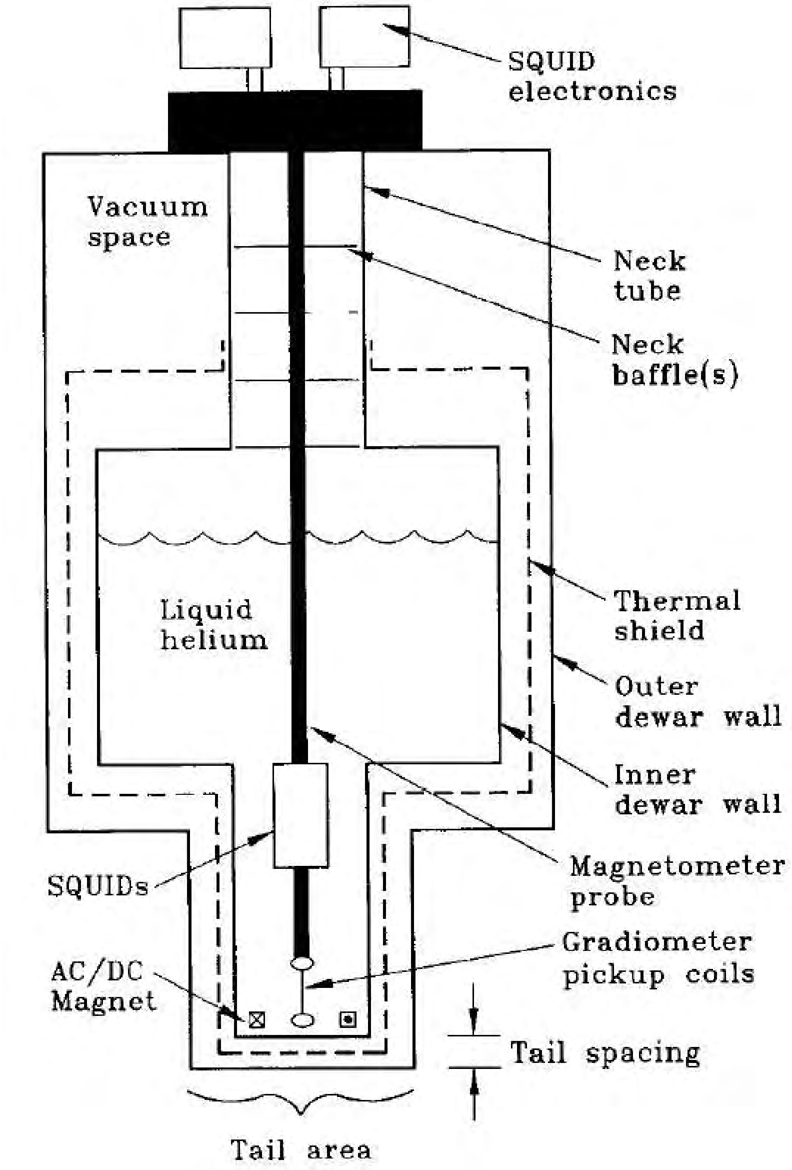

Figure I.1: Cross-sectional schematic of a simple T_c SQUID system. The SQUID and input coils are located within a superconducting niobium cylinder. A flux-locked loop is housed in a SQUID electronics box positioned above the dewar and linked to the SQUID via a magnetometer probe. When the dewar is filled with liquid helium, the SQUID, niobium canister and pickup coils are cooled to a temperature below the boiling point of He (4.2 K). From [96], reproduced with permission.

body [36, 37, 35]. The use of SQUIDs for the investigation of GI magnetic fields was pioneered in the Living State Physics Laboratories at Vanderbilt University in the 1990s. There, it was first shown that the biomagnetic fields of the stomach and intestine can be used to detect pathological conditions of these organs noninvasively. Since then, a great deal of research has been conducted in order to quantify and understand changes in the BER that are associated with abnormal conditions of the human GI tract.

A SQUID—or Superconducting QUantum Interference Device—is a magnetometer that contains one or more Josephson junctions. A Josephson junction is a weak insulative layer between two superconductors that is able to support a supercurrent below a critical temperature I_c [187]. In a direct current (DC) SQUID—which contains two Josephson junctions—a superconducting loop with a pair of Josephson junctions is applied in order to measure the loop impedance. Due to several special properties of the Josephson junction, the impedance is a periodic function of the magnetic flux threading the SQUID. Using this setup, a modulation signal applied to the bias current and a lock-in detector are employed to measure the impedance and to linearize the voltage-to-flux relationship. Thus the SQUID functions as a flux-to-voltage converter of extremely high sensitivity. In biomagnetism, where the strength of the measured field is very weak and a substantial amount of information is present at low frequencies, the SQUID magnetometer is excellently suited as a measurement tool.

A typical modern SQUID is located inside a small, cylindrical, superconducting magnetic shield within a liquid helium dewar. A number of superconducting pickup coils located at the bottom of the dewar are configured as gradiometers and are able to detect the difference in one component of the field between two points. When cooled below a critical temperature T_c, the superconductor exhibits zero resistence to DC currents up to a critical current value I_c. Due to a number of properties of

Figure I.2: The Tristan 637i SQUID magnetometer in the Biomagnetism Laboratory at Vanderbilt University. The magnetometer is located in a magnetically shielded room where measurements are taken noninvasively.

superconductors, the superconducting ring of a SQUID can only enclose an amount of magnetic flux Φ that is an integer multiple of the flux quantum $\Phi_0 = 2.07 \times 10^{-15}$ Wb [96]. The superconducting components of the SQUID are immersed in a helium reservoir which is thermally insulated by a vacuum jacket containing radiation shields.

Instead of exposing the actual SQUID to the external magnetic field to be measured, most modern instruments use a multi-turn pickup coil that is linked inductively to the SQUID. Thus, the pickup coils have the capability to sense the ambient field while the input coils of the SQUID are shielded from the external field within a superconducting niobium canister.

The Tristan 637i magnetometer has 5 pickup coils that record the magnetic field gradient in the $\hat{\mathbf{x}}$ direction and 5 coils for the $\hat{\mathbf{y}}$ direction. In addition, 19 axial coils are available for measuring gradients in the $\hat{\mathbf{z}}$ direction. The 29 superconducting pickup coils of the 637i SQUID magnetometer coils are distributed in the shape of two concentric, coplanar hexagons, as in Figure I.3, and can record the quantity $\Delta\mathbf{B}/\Delta z$. Ten other such input channels are also positioned in the same plane as the other channels, five of each being used to record $\Delta\mathbf{B}/\Delta x$ and $\Delta\mathbf{B}/\Delta y$, respectively.

The hardware associated with the Tristan magnetometer includes a cryogenic flux-to-voltage converter, superconducting pickup coils serving as a direct current flux transformer, connecting wires and a cryostat. Pickup coils are arranged in a gradiometer configuration with one pickup coil located a certain distance above a lower coil. These coils are wound in opposite directions so that the flux in the upper coil is subtracted from the flux in the lower coil, thus canceling steady ambient magnetic fields such as that of the Earth.

During a SQUID experiment, an analog-to-digital device is employed to convert the magnetic data recorded by these channels into binary file format. The data are stored as a matrix with 29 columns corresponding to each input channel of the SQUID

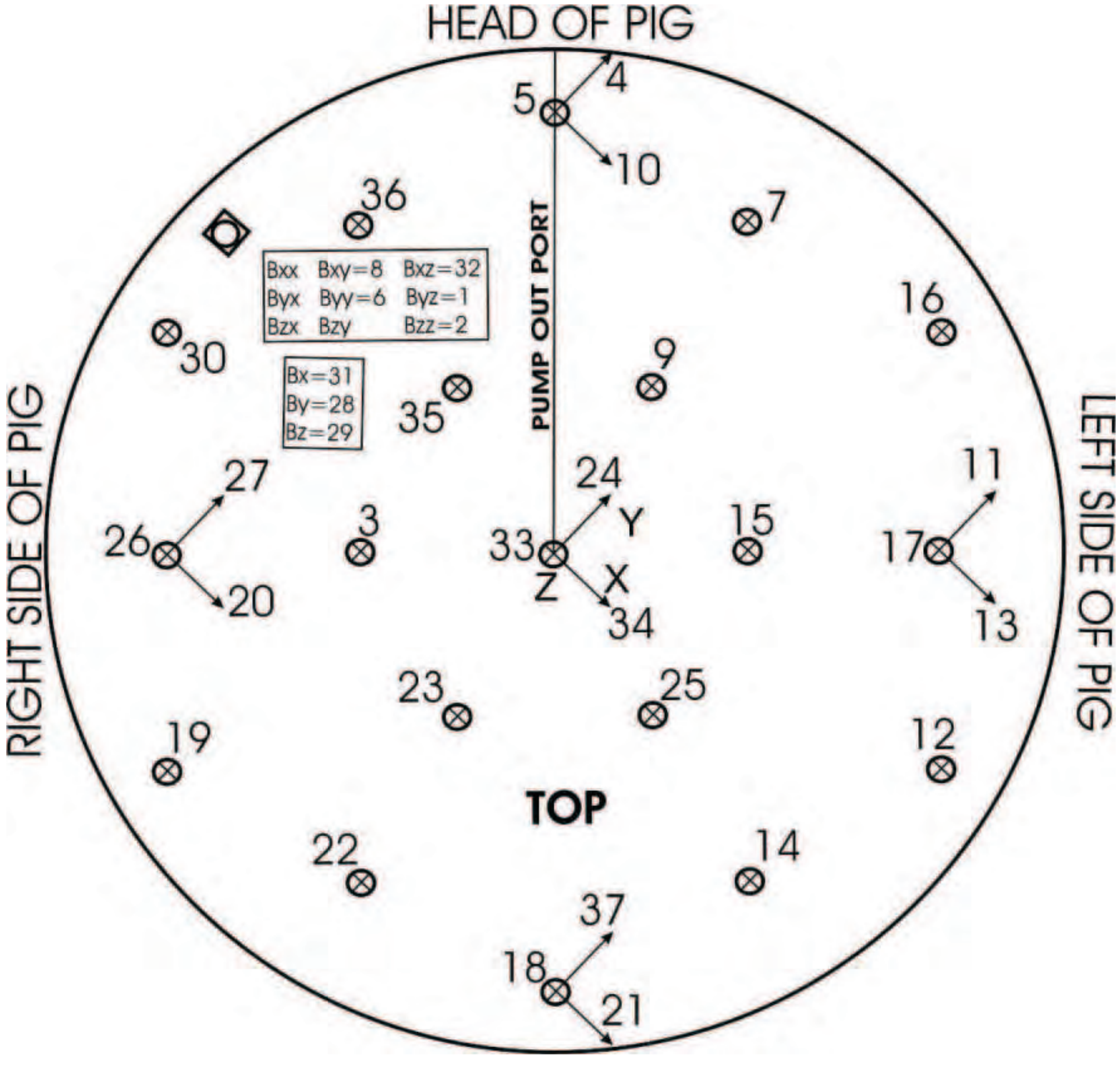

Figure I.3: Spatial distribution of the co-planar input coils for the 637i SQUID biomagnetometer produced by Tristan Technologies (San Diego, CA). The magnetometer possesses a total of 29 pickup coils that are distributed within two concentric hexagons around a 5-cm baseline. 19 of these coils record changes in the magnetic field in the $\hat{\mathbf{z}}$ direction (i.e. $\Delta\mathbf{B}_z/\Delta z$), while 5 coils record $\Delta\mathbf{B}_x/\Delta x$ and 5 record $\Delta\mathbf{B}_y/\Delta y$. The x and y channels are located at the center and extremities of the baseline and their positions are marked in the figure by short arrows inscriptioned with x or y, as appropriate. In addition to these 29 channels recording absolute changes in B_x, B_y and B_z, a number of noise channels and respiration channels for monitoring and recording breathholds are also provided.

magnetometerand and a number of rows equal to the number of discrete sampling times at which data values are recorded. Before the data are stored in digital format, a number of analog filters and downsampling operations are also carried out. In our case, the effective sampling frequency used for storing SQUID data is user selectable and with a commonly used value of 300 Hz, although the actual sampling frequency of the SQUID magnetometer is higher.

Two types of coil assemblies are present among the 29 signal channels: an axial assembly and a three-channel vector assembly. A number of 14 axial assemblies and 5 vector assemblies are present in the sensor; signal channels are first-order gradiometers with a baseline of 5 cm while the normal channel is an axial gradiometer. In the vector assemblies, two transverse channels are planar gradiometers. The gradiometers of the SQUID are designed in such fashion as to reduce environmental magnetic noise, which is due to distant sources and couples equal but opposite signals into the two gradiometer coils. Because biological signals are located close to the input array, their sources will couple strongly into the closest gradiometer coil, while the distant coil causes little signal loss. For this reason, the gradiometer design of the SQUID impacts only signals when dealing with distant environmental sources of noise. For sources in the stomach and intestine, the signal coils are therefore essentially magnetometers.

The 29 z channels of the SQUID measure only the $\mathbf{B}$ field component that is normal to the outer surface of the sensor and, because of the experimental setup for GI recordings, normal to the body of the subject. All three components of the field are measured at only five locations, thus allowing one to determine the direction of the field and its magnitude at those particular positions.

In addition to the 29 channels that record magnetic field data, a number of 8 magnetic sensing channels are provided in a tensor array to monitor environmental magnetic noise. This array is located high enough above the input coils to avoid

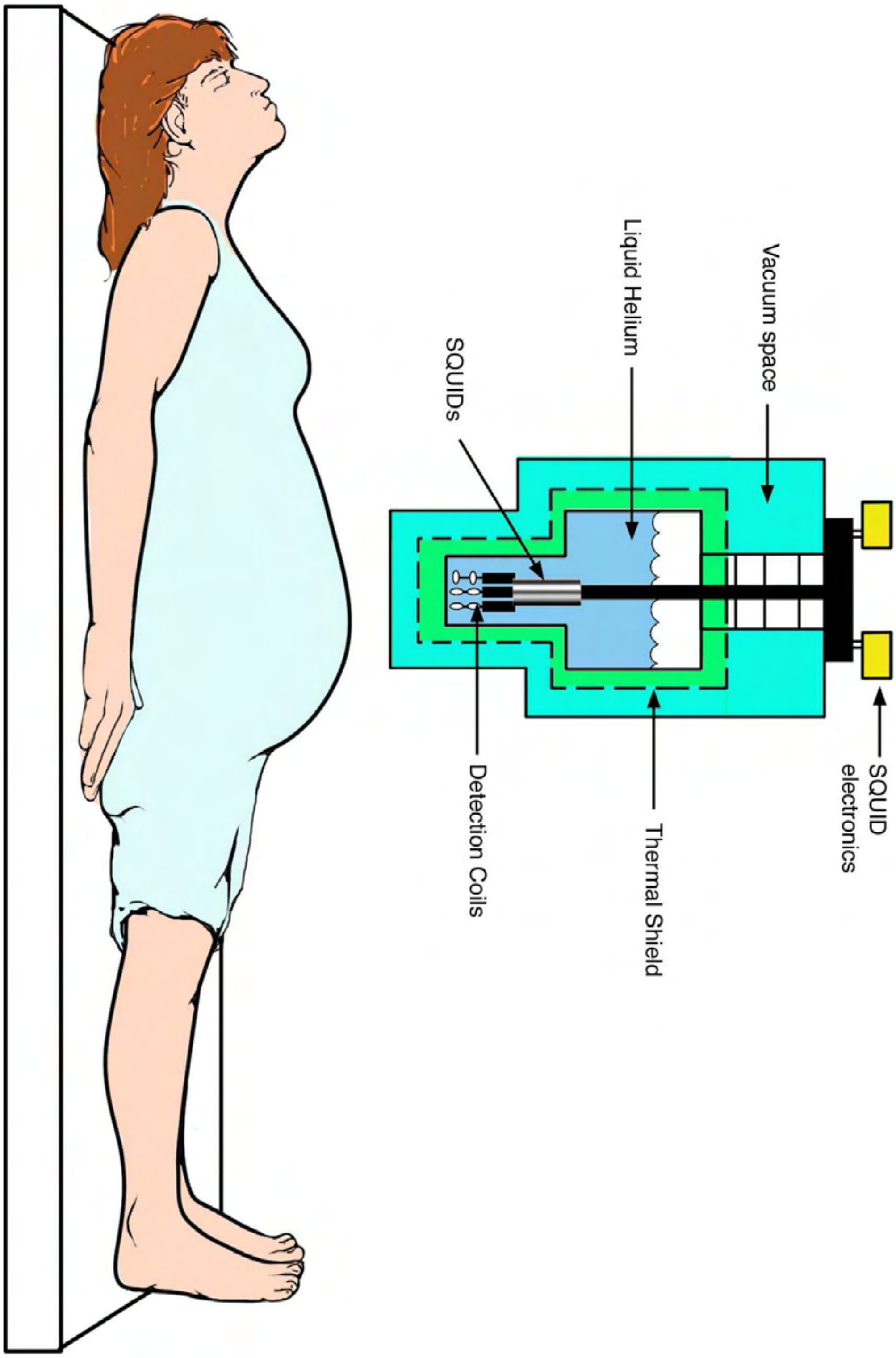

Figure I.4: Experimental setup for data acquisition in MGG. The subject is positioned horizontally directly below the pickup coils of the SQUID gradiometer.

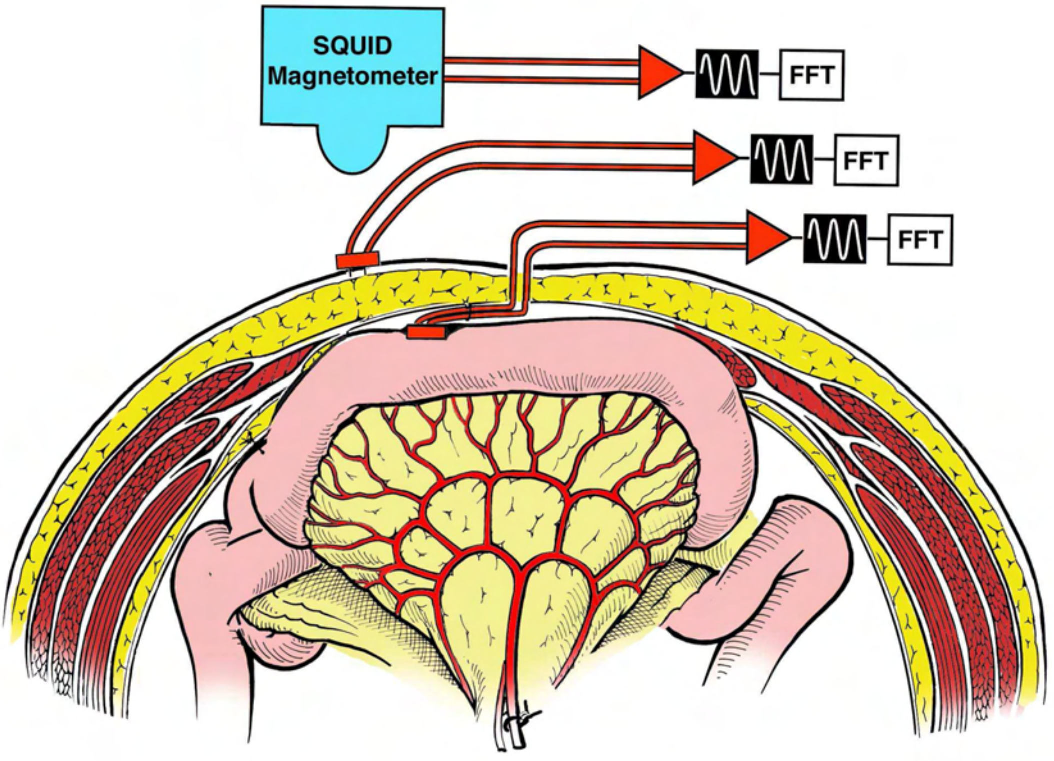

Figure I.5: Experimental setup of simultaneous MENG/EENG data acquisition. The intestine of most common mammals is located under several layers of skin, fat and other tissues, which all attenuate the EENG signal. For this reason, the EENG is invasive because it requires the placement of electrodes directly on the external gastric wall surface, while the MGG is non-invasive because magnetic fields are recorded in the latter procedure. Because the permittivity of biological tissues is nearly equal to that of free space, the MGG signal is attenuated far less than the EGG signal.

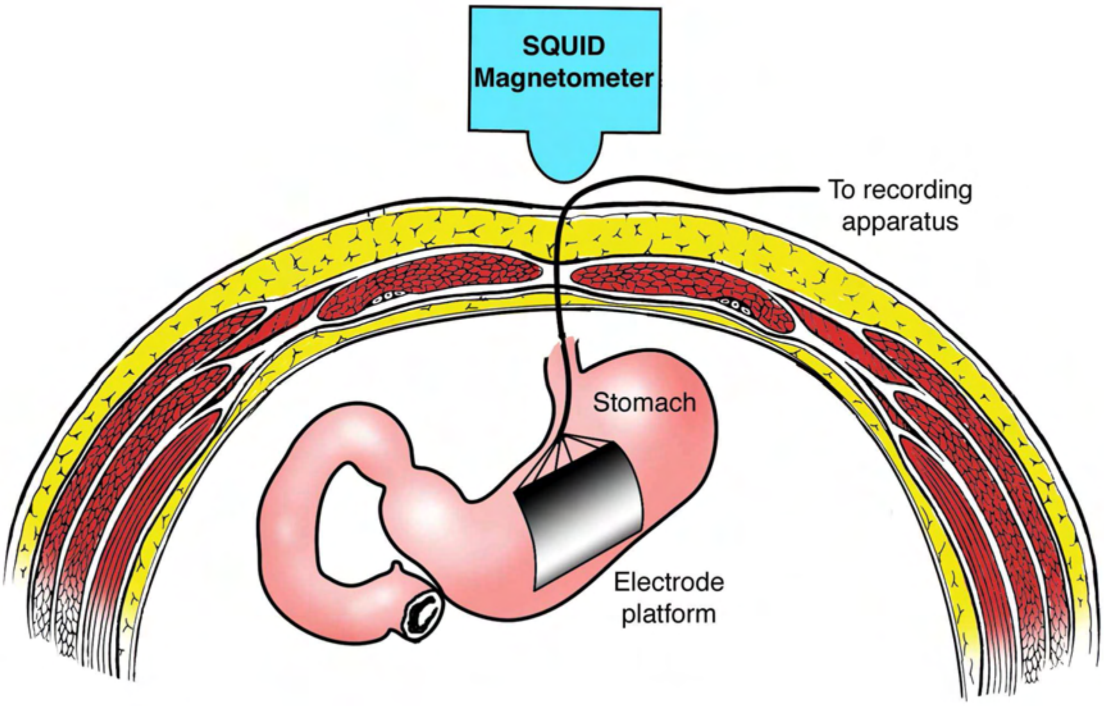

Figure I.6: Experimental setup of simultaneous MGG/EGG data acquisition. The EGG electrode platform is placed invasively at the external surface of the stomach while the SQUID magnetometer is positioned above the body.

detection of the signal of interest but close enough to the subject to record environmental noise that is representative of the noise in the signal coils. The total of 37 SQUID channels are mounted in a 27 liter liquid helium dewar, although the average helium consumption is less than 6 liters per day, allowing the system to remain usable for several days in a row after the cooling of the SQUID.

MGG and MENG experiments are conducted at Vanderbilt University in the magnetically shielded room of the Biomagnetism Laboratory. Informed consent is obtained from every volunteer and each study must be approved by the Vanderbilt University Institutional Review Board (VUIRB). In a typical experiment of this type, the subject is positioned horizontally below the magnetometer coils and is then asked to suspend respiration and lie quietly for a period of at least one minute during each recording. A drawing of the experimental setup in such cases is provided in Figure I.4. In some cases, fasting is required of the subject prior to the experiment. Very often, biomagnetic data are acquired both before and after the consumption of a meal to study the electrical activity of the stomach in both of these two conditions. For each recording, the magnetometer is oriented such that the coils measuring the x and y components of the signal tangential to the body surface are oriented in the saggital and horizontal planes. On the other hand, the coil measuring the z component normal to the body surface is oriented in the frontal plane. [22].

A variety of clinical investigations and data measurements can be done with the Tristan SQUID magnetometer, as shown in Figure I.5 and Figure I.6. Very often, measurements for both the MGG/MENG and the EGG/EENG are taken at the same time not only for practical reasons but also to have both signals available for investigation, e.g. in a correlation study of the MGG and EGG signals. Because the EGG/EENG signal is attenuated dramatically from the internal source to the external environment due to the presence of skin and fat, EGG electrodes are often placed invasively directly on the outer surface of the stomach. The MGG signal, however, depends on the permittivity of tissues, which is nearly equal to μ_0. Thus MGG signals can be acquired noninvasively.

CHAPTER II

POTENTIALS AND FIELDS FOR A CURRENT DIPOLE IN AN ELLIPSOID

Introduction

The forward problem of bioelectromagnetism plays an important role in the scientific area of biophysical electrodynamics. In human brain studies [66], for example, where the forward problem has been in the focus of attention for a considerable period of time, noninvasive recordings of magnetic fields generated in the head have allowed researchers to detect and measure brain electrical activity directly via electroencephalography (EEG) and magnetoencephalography (MEG) [12, 136]. In magnetogastrography (MGG), on the other hand, the phenomenon under study is the gastric electrical activity (GEA), generated by the periodic depolarization and repolarization of cells in the stomach [22, 32]. The GEA originates in the corpus of this organ as a wave propagating aborally towards the pylorus through the electric syncytium of the stomach [144]. In the quasistatic approximation, the phenomenon can be modeled as one or several current dipoles. A current dipole $\mathbf{Q}$ is a good approximation for a small source viewed from a distant field point; it is a concentration of some impressed current density $\mathbf{J}_i$ to a single point $\mathbf{r}_0$. Anomalies in the characteristics of dipole propagation have been studied [112] and their relevance to the field of medical diagnosis has been the focus of active research [21, 53]. In particular, the use of superconducting quantum interference device (SQUID) magnetometers, pioneered by Cohen *et al.* in the 1970s [35, 36, 37], has proven to be very suitable for detecting and studying the GEA both in healthy and diseased subjects [21]. An important practical aspect in favor of using SQUIDs for experimental biological data acquisition is the ability to study gastrointestinal electromagnetic phenomena noninvasively, which greatly eases the task of conducting clinical studies. Moreover, non-invasive GEA studies are encouraging in light of current efforts to identify effective ways of analyzing the phenomenon of abnormal current propagation, which is associated with pathological conditions such as gastroparesis and ischemia [23].

The current dipole approximation has been widely used in the literature to model the biological electrical activity [131]. To study this phenomenon, the body of the stomach has been simulated using cylinders, cones, conoids, ellipsoids and, very recently, using a realistic model of the human body via the finite element and boundary element methods [30]. In 1985 [121, 122], Mirizzi *et al.* proposed a mathematical model to simulate the extracellular electrical control activity where an annular band polarized by electric current dipoles moves distally from the mid-corpus to the terminal antrum. In 1995, Mintchev & Bowes constructed a conoidal dipole model of the electrical field produced by the human stomach, where spontaneous depolarization and repolarization due to ionic exchange were simulated [114]. Later, Irimia & Bradshaw constructed a model of the stomach in which an annular band of dipoles advances along a truncated ellipsoid [87], thus simulating the electric potential and electric field recorded by a nasogastric probe.

An important advantage of using the ellipsoidal model in both MGG and EGG is the fact that the problem is approached more realistically than in the case of spherical and conoidal models. Moreover, ellipsoidal geometry offers a suitable ground for the evaluation of inverse problem algorithms in both MEG and MGG. Computing the electric potential ϕ and electric field $\mathbf{E}$ due to an electric current dipole in an ellipsoid requires a truncated expansion of normal ellipsoidal harmonic terms $\mathbb{E}_n^m$. The general approach to this was first proposed by Kariotou [99] and Dassios [44], who outlined the formalism for this problem but who derived formulas for ϕ only up to order 2 in $\mathbb{E}_n^m$. Analogous formulas for the electric field $\mathbf{E}$ have not yet been derived. In our most recent study [92], the electric potential of the stomach was successfully simulated using the low-order ellipsoidal harmonic expansion of Dassios & Kariotou. However, it was found that all ellipsoidal terms included in this expansion (order 1 and 2) contributed substantially to the computed electric potential. This raises the important question as to whether the contributions of higher-order terms may also be significant in electro- and magneto- gastrographic modelling. This issue is significant because the accuracy of the calculation may be seriously affected if an insufficient number of ellipsoidal terms are included in the expansion. The purpose of the present article is to address this problem by providing a generalized theoretical and computational approach to the calculation of ϕ and $\mathbf{E}$ using an arbitrarily large expansion of ellipsoidal terms. The computer implementation of our proposed formalism would then allow one to investigate the contributions of these terms and to identify suitable cutoffs to the associated harmonic expansions so that an accurate calculation of the two physical quantities under consideration (ϕ and $\mathbf{E}$) is made possible.

In the following section, we present the mathematical formalism behind our model. We then continue by deriving formulas for two important quantities in our calculation, namely the gradient $\boldsymbol{\nabla}$ of the normal harmonic functions $\mathbb{E}_n^m$ and the first derivative of the associated Lamé functions E_n^m. Thereafter, generalized expressions for ϕ and $\mathbf{E}$ are found using the mathematical tools developed and computational considerations regarding the overall problem are addressed in the following section. Thus, the material in section 2 is a review of previous work while the remainder of the paper contains novel results. We conclude with a discussion and summary of our model, which we intend to implement numerically with the purpose of answering the important modelling issues raised above.

Mathematical formalism

Throughout our derivations, we make use of the standard equation of the ellipsoid

$$\frac{x_1^2}{\alpha_1^2} + \frac{x_2^2}{\alpha_2^2} + \frac{x_3^2}{\alpha_3^2} = 1 \tag{II.1}$$

where $(x_1,\, x_2,\, x_3)$ are the usual Cartesian coordinates $(x,\, y,\, z)$ and $0 < \alpha_3 < \alpha_2 < \alpha_1 < +\infty$ are the ellipsoidal semiaxes. As in [99, 72], we also employ the ellipsoidal system, with coordinates ρ, μ and ν and semifocal distances h_1, h_2 and h_3, defined by

$$\begin{aligned} h_1^2 &= \alpha_2^2 - \alpha_3^2 && \text{(II.2)} \\ h_2^2 &= \alpha_1^2 - \alpha_3^2 && \text{(II.3)} \\ h_3^2 &= \alpha_1^2 - \alpha_2^2. && \text{(II.4)} \end{aligned}$$

Conversion from ellipsoidal to Cartesian coordinates can be made via the relationships

$$\begin{aligned} x_1 &= \frac{\rho\mu\nu}{h_2 h_3} && \text{(II.5)} \\ x_2 &= \frac{\sqrt{\rho^2 - h_3^2}\sqrt{\mu^2 - h_3^2}\sqrt{h_3^2 - \nu^2}}{h_1 h_3} && \text{(II.6)} \\ x_3 &= \frac{\sqrt{\rho^2 - h_2^2}\sqrt{h_2^2 - \mu^2}\sqrt{h_2^2 - \nu^2}}{h_1 h_2}, && \text{(II.7)} \end{aligned}$$

where $\rho \in [h_2, +\infty)$, $\mu \in [h_3, h_2]$ and $\nu \in [-h_3, h_3]$. In ellipsoidal coordinates, the Laplace equation has the form

$$\left(\mu^2 - \nu^2\right) \frac{\partial^2 \phi}{\partial \beta^2} + \left(\rho^2 - \nu^2\right) \frac{\partial^2 \phi}{\partial \varphi^2} + \left(\rho^2 - \mu^2\right) \frac{\partial^2 \phi}{\partial \chi^2} = 0, \tag{II.8}$$

where

$$\beta = \int_{h_2}^{\chi} \frac{d\rho}{\sqrt{\rho^2 - h_3^2}\sqrt{\rho^2 - h_2^2}} \tag{II.9}$$

$$\varphi = \int_{h_3}^{\mu} \frac{d\mu}{\sqrt{\mu^2 - h_3^2}\sqrt{h_2^2 - \mu^2}} \tag{II.10}$$

$$\chi = \int_{0}^{\nu} \frac{d\nu}{\sqrt{h_3^2 - \nu^2}\sqrt{h_2^2 - \nu^2}} \tag{II.11}$$

and ϕ is the electric potential.

To calculate the electric potential ϕ for an ellipsoid, separation of variables for the Laplace equation in ellipsoidal coordinates leads to the Lamé equation, which assumes the following form for each of the three spatial coordinates $\eta_i = \rho, \mu, \nu$:

$$\begin{aligned} &\left(\eta_i^2 - h_3^2\right)\left(\eta_i^2 - h_2^2\right) E''(\eta_i) + \eta_i \left(2\eta_i^2 - h_3^2 - h_2^2\right) E'(\eta_i) + \\ &\qquad \left[\left(h_2^2 + h_3^2\right) P - n(n+1)\eta_i^2\right] E(\eta_i) = 0. \end{aligned} \tag{II.12}$$

Above, P, n are constants, the prime in E', etc. indicates differentiation with respect to the independent variable $\eta_i = \rho, \mu, \nu$, and the quantities E are the so-called Lamé functions that form the normal interior harmonic function

$$\mathbb{E}_n^m(\rho, \mu, \nu) = E_n^m(\rho) E_n^m(\mu) E_n^m(\nu). \tag{II.13}$$

The corresponding exterior harmonic functions $\mathbb{F}_n^m$ are given by

$$\begin{aligned} \mathbb{F}_n^m(\rho, \mu, \nu) &= (2n+1)\mathbb{E}_n^m(\rho, \mu, \nu) I_n^m(\rho) \\ &= (2n+1) I_n^m(\rho) E_n^m(\rho) E_n^m(\mu) E_n^m(\nu), \end{aligned} \tag{II.14}$$

where I_n^m are elliptic integrals of the form

$$I_n^m(\rho) = \int_\rho^\infty \frac{dt}{\left[E_n^m(t)\right]^2 \sqrt{t^2 - h_2^2}\sqrt{t^2 - h_3^2}} \tag{II.15}$$

with $n = 0, 1, 2, ...,$ and $m = 1, 2, ... , 2n + 1$. Interior harmonic functions enter the expression for the electric potential only for the space enclosed by the ellipsoid, while exterior harmonic functions are used to define the potential outside this body. In fact, internal harmonic terms diverge as $r \to \infty$, while external terms tend to 0 in the same limit, as expected. Naturally, the surface potential can be computed using either internal or external harmonics since the boundary conditions imposed upon solving the Laplace equation guarantee the absence of any anomalous discontinuities in the potential across the two media.

It was first shown by Lamé that four classes (also called species) of Lamé functions exist, typically denoted by $K(\eta_i)$, $L(\eta_i)$, $M(\eta_i)$, and $N(\eta_i)$, respectively, where η_i is any of the coordinates ρ, μ, or ν. These are referred to as Lamé functions of the first (as opposed to second) kind, a label that we omit from this point forward because our theory does not involve Lamé functions of the second kind.

The Lamé functions of the first kind involve polynomials and can be written as

$$\begin{aligned}
K(\eta_i) &= \sum_{k=0}^{r+1} a_k \eta_i^{n-2k} && \text{(II.16)}\\
L(\eta_i) &= \sqrt{\eta_i^2 - h_3^2}\sum_{k=0}^{n-r} a_k \eta_i^{n-(k+1)} && \text{(II.17)}\\
M(\eta_i) &= \sqrt{h_2^2 - \eta_i^2}\sum_{k=0}^{n-r} a_k \eta_i^{n-(k+1)} && \text{(II.18)}\\
N(\eta_i) &= \sqrt{\left(\eta_i^2 - h_3^2\right)\left(\eta_i^2 - h_2^2\right)}\sum_{k=0}^{r} a_k \eta_i^{n-2(k+1)}, && \text{(II.19)}
\end{aligned}$$

where the coefficients a_k can be obtained by inserting the appropriate Lamé functions into the Laplace equation, acoording to the approach described by Hobson [72]. The additional restriction must be placed that the power of each η_i in the expressions for K, L, M and N above must be greater than or equal to zero. The index r in the summations above is given by

$$r = \begin{cases} \frac{n}{2} & \text{for} \quad n \quad \text{even} \\ \frac{n-1}{2} & \text{for} \quad n \quad \text{odd} \end{cases}, \tag{II.20}$$

where n is the degree of the ellipsoidal harmonic $\mathbb{E}_n^m$. For a harmonic of degree n, there are $2n+1$ associated Lamé functions; it can be inferred from Eq. II.19 that there are $r+1$ functions of type K, $n-r$ functions of type L, $n-r$ functions of type M and r functions of type N, for a total of $2n+1$ Lamé functions. Although not required for our derivations, we give the definition of the Lamé functions of the second kind F_n for completeness. These functions were introduced independently by Liouville and Heine; they involve the Lamé functions of the first kind as well as elliptic integrals. Their general definition is given by

$$F_n(\eta) = (2n+1)E_n(\eta) \int_\eta^\infty \frac{d\eta}{\sqrt{\eta^2 - h^2}\sqrt{\eta^2 - k^2}}, \tag{II.21}$$

where h and k are constants determined by the geometry ([72] discusses this type of functions in more detail).

In the ellipsoidal formalism, Lamé functions are used to construct ellipsoidal harmonic functions, which are eigenfunctions of the Laplacian operator in ellipsoidal coordinates. Thus, Lamé functions and the triplet $(E_n^m(\rho),\, E_n^m(\mu),\, E_n^m(\nu))$ are analogous to the radial function $R_l^m(r)$ and spherical harmonics $Y_l^m(\theta,\phi)$−i.e. to the doublet $(R_l^m(r),\, Y_l^m(\theta,\phi))$−in spherical harmonic theory.

Products of the form $E_n^m(\mu)E_n^m(\nu)$ are called surface ellipsoidal harmonics because they refer to the ellipsoidal surface $\rho = \rho_0$. We adopt the convention used by Kariotou [99] and label the normalization functions associated with ellipsoidal harmonics as γ_n^m. These quantities assume the form

$$\gamma_n^m = \oint_{\rho=\rho_0} \frac{\left[E_n^m(\mu) E_n^m(\nu)\right]^2}{\sqrt{\left(\rho_0^2 - \mu^2\right)\left(\rho_0^2 - \nu^2\right)}} dS, \tag{II.22}$$

where

$$dS = d\mu d\nu \left(\mu^2 - \nu^2\right) \sqrt{\frac{\left(\rho^2 - \mu^2\right)\left(\rho^2 - \nu^2\right)}{\left(\mu^2 - h_3^2\right)\left(h_2^2 - \mu^2\right)\left(h_3^2 - \nu^2\right)\left(h_2^2 - \nu^2\right)}} \tag{II.23}$$

is the ellipsoidal surface element in the same coordinate system [31]. The formulation of ellipsoidal harmonics in Cartesian coordinates is given by

$$\mathbb{E}_n^m(\mathbf{r}) = C_{ij} \prod_{k=1}^{m} \Theta_k, \tag{II.24}$$

where $\Theta_k(x, y, z)$ is known as the Niven function [128, 72],

$$\Theta_k = \frac{x^2}{\alpha_1^2 + \theta_k} + \frac{y^2}{\alpha_2^2 + \theta_k} + \frac{z^2}{\alpha_3^2 + \theta_k} - 1, \tag{II.25}$$

while θ_k is the k-th root of the Lamé function E_n^m. C denotes a matrix whose elements are given in Cartesian coordinates and are labeled by subscripts i and j, indicating the corresponding row and column, respectively, of the appropriate entry. C has the form

$$C = \left\{ \begin{array}{cccc} & x & yz & \\ 1 & y & zx & xyz \\ & z & xy & \end{array} \right\}. \tag{II.26}$$

Columns in C correspond to each of the function types K, L, M and N, while rows refer to the coordinates in the chosen system, i.e. x, y or z in the Cartesian system. To evaluate $\mathbb{E}_n^m$ using Eq. II.24, one must select appropriate entries in C for each coordinate and multiply the resulting quantity by the product $\prod_k^m \Theta_k$. Lamé showed that the roots of the functions bearing his name must all be real, distinct and located in the interval $(-\alpha_1^2, \alpha_3^2)$. In ellipsoidal coordinates, the harmonics can be written as

$$\mathbb{E}_n^m(\mathbf{r}) \quad = \quad L_{ij} \prod_{k=1}^{m} \Psi_k, \tag{II.27}$$

where L_{ij} denotes the appropriate entry in the table L given in ellipsoidal coordinates, where

$$L = \left\{ \begin{array}{ccccc} & \rho & \sqrt{\rho^2 - h_3^2} & \sqrt{\rho^2 - h_2^2} & \sqrt{\left(\rho^2 - h_3^2\right)\left(\rho^2 - h_2^2\right)} \\ 1 & \mu & \sqrt{\mu^2 - h_3^2} & \sqrt{h_2^2 - \mu^2} & \sqrt{\left(\mu^2 - h_3^2\right)\left(h_2^2 - \mu^2\right)} \\ & \nu & \sqrt{h_3^2 - \nu^2} & \sqrt{h_2^2 - \nu^2} & \sqrt{\left(h_3^2 - \nu^2\right)\left(h_2^2 - \nu^2\right)} \end{array} \right\} \tag{II.28}$$

and

$$\Psi_k = \left(\rho^2 - \psi_k^2\right)\left(\mu^2 - \psi_k^2\right)\left(\nu^2 - \psi_k^2\right). \tag{II.29}$$

In this case, ψ_k are the roots of the corresponding function $\Psi_k(\rho, \mu, \nu)$ expressed in ellipsoidal coordinates.

The two coordinate systems used above (Cartesian and ellipsoidal) are both important throughout our derivations; for this reason, formulas of interest will be given in a form that is independent of the coordinate system chosen. In this section, we derive two particular quantities that are of interest in each of them, namely the gradient of the normal ellipsoidal harmonic function $\mathbb{E}_n^m$ and the derivative of the Lamé polynomial E_n^m.

For any diagonal metric tensor $g_{ij} = g_{ii}\delta_{ij}$ (where δ_{ij} is the usual Kronecker delta function), the scale factors s_i are defined in terms of the parametrizations $x_i = f_i$, where x_i are the Cartesian coordinates and f_i are the functions x_i in terms of some other coordinates η_i. In our case, η_i are the ellipsoidal coordinates ρ, μ and ν and the parametrizations f_i are given in Eqs. II.5-II.7. For three-dimensional space, the scale factors s_i are defined as

$$\begin{aligned} s_i &= (g_{ii})^{1/2} && \text{(II.30)} \\ &= \left[\sum_{k=1}^{3}\left(\frac{\partial f_k}{\partial \eta_i}\right)^2\right]^{1/2}. && \text{(II.31)} \end{aligned}$$

In this generalized formalism, the gradient $\boldsymbol{\nabla} w(\eta_i)$ of any function w of three independent variables η_i assumes the form

$$\boldsymbol{\nabla} w = \sum_{i=1}^{3} \frac{1}{s_i}\frac{\partial w}{\partial \eta_i}\widehat{\mathbf{a}}_i, \tag{II.32}$$

where $\widehat{\mathbf{a}}_i$ are the three unit vectors in the coordinate system η_i. For the Cartesian case, we obtain the familiar expression

$$\boldsymbol{\nabla} = \widehat{\mathbf{x}}\frac{\partial}{\partial x} + \widehat{\mathbf{y}}\frac{\partial}{\partial y} + \widehat{\mathbf{z}}\frac{\partial}{\partial z}. \tag{II.33}$$

Applying this formalism to the ellipsoidal coordinate case, we obtain

$$\boldsymbol{\nabla} = \frac{1}{s_\rho}\widehat{\boldsymbol{\rho}}\frac{\partial}{\partial \rho} + \frac{1}{s_\mu}\widehat{\boldsymbol{\mu}}\frac{\partial}{\partial \mu} + \frac{1}{s_\nu}\widehat{\boldsymbol{\nu}}\frac{\partial}{\partial \nu}, \tag{II.34}$$

where inverses of the scale factors [124] are given by

$$\frac{1}{s_\rho} = \sqrt{\frac{(\rho^2 - h_2^2)(\rho^2 - h_3^2)}{(\rho^2 - \mu^2)(\rho^2 - \nu^2)}} \tag{II.35}$$

$$
\begin{aligned}
\frac{1}{s_\mu} &= \sqrt{\frac{(\mu^2 - h_2^2)(\mu^2 - h_3^2)}{(\mu^2 - \rho^2)(\mu^2 - \nu^2)}} && \text{(II.36)} \\
\frac{1}{s_\nu} &= \sqrt{\frac{(\nu^2 - h_2^2)(\nu^2 - h_3^2)}{(\nu^2 - \rho^2)(\nu^2 - \mu^2)}}. && \text{(II.37)}
\end{aligned}
$$

Another quantity that will be useful later is the outward unit vector $\widehat{\mathbf{n}}$ with respect to the surface of the ellipsoid. In Cartesian coordinates, the ellipsoid can be defined [87] by the implicit equation $F(x, y, z) = 0$, where

$$
F(x, y, z) = \frac{x^2}{\alpha_1^2} + \frac{y^2}{\alpha_2^2} + \frac{z^2}{\alpha_3^2} - 1. \tag{II.38}
$$

It follows by a theorem of vector calculus [61] that, in the Cartesian coordinate system, the normal unit vector can be defined as

$$
\begin{aligned}
\widehat{\mathbf{n}} &= \left[\left(\frac{\partial F}{\partial x}\right)^2 + \left(\frac{\partial F}{\partial y}\right)^2 + \left(\frac{\partial F}{\partial z}\right)^2\right]^{-1/2} \boldsymbol{\nabla} F && \text{(II.39)} \\
&= \left(\frac{x}{\alpha_1^2}\widehat{\mathbf{x}} + \frac{y}{\alpha_2^2}\widehat{\mathbf{y}} + \frac{z}{\alpha_3^2}\widehat{\mathbf{z}}\right)\left(\frac{x^2}{\alpha_1^4} + \frac{y^2}{\alpha_2^4} + \frac{z^2}{\alpha_3^4}\right)^{-1/2}. && \text{(II.40)}
\end{aligned}
$$

For ellipsoidal coordinates, the expression for this function is quoted in [43] as being given by

$$
\widehat{\mathbf{n}} = D_n \widehat{\boldsymbol{\rho}}, \tag{II.41}
$$

with

$$
D_n = \frac{\alpha_2 \alpha_3}{\sqrt{(\alpha_1^2 - \mu^2)(\alpha_1^2 - \nu^2)}}. \tag{II.42}
$$

To compute the gradient of the Lamé function, the Cartesian coordinate system is preferable because of the simple form assumed by this operator in terms of x, y and

z. Applying the gradient operator to the Cartesian coordinate expression in Eq. II.24 and keeping in mind the product rule of differentiation yields the result

$$\nabla \mathbb{E}_n^m(\mathbf{r}) \;=\; \left[\mathbf{G}_{ij} + \left(C_{ij}\sum_{k=1}^{m}\xi_k\right)\widehat{\mathbf{u}}\right]\prod_{l=1}^{m}\Theta_l, \tag{II.43}$$

where $\mathbf{G}$ is a vector matrix with entries

$$\mathbf{G} \;=\; \left\{\begin{array}{cccc} & \widehat{\mathbf{x}} & y\widehat{\mathbf{z}} + z\widehat{\mathbf{y}} & \\ \mathbf{0} & \widehat{\mathbf{y}} & x\widehat{\mathbf{z}} + z\widehat{\mathbf{x}} & xy\widehat{\mathbf{z}} + yz\widehat{\mathbf{x}} + xz\widehat{\mathbf{y}} \\ & \widehat{\mathbf{z}} & x\widehat{\mathbf{y}} + y\widehat{\mathbf{x}} & \end{array}\right\}. \tag{II.44}$$

The function ξ_k is defined as

$$\begin{aligned} \xi_k(\mathbf{r}) &= \frac{1}{\Theta_k}\nabla\Theta_k \\ &= \frac{2}{\Theta_k}\left(\frac{x}{\alpha_1^2+\theta_k} + \frac{y}{\alpha_2^2+\theta_k} + \frac{z}{\alpha_3^2+\theta_k}\right) \end{aligned} \tag{II.45}$$

and $\widehat{\mathbf{u}} = \widehat{\mathbf{x}} + \widehat{\mathbf{y}} + \widehat{\mathbf{z}}$ is composed of the three orthonormal vectors in each of the coordinate directions.

Before we address the problem of computing $\nabla\mathbb{E}_n^m$ in ellipsoidal coordinates, let us compute the first derivative of the Lamé polynomial E_n^m, which has the general form

$$\frac{d}{d\eta_i}E_n^m(\eta_i) = L_{ij}\frac{d}{d\eta_i}B^m + L'_{ij}B^m, \tag{II.46}$$

the prime in L'_{ij} denoting differentiation of the appropriate entry in table L with respect to η_i. The function B^m is defined as

$$B^m = \prod_{k=1}^{m} (\eta_i^2 - \psi_k^2) \tag{II.47}$$

$$= \prod_{k=1}^{m} (\eta_i - \psi_k)(\eta_i + \psi_k). \tag{II.48}$$

We made use, on the last line above, of the property $\psi_k \in \mathbb{R}$ characteristic of Lamé function roots to factor out the quantity $\eta_i^2 - \psi_k^2$. In other words, since the roots of a Lamé function are always real by definition (see [72]), the quantity $\eta_i^2 - \psi_k^2$ can be written as $(\eta_i - \psi_k)(\eta_i + \psi_k)$. It is also important to note that the symbol η_i is employed to denote the independent variable for E_n^m, where $\eta_i = \rho$, μ or ν. This is to emphasize that the B^m function has the same general form for each of all three spatial ellipsoidal coordinates. As expected, the definition of the Lamé polynomials given above is consistent with the separability of the normal ellipsoidal harmonics into functions depending only on one of ρ, μ or ν (see Eq. II.13); this can be made obvious by noting that the entries in each row of L are functions of only one variable, whereas only the normal ellipsoidal harmonic function $\mathbb{E}_n^m$ depends on all three spatial coordinates. The entries in the matrix L' can be computed straightforwardly by differentiation. They are

$$L'_{i1} = 0 \tag{II.49}$$

$$L'_{i2} = 1 \tag{II.50}$$

$$L'_{13} = \frac{\rho}{\sqrt{\rho^2 - h_3^2}} \tag{II.51}$$

$$L'_{14} = \frac{\rho}{\sqrt{\rho^2 - h_2^2}} \tag{II.52}$$

$$
\begin{aligned}
L'_{15} &= \frac{\rho\left[2\rho^2 - (h_2^2 + h_3^2)\right]}{\sqrt{(\rho^2 - h_3^2)(\rho^2 - h_2^2)}} &\text{(II.53)}\\
L'_{23} &= \frac{\mu}{\sqrt{\mu^2 - h_3^2}} &\text{(II.54)}\\
L'_{24} &= \frac{-\mu}{\sqrt{h_2^2 - \mu^2}} &\text{(II.55)}\\
L'_{25} &= \frac{\mu\left[(h_2^2 + h_3^2) - 2\mu^2\right]}{\sqrt{(\mu^2 - h_3^2)(h_2^2 - \mu^2)}} &\text{(II.56)}\\
L'_{33} &= \frac{-\nu}{\sqrt{h_3^2 - \nu^2}} &\text{(II.57)}\\
L'_{34} &= \frac{-\nu}{\sqrt{h_2^2 - \nu^2}} &\text{(II.58)}\\
L'_{35} &= \frac{\nu\left[2\nu^2 - (h_2^2 + h_3^2)\right]}{\sqrt{(h_3^2 - \nu^2)(h_2^2 - \nu^2)}}. &\text{(II.59)}
\end{aligned}
$$

Note again that each row i in L' is associated with the Lamé function that depends on the respective variable η_i.

We now turn to the differentiation of B^m. Applying the chain rule of differentiation, we obtain

$$
\begin{aligned}
\frac{d}{d\eta_i}B^m &= \prod_{k=1}^{m}(\eta_i - \psi_k)\frac{d}{d\eta_i}\prod_{k=1}^{m}(\eta_i + \psi_k)\\
&+ \prod_{k=1}^{m}(\eta_i + \psi_k)\frac{d}{d\eta_i}\prod_{k=1}^{m}(\eta_i - \psi_k). \qquad \text{(II.60)}
\end{aligned}
$$

Expanding and factoring out the products on the right-hand side, we obtain the following expression:

$$
\begin{aligned}
\frac{d}{d\eta_i}B^m &= \sum_{d=1}^{m}\frac{1}{\eta_i + \psi_d}\prod_{k=1}^{m}(\eta_i - \psi_k)(\eta_i + \psi_k)\\
&+ \sum_{d=1}^{m}\frac{1}{\eta_i - \psi_d}\prod_{k=1}^{m}(\eta_i - \psi_k)(\eta_i + \psi_k). \qquad \text{(II.61)}
\end{aligned}
$$

It is useful now to define two functions ζ^+_{km} and ζ^-_{km}:

$$\zeta^{\pm}_{km} = \sum_{d=1}^{m} \frac{1}{(\eta_i \pm \psi_d)^k}. \tag{II.62}$$

Straightforwardly, we can also define a third function ζ_{km} as the sum of the two:

$$\begin{aligned} \zeta_{km} &= \zeta^+_{km} + \zeta^-_{km} \\ &= \sum_{d=1}^{m} \left[\frac{1}{(\eta_i + \psi_d)^k} + \frac{1}{(\eta_i - \psi_d)^k} \right]. \end{aligned} \tag{II.63}$$

It is worthwhile to note that $\zeta_{km} \equiv \zeta_{mk}$, i.e. permutation of the non-spatial indices k and m does not change the value of $\zeta_{km} B^m$. From this point forward, the subscript m of the ζ's will be suppressed for simplicity and we will write $\zeta_k \equiv \zeta_{km}$. Using the formalism described above, one can derive the following result by direct substitution of ζ_k into the expression for the derivative of B^m:

$$\frac{d}{d\eta_i} B^m = B^m \zeta_1. \tag{II.64}$$

This allows us to write the first derivative of the Lamé function using the simple formula

$$\frac{d}{d\eta_i} E^m_n(\eta_i) = \left(L_{ij} \zeta_{1m} + L'_{ij} \right) B^m. \tag{II.65}$$

We now have the tools required to derive $\boldsymbol{\nabla} \mathbb{E}^m_n(\rho, \mu, \nu)$. The form assumed by the gradient of the normal ellipsoidal harmonic function is far more complicated in ellipsoidal coordinates than it is in the Cartesian system. Nevertheless, this particular formulation is very important because of the separability property of the normal ellipsoidal harmonics in this coordinate system. Moreover, as will be made obvious in a future section, the simplicity associated with the definition of the ellipsoidal surface in this framework leads to numerous computational advantages, both analytic and numerical. Upon applying the gradient operator in ellipsoidal coordinates, we obtain the formula

$$\begin{aligned} \boldsymbol{\nabla}\mathbb{E}_m^n &= \mathbf{D}_{ij}\prod_{k=1}^{m}\Psi_k + L_{ij}\boldsymbol{\nabla}\prod_{k=1}^{m}\Psi_k && \text{(II.66)} \\ &= (\mathbf{D}_{ij} + L_{ij}\boldsymbol{\nabla})\prod_{k=1}^{m}\Psi_k, && \text{(II.67)} \end{aligned}$$

where $\{\mathbf{D}_{ij}\}$ denotes a 3×5 matrix with the following entries:

$$\begin{aligned} \mathbf{D}_{i1} &= \mathbf{0} && \text{(II.68)} \\ \mathbf{D}_{12} &= \frac{1}{s_\rho}\widehat{\boldsymbol{\rho}} && \text{(II.69)} \\ \mathbf{D}_{22} &= \frac{1}{s_\mu}\widehat{\boldsymbol{\mu}} && \text{(II.70)} \\ \mathbf{D}_{32} &= \frac{1}{s_\nu}\widehat{\boldsymbol{\nu}} && \text{(II.71)} \\ \mathbf{D}_{13} &= \frac{1}{s_\rho}\frac{\rho}{\sqrt{\rho^2 - h_3^2}}\widehat{\boldsymbol{\rho}} && \text{(II.72)} \\ \mathbf{D}_{23} &= \frac{1}{s_\mu}\frac{\mu}{\sqrt{\mu^2 - h_3^2}}\widehat{\boldsymbol{\mu}} && \text{(II.73)} \\ \mathbf{D}_{33} &= \frac{1}{s_\nu}\frac{-\nu}{\sqrt{h_3^2 - \nu^2}}\widehat{\boldsymbol{\nu}} && \text{(II.74)} \\ \mathbf{D}_{14} &= \frac{1}{s_\rho}\frac{\rho}{\sqrt{\rho^2 - h_2^2}}\widehat{\boldsymbol{\rho}} && \text{(II.75)} \\ \mathbf{D}_{24} &= \frac{1}{s_\mu}\frac{-\mu}{\sqrt{h_2^2 - \mu^2}}\widehat{\boldsymbol{\mu}} && \text{(II.76)} \\ \mathbf{D}_{34} &= \frac{1}{s_\nu}\frac{-\nu}{\sqrt{h_2^2 - \nu^2}}\widehat{\boldsymbol{\nu}} && \text{(II.77)} \\ \mathbf{D}_{15} &= \frac{\left[2\rho^2 - (h_3^2 + h_2^2)\right]\rho}{\sqrt{(\rho^2 - \mu^2)(\rho^2 - \nu^2)}}\widehat{\boldsymbol{\rho}} && \text{(II.78)} \\ \mathbf{D}_{25} &= \frac{\left[(h_3^2 + h_2^2) - 2\mu^2\right]\mu}{\sqrt{(\mu^2 - \rho^2)(\nu^2 - \mu^2)}}\widehat{\boldsymbol{\mu}} && \text{(II.79)} \\ \mathbf{D}_{35} &= \frac{\left[2\nu^2 - (h_3^2 + h_2^2)\right]\nu}{\sqrt{(\nu^2 - \rho^2)(\nu^2 - \mu^2)}}\widehat{\boldsymbol{\nu}}. && \text{(II.80)} \end{aligned}$$

Since we have already computed $dB^m/d\eta_i$ using our ζ operator approach, it is now easy to derive $\boldsymbol{\nabla}\prod_k^m \Psi_k$ because the factorized form of Ψ_k (see Eq. II.29) allows us to compute partial derivatives with respect to η_i very easily by holding terms of the form $(\eta_j^2 - \psi_k^2)(\eta_l^2 - \psi_k^2)$ constant, where $j \neq i$ and $l \neq i$. Thus, the same line of reasoning used for finding $dB^m/d\eta_i$ can be employed to compute the partial derivatives of $\prod_k^m \Psi_k$. The final result is given by

$$\boldsymbol{\nabla}\prod_{k=1}^{m}\Psi_k \;=\; \left[\frac{\zeta_{1m}(\rho)}{s_\rho}\widehat{\boldsymbol{\rho}}+\right]\prod_{k=1}^{m}\Psi_k, \qquad \text{(II.81)}$$

leading to the following expression for $\boldsymbol{\nabla}\mathbb{E}_n^m$:

$$\boldsymbol{\nabla}\mathbb{E}_m^n \;=\; \left\{\mathbf{D}_{ij} + L_{ij}\left[\frac{\zeta_{1m}(\rho)}{s_\rho}\widehat{\boldsymbol{\rho}} + \frac{\zeta_{1m}(\mu)}{s_\mu}\widehat{\boldsymbol{\mu}} + \frac{\zeta_{1m}(\nu)}{s_\nu}\widehat{\boldsymbol{\nu}}\right]\right\}\prod_{k=1}^{m}\Psi_k. \qquad \text{(II.82)}$$

This concludes our derivation of $\boldsymbol{\nabla}\mathbb{E}_n^m$ in the two coordinate systems of our choice.

Calculation of the potentials and fields

The mathematical theory of ellipsoidal harmonics is of great interest in a variety of scientific areas, including gravitational astrophysics [149] physical geodesy [54] and numerical analysis, e.g. for obtaining solutions to the ellipsoidal Stokes problem [147]. In biophysics, it is useful for computing the electric potential, electric field and magnetic field due to one or several quasistatic current dipoles located in an organ whose shape is approximately ellipsoidal, such as the human brain or stomach.

Consider a point $\mathbf{r}'$ located inside a body of volume V, where a primary current dipole source with moment $\mathbf{Q}$ is also located. The physics of this problem [158, 64] allows one to model the phenomenon at hand as a concentration of impressed current

$\mathbf{J}_i$ to a point $\mathbf{r}_0$ using the Dirac delta functional $\delta(\mathbf{r}-\mathbf{r}_0)$ via the algebraic expression

$$\mathbf{J}_i(\mathbf{r}) = \mathbf{Q}\delta(\mathbf{r}-\mathbf{r}_0). \tag{II.83}$$

The electric field $\mathbf{E}$ induced by the impressed current creates an induction current

$$\mathbf{J}_d(\mathbf{r}) = \sigma\mathbf{E}(\mathbf{r}), \tag{II.84}$$

where σ is the tissue conductivity. Since anatomical and physiological characteristics of the human body allow for such currents to be considered quasistatic [66, 111, 158, 164], the electric field is irrotational and Poisson's equation can be used to find the electric potential ϕ.

The formulas for ϕ due to dipoles located inside ellipsoids, spheroids and spheres were derived by Kariotou in [99]. For this reason, we discuss these theoretical results only to the extent that they are necessary for our own derivations. Nevertheless, it is important to take note of the fact that the expressions provided in [99] do not include ellipsoidal harmonic terms of degree 3 or higher because such terms require numerical evaluations of roots for the Lamé polynomials. In the present study, we provide a generalized numerical and theoretical method for computing the potential using a harmonic expansion of arbitrary degree and order.

In our ellipsoidal coordinate formulation, the general solution to Poisson's equation

$$\Delta\phi^{-}(\mathbf{r}) = \frac{1}{\sigma}\boldsymbol{\nabla}\cdot\mathbf{J}_i(\mathbf{r}),\ \ \mathbf{r}\in V^{-} \tag{II.85}$$

is a superposition of an interior harmonic function $\Phi(\mathbf{r})$ and of the function

$$\phi(\mathbf{r}) = \frac{1}{4\pi\sigma}\mathbf{Q}\cdot\boldsymbol{\nabla}_{\mathbf{r}_0}\frac{1}{|\mathbf{r}-\mathbf{r}'|}, \tag{II.86}$$

where the superscripts $(-)$ and $(+)$ denote quantitites referring to the interior and exterior, respectively, of the volume for which Poisson's equation is solved. The equation above is cited correctly in reference [44]. In Eqs. 38 and 40 of [99], however (both [44] and [99] have the same authors), $\boldsymbol{\nabla}_{\mathbf{r}_0}$ is replaced by $\boldsymbol{\nabla}$; this is most likely a typographic error because all the other theory in that reference based on this formula is derived correctly using $\boldsymbol{\nabla}_{\mathbf{r}_0}$ instead of $\boldsymbol{\nabla}$. Upon substitution of the formulas for the interior harmonic function and Laplace operator [113] into Eq. II.85, the interior potential assumes the form

$$\phi^-(\mathbf{r}) = b_0^1 + \sum_{n=0}^{\infty}\sum_{m=1}^{2n+1}\left\{b_n^m + \frac{1}{\sigma\gamma_n^m}\left[\mathbf{Q}\cdot\boldsymbol{\nabla}_{\mathbf{r}_0}\mathbb{E}_n^m(\mathbf{r}_0)\right]I_n^m(\rho)\right\}\mathbb{E}_n^m(\mathbf{r}) \tag{II.87}$$

The symbol b_n^m denotes the coefficient of the normal ellipsoidal harmonic functions $\mathbb{E}_n^m$, which is given [99] by the formula

$$b_n^m = \frac{1}{\sigma\gamma_n^m}\left[\mathbf{Q}\cdot\boldsymbol{\nabla}_{\mathbf{r}_0}\mathbb{E}_n^m(\mathbf{r}_0)\right]\left[\frac{1}{\alpha_1\alpha_3 E_n^m(\alpha_1)}\left(\frac{dE_n^m}{d\alpha_1}\right)^{-1} - I_n^m(\alpha_1)\right], \tag{II.88}$$

where differentiation of $dE_n^m/d\alpha_1$ is with respect to the argument α_1. As one can see, the interior potential is an infinite summation of terms involving the ellipsoidal harmonics $\mathbb{E}_n^m$. Substitution of the expression for b_n^m into the equation defining the potential and further manipulations yield the important formula

$$\begin{aligned}\phi^-(\mathbf{r}) &= b_0^1 + \sum_{n=1}^{\infty}\sum_{m=1}^{2n+1}\frac{1}{\sigma\gamma_n^m}\left[\mathbf{Q}\cdot\boldsymbol{\nabla}_{\mathbf{r}_0}\mathbb{E}_n^m(\mathbf{r}_0)\right]\mathbb{E}_n^m(\mathbf{r})\\ &\times\left[I_n^m(\rho) - I_n^m(\alpha_1) + \frac{1}{\alpha_2\alpha_3 E_n^m(\alpha_1)}\left(\frac{dE_n^m}{d\alpha_1}\right)^{-1}\right]\end{aligned} \tag{II.89}$$

A similar calculation for ϕ^+ [99] provides the following expression for the exterior potential:

$$\begin{aligned}\phi^{+}(\mathbf{r}) &= b_0^1 \frac{I_0^1(\rho)}{I_0^1(\alpha_1)} \\ &+ \sum_{n=1}^{\infty}\sum_{m=1}^{2n+1} \frac{I_n^m(\rho)}{I_n^m(\alpha_1)} \frac{\left[\mathbf{Q}\cdot\boldsymbol{\nabla}'\mathbb{E}_n^m(\mathbf{r}')\right]\mathbb{E}_n^m(\mathbf{r})}{\sigma\gamma_n^m\alpha_2\alpha_3 E_n^m(\alpha_1)} \left(\frac{dE_n^m}{d\alpha_1}\right)^{-1} \qquad \text{(II.90)}\end{aligned}$$

The value assigned to the real constant b_0^1 is entirely arbitrary and its presence is evocative of the fact that one can add any real constant to a scalar potential without affecting the result obtained when computing the potential difference between two points. In the next section it will be shown that setting this constant to 0 is computationally advantageous in the calculation of the magnetic field. Although the exterior potential involves the exterior harmonic functions $\mathbb{F}_n^m$, the potential can also be expressed only in terms of internal harmonics $\mathbb{E}_n^m$ since the former can be defined in terms of the latter. The expressions above were simplified analytically in [99] for ellipsoidal terms of first and second degree. In this section, however, we develop a more general model for obtaining solutions for an arbitrarily large expansion of harmonics.

Using the expressions for ϕ, we can derive corresponding formulas for the electric field $\mathbf{E}$ that apply both to the interior ($\mathbf{E}^{-}$) and to the exterior ($\mathbf{E}^{+}$) of the ellipsoid:

$$\begin{aligned}\mathbf{E}^{-}(\mathbf{r}) &= -\boldsymbol{\nabla}\phi^{-} \qquad \text{(II.91)} \\ &= -\sum_{n=1}^{\infty}\sum_{m=1}^{2n+1} \frac{1}{\sigma\gamma_n^m}\left[\mathbf{Q}\cdot\boldsymbol{\nabla}_{\mathbf{r}_0}\mathbb{E}_n^m(\mathbf{r}_0)\right]\boldsymbol{\nabla}\mathbb{E}_n^m(\mathbf{r}) \\ &\times \left[I_n^m(\rho) - I_n^m(\alpha_1) + \frac{1}{\alpha_2\alpha_3 E_n^m(\alpha_1)}\left(\frac{dE_n^m}{d\alpha_1}\right)^{-1}\right]. \qquad \text{(II.92)}\end{aligned}$$

Similarly, we obtain for $\mathbf{E}^+$

$$\begin{aligned}\mathbf{E}^+(\mathbf{r}) &= -\boldsymbol{\nabla}\phi^+ && \text{(II.93)}\\ &= -\sum_{n=1}^{\infty}\sum_{m=1}^{2n+1}\frac{I_n^m(\rho)}{I_n^m(\alpha_1)}\frac{\left[\mathbf{Q}\cdot\boldsymbol{\nabla}_{\mathbf{r}_0}\mathbb{E}_n^m(\mathbf{r}_0)\right]\boldsymbol{\nabla}\mathbb{E}_n^m(\mathbf{r})}{\sigma\gamma_n^m\alpha_2\alpha_3E_n^m(\alpha_1)}\left(\frac{dE_n^m}{d\alpha_1}\right)^{-1}. && \text{(II.94)}\end{aligned}$$

This completes our derivation of the electric potential and field.

Deriving a generalized expression for the magnetic field $\mathbf{B}$ is somewhat more tedious. Because much of the underlying theory required for this task has already been derived by Sarvas [158], we only summarize it here. The magnetic field due to some current density $\mathbf{J}$ is given by the law of Biot and Savart:

$$\mathbf{B}(\mathbf{r}) = \frac{\mu_0}{4\pi}\oint_{\Omega}\mathbf{J}(\mathbf{r}')\times\frac{\mathbf{r}-\mathbf{r}'}{|\mathbf{r}-\mathbf{r}'|^3}d^3\mathbf{r}', \tag{II.95}$$

where Ω is the support of $\mathbf{J}$ and μ_0 is the permeability of free space. An important detail concerning the formula above and the remainder of this section pertains to the difference between $\mathbf{r}'$ and $\mathbf{r}_0$. The variable $\mathbf{r}'$ refers to the integration space Ω, whereas $\mathbf{r}_0$ is related to the position of the dipole. Thus, $\mathbf{r}'$ is used in association with the current density $\mathbf{J}$ over the entire volume of the ellipsoid, whereas $\mathbf{r}_0$ is used for the current dipole that approximates this density. The conceptual differences associated with this aspect of the theory will be explained below in more detail. In the quasistatic approximation—which is justified here [158, 99, 44]—one of Maxwell's equation reads

$$\begin{aligned}\mathbf{J} &= \mathbf{J}_i+\mathbf{J}_d && \text{(II.96)}\\ &= \mathbf{J}_i+\sigma\mathbf{E}, && \text{(II.97)}\end{aligned}$$

where $\sigma\mathbf{E}$ is the Ohmic induction current previously described. Replacing $\mathbf{J}$ in

Eq. II.95 by the quantities on the right hand side above and using $\mathbf{E}^- = -\boldsymbol{\nabla}\phi^-$ yields the magnetic field as an integral over the volume V of the ellipsoid:

$$\mathbf{B}(\mathbf{r}) = \frac{\mu_0}{4\pi} \oint_V \left[\mathbf{J}_i(\mathbf{r}') - \sigma \boldsymbol{\nabla}\phi^-(\mathbf{r}')\right] \times \frac{\mathbf{r}-\mathbf{r}'}{|\mathbf{r}-\mathbf{r}'|^3} d^3\mathbf{r}'. \tag{II.98}$$

Using the definition of a current dipole $\mathbf{Q}$ located at $\mathbf{r}_0$ given before, i.e.

$$\mathbf{J}_i(\mathbf{r}) = \mathbf{Q}\delta(\mathbf{r}-\mathbf{r}_0), \tag{II.99}$$

it can be shown (see [158] for details) that the magnetic field is given by

$$\mathbf{B}(\mathbf{r}) = \frac{\mu_0}{4\pi}\mathbf{Q} \times \frac{\mathbf{r}-\mathbf{r}_0}{|\mathbf{r}-\mathbf{r}_0|^3} - \sigma\frac{\mu_0}{4\pi} \oint_{V^-} \boldsymbol{\nabla}\phi^-(\mathbf{r}') \times \frac{\mathbf{r}-\mathbf{r}'}{|\mathbf{r}-\mathbf{r}'|^3} d^3\mathbf{r}'. \tag{II.100}$$

From the formula above, one can see that the variable $\mathbf{r}_0$ is associated with the dipole location, whereas $\mathbf{r}'$ is used in the integral over the entire ellipsoidal volume, hence the difference between the two. One can apply Stokes' theorem to convert this integral into a surface integral, with the result

$$\mathbf{B}(\mathbf{r}) = \frac{\mu_0}{4\pi}\mathbf{Q} \times \frac{\mathbf{r}-\mathbf{r}_0}{|\mathbf{r}-\mathbf{r}_0|^3} - \sigma\frac{\mu_0}{4\pi} \oint_S \phi^-(\mathbf{r}')\widehat{\mathbf{n}} \times \frac{\mathbf{r}-\mathbf{r}'}{|\mathbf{r}-\mathbf{r}'|^3} dS'. \tag{II.101}$$

Our task is now to express the equation for $\mathbf{B}$ above in terms of normal ellipsoidal harmonic functions $\mathbb{E}_n^m$. The elliptic integrals I_n^m have been already defined in Eq. II.15. One can use the identity

$$\boldsymbol{\nabla}' \frac{1}{|\mathbf{r}-\mathbf{r}'|} = \frac{\mathbf{r}-\mathbf{r}'}{|\mathbf{r}-\mathbf{r}'|^3} \tag{II.102}$$

together with the result

$$\frac{1}{|\mathbf{r}-\mathbf{r}'|} = \sum_{n=0}^{\infty}\sum_{m=1}^{2n+1}\frac{4\pi}{\gamma_n^m}I_n^m(\rho)\mathbb{E}_n^m(\mathbf{r}')\mathbb{E}_n^m(\mathbf{r}) \tag{II.103}$$

derived in [44] to conclude that

$$\frac{\mathbf{r}-\mathbf{r}'}{|\mathbf{r}-\mathbf{r}'|^3} = \sum_{n=0}^{\infty}\sum_{m=1}^{2n+1}\frac{4\pi}{\gamma_n^m}I_n^m(\rho)\mathbb{E}_n^m(\mathbf{r})\boldsymbol{\nabla}'\mathbb{E}_n^m(\mathbf{r}'). \tag{II.104}$$

We can also compute the useful quantity

$$\begin{aligned}\mathbf{p} &\equiv \widehat{\mathbf{n}}\times\frac{\mathbf{r}-\mathbf{r}'}{|\mathbf{r}-\mathbf{r}'|^3} && \text{(II.105)}\\ &= D_n(\mathbf{r}')\sum_{n=0}^{\infty}\sum_{m=1}^{2n+1}\frac{4\pi}{\gamma_n^m}I_n^m(\rho)\mathbb{E}_n^m(\mathbf{r})\left[\widehat{\boldsymbol{\rho}}'\times\boldsymbol{\nabla}'\mathbb{E}_n^m(\mathbf{r}')\right]. && \text{(II.106)}\end{aligned}$$

The unit vector $\widehat{\boldsymbol{\rho}}'$ above comes from the definition of $\widehat{\mathbf{n}}$ in ellipsoidal coordinates given in Eq. II.41. This unit vector refers to the *surface* of the ellipsoid being integrated over in Eq. II.101; because the integration variable there is dS' as a function of (ρ', μ', ν'), the unit normal $\widehat{\mathbf{n}}$ is also a function of the primed variables. This is the motivation for writing $\widehat{\boldsymbol{\rho}}'$ rather than $\widehat{\boldsymbol{\rho}}$ in the expression above.

Before evaluating the integral over the closed surface in Eq. II.101, we note that its variable of integration is $\mathbf{r}'$. It was shown by Kariotou [99] that the exterior electric potential due to a dipole in the ellipsoid can be written as

$$\begin{aligned}\phi^-(\mathbf{r}) &= g_0^1 + \sum_{n=1}^{\infty}\sum_{m=1}^{2n+1}\frac{1}{\sigma\gamma_n^m}\left[\mathbf{Q}\cdot\boldsymbol{\nabla}_{\mathbf{r}_0}\mathbb{E}_n^m(\mathbf{r}_0)\right]\mathbb{E}_n^m(\mathbf{r})\\ &\times\left[I_n^m(\rho) - I_n^m(\alpha_1) + \frac{1}{\alpha_2\alpha_3 E_n^m(\alpha_1)}\left(\frac{dE_n^m}{d\alpha_1}\right)^{-1}\right],\end{aligned} \tag{II.107}$$

where g_0^1 is a constant. The only quantities in $\phi^-(\mathbf{r}')$ and $\mathbf{p}$ that are dependent on this variable are, respectively, $\mathbb{E}_n^m(\mathbf{r}')$ (from making the substitution $\mathbf{r} \to \mathbf{r}'$ in Eq. II.89) and $D_n(\mathbf{r}')\,[\boldsymbol{\rho}' \times \boldsymbol{\nabla}'\mathbb{E}_n^m(\mathbf{r}')]$. Thus constants and functions involving only $\mathbf{r}$ can be factored out from the integral. To ease our calculation, let us define the following functions:

$$\begin{aligned}
a_n^m(\mathbf{r}) &= \frac{4\pi}{\gamma_n^m} I_n^m(\rho)\mathbb{E}_n^m(\mathbf{r}) && \text{(II.108)}\\
b_n^m(\mathbf{r}') &= D_n(\mathbf{r}')\,[\widehat{\boldsymbol{\rho}}' \times \boldsymbol{\nabla}'\mathbb{E}_n^m(\mathbf{r}')] && \text{(II.109)}\\
c_n^m(\mathbf{r}_0) &= \frac{1}{\sigma\gamma_n^m}\mathbf{Q}\cdot\boldsymbol{\nabla}_{\mathbf{r}_0}\mathbb{E}_n^m(\mathbf{r}_0) && \text{(II.110)}\\
d_s^t(\rho;\alpha_i) &= I_s^t(\rho) - I_s^t(\alpha_1) + \frac{1}{\alpha_2\alpha_3 E_s^t(\alpha_1)}\left(\frac{dE_s^t}{d\alpha_1}\right)^{-1} && \text{(II.111)}
\end{aligned}$$

This allows us to write

$$\begin{aligned}
\phi^-(\mathbf{r},\mathbf{r}',\mathbf{r}_0) &= b_0^1 + \sum_{n=0}^{\infty}\sum_{m=0}^{2n+1}\mathbb{E}_n^m(\mathbf{r}')c_n^m(\mathbf{r}_0)d_n^m(\rho;\alpha_i) && \text{(II.112)}\\
\mathbf{p}(\mathbf{r},\mathbf{r}') &= \sum_{n=0}^{\infty}\sum_{m=0}^{2n+1} a_n^m(\mathbf{r})b_n^m(\mathbf{r}') && \text{(II.113)}
\end{aligned}$$

The integrand over the surface of the ellipsoid in Eq. II.101 can now be written as

$$\begin{aligned}
\phi^-\mathbf{p} &= b_0^1\sum_{n=0}^{\infty}\sum_{m=0}^{2n+1} a_n^m(\mathbf{r})b_n^m(\mathbf{r}')\\
&+ \sum_{n=0}^{\infty}\sum_{m=0}^{2n+1} a_n^m(\mathbf{r})b_n^m(\mathbf{r}')\sum_{s=0}^{\infty}\sum_{t=0}^{2s+1}\mathbb{E}_s^t(\mathbf{r}')c_s^t(\mathbf{r}_0)d_s^t(\rho;\alpha_i). && \text{(II.114)}
\end{aligned}$$

From a computational perspective, it is useful to assign the value 0 to the constant b_0^1 because this allows one to drop one infinite summation from the equation above. Carrying out the integration over the ellipsoidal surface for which $\rho = \rho_0$, we obtain

$$\oint_{\rho_0}\phi^-\mathbf{p}\,dS' = \sum_{n=0}^{\infty}\sum_{m=0}^{2n+1}\sum_{s=0}^{\infty}\sum_{t=0}^{2s+1} a_n^m(\mathbf{r})c_s^t(\mathbf{r}_0)d_s^t(\rho_0;\alpha_i)\oint_{\rho_0} b_n^m(\mathbf{r}')\mathbb{E}_s^t(\mathbf{r}')dS'. \tag{II.115}$$

Note the dependence of d_s^t on ρ_0 as a constant rather than on ρ as a variable since the value of this coordinate is constant on the surface. A simplification to the equation of the magnetic field given above comes from contracting the two infinite summations over n and s in the same equation using the convolution method for sequences that one can derive from Cauchy's product formalism [151]. This method, although typically used in the context of complex analysis for power series, is nevertheless perfectly applicable to real sequences. Therefore, recalling the Cauchy product formula

$$\left(\sum_{n=1}^{\infty} a_n\right) \cdot \left(\sum_{s=1}^{\infty} b_s\right) = \sum_{n=1}^{\infty}\sum_{p=1}^{n} a_{n-p} b_p, \tag{II.116}$$

we can relabel the subscripts in Eq. II.119 appropriately, and simplify our notation by defining the function

$$\zeta_{ns}^{mt} \equiv a_{n-s}^m(\mathbf{r}) c_s^t(\mathbf{r}_0) d_s^t(\rho_0; \alpha_i) \oint_{\rho_0} b_{n-s}^m(\mathbf{r}') \mathbb{E}_s^t(\mathbf{r}') dS'. \tag{II.117}$$

This leads us to the following expression for our integral:

$$\oint_{\rho_0} \phi^- \mathbf{p} dS' = \sum_{n=0}^{\infty}\sum_{s=0}^{n}\sum_{m=0}^{2(n-s)+1}\sum_{t=0}^{2s+1} \zeta_{ns}^{mt}. \tag{II.118}$$

In addition to making the notation more compact and easier to follow, this formulation removes the additional and unnecessary degree of freedom s from the double infinite summation for $\mathbf{B}$. The expression involving the magnetic field is given by

$$\begin{aligned} \frac{1}{\mu_0}\mathbf{B}(\mathbf{r}) &= \sum_{n=0}^{\infty}\sum_{m=1}^{2n+1} \frac{1}{\gamma_n^m} I_n^m(\rho) \mathbb{E}_n^m(\mathbf{r}) \left[\mathbf{Q} \times \boldsymbol{\nabla}_{\mathbf{r}_0} \mathbb{E}_n^m(\mathbf{r}_0)\right] \\ &- \sum_{n=0}^{\infty}\sum_{s=0}^{n}\sum_{m=0}^{2(n-s)+1}\sum_{t=0}^{2s+1} \zeta_{ns}^{mt} \end{aligned} \tag{II.119}$$

This can also be written in the elegant factorized form

$$\frac{1}{\mu_0}\mathbf{B}(\mathbf{r}) \;=\; \sum_{n=0}^{\infty}\sum_{m=1}^{2n+1}\left[\frac{1}{\gamma_n^m}I_n^m(\rho)\mathbb{E}_n^m(\mathbf{r})\mathbf{Q}\times\boldsymbol{\nabla}_{\mathbf{r}_0}\mathbb{E}_n^m(\mathbf{r}_0)-\sum_{s=0}^{n}\sum_{t=1}^{2(n-s)+1}\zeta_{ns}^{mt}\right], \tag{II.120}$$

which completes our derivation of the magnetic field.

A final remark is in place concerning the computational complexity of evaluating **B**. Upon examining the formulas for ϕ and **B**, it is not difficult to realize that calculating the magnetic field is the most computationally-intensive task (since it effectively involves two infinite summation even though the Cauchy summation formula can be used to remove one of them). Let u represent the degree of the highest term used in each expansion, i.e. the highest selected value of n, and let τ represent the time needed to compute either one of ϕ or **B** for some particular set of values for n and m. Using Big-Oh notation, computing ϕ and **E** requires $\sum_{n=1}^{u}(2n+1)\tau = (u^2+2u)\tau$, i.e. the algorithm is $\mathcal{O}(u^2)$. In the case of computing the magnetic field, there are two degrees of freedom because n and s can be chosen arbitrarily. If the assumption is made that the two are equal, we can let $\tau' \equiv (u^2+2u)\tau$ in the equation above and the algorithm is then found to be $\mathcal{O}(u^4)$. Thus the calculation of the magnetic field is significantly more intensive.

Figure II.1 depicts the results of a simple numerical study regarding the accuracy of the expansion in Eq. II.120. Physical parameter values (as specified in the caption) were selected so that the situation described resembles closely the experimental protocol of MGG or MEG (the case discussed is identical to that in [92], where images are also provided). What the figure demonstrates is that, for points located farther and farther away from the ellipsoid, the contribution of higher and higher order terms decreases. Close to the surface of the ellipsoid, however, these terms

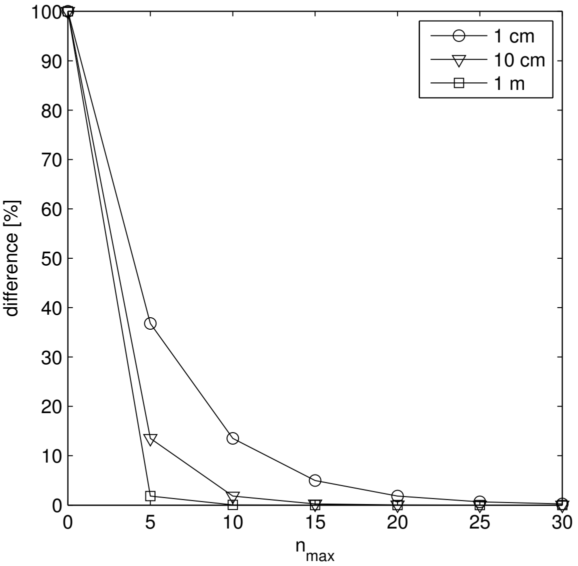

Figure II.1: Numerical accuracy results for the expansion in Eq. II.120. The independent variable n_{max} refers to the size of the expansion over n in Eq. II.120, i.e. $\mathbf{B}/\mu_0 = \sum_{n=0}^{n_{max}}(...)$. Let $\mathbf{B}(i)$ refer to the value of the magnetic field computed for an expansion over $n = 0, \ldots, i$. The quantity on the vertical axis was computed according to the formula $[\mathbf{B}(n_{max})$ - $\mathbf{B}(i)]/\mathbf{B}(n_{max})$. In other words, it represents the percentage difference between $\mathbf{B}(i)$ and the most accurate value of $\mathbf{B}$ that was computed for this numerical example, namely $\mathbf{B}(n_{max})$. The results presented are for an ellipsoid of dimensions $(\alpha_1, \alpha_2, \alpha_3) = (7.5, 5.0, 4.0)$ cm located at the origin (this is identical to the case discussed in [92], where images are also provided). The three curves represent values computed for a point A located on the Cartesian z axis at a distance of 1 cm, 10 cm and 1 m, respectively, from the upper extremity of the ellipsoid (i.e. the point on the surface of the ellipsoid closest to A).

can have a significant contribution. In conclusion, for applications where reasonable numerical precision is needed for the calculation of $\mathbf{B}$, a large expansion (n > 10) may be required. What this implies is that, if the ellipsoidal approximation to the brain or stomach is to be used effectively in similar simulation studies, low-order expansions (e.g. n < 3) may be insufficient.

Discussion

We can now summarize our algorithm proposed for the computation of ϕ, $\mathbf{B}$ and $\mathbf{E}$ using an ellipsoidal harmonic expansion of arbitrary order and degree. The generalized formulas for these three quantities are given in Eqs. II.89, II.90, II.92 and II.94. The constants γ_n^m can be evaluated numerically using Eq. II.22 as well as the formula for the surface differential dS specified by Eq. II.23. The normal ellipsoidal harmonic functions are given in both Cartesian (Eqs. II.24-II.26) and ellipsoidal (Eqs. II.27-II.29) coordinates. The gradient $\boldsymbol{\nabla}'\mathbb{E}_n^m$ can be computed using Eq. II.82 with inputs for $\{\mathbf{D}_{ij}\}$, $\{L_{ij}\}$ provided in Eqs. II.68-II.80 and II.28, respectively. Two other required formulas include the elliptic integrals I_n^m (which can be evaluated numerically using Eq. II.15) and the first derivative of the Lamé function (provided by Eq. II.65). Finally, the function D_n is specified by Eq. II.41.

A number of computational issues should be addressed with reference to the problem at hand. As explained in [99], ellipsoidal harmonics can be expressed analytically in terms of the α_i's only for $n \leq 3$ because higher-degree harmonic parameters lead to irreducible polynomial equations of cubic or higher degree. In this work, we choose to work only with the general formula for the ellipsoidal harmonics of arbitrary order and degree. According to a result by Stieltjes [145, 146], the Lamé function $E_n^m(\rho)$ has at most m real zeros $\psi_1, \cdots, \psi_m$, $m \leq 2n+1$, none of which are repeated. Because identifying all roots is algebraically impossible for polynomials of order 5 and higher, better approximations to the electric potential can be obtained only by implementing a numerical algorithm. To find the characteristic equations associated with Lamé polynomials, one must substitute the general expressions for $\mathbb{E}_n^m$ into the Laplace equation and write down the relations that must hold in order for this equation to be satisfied; the details of this process are demonstrated in detail by Hobson, whose work on ellipsoidal harmonics [72] is an excellent reference. After tedious manipulations, it can be shown that the set of characteristic equations is given by

$$\sum_{d=1}^{3} \frac{z_d}{\alpha_d^2 + \theta_p} + \sum_{q=1, q \neq p}^{m} \frac{1}{\theta_p - \theta_q} = 0, \tag{II.121}$$

where $\theta_1, \ldots, \theta_m$ are the m roots sought and the constants z_d have the values shown in Table II.1. The left-hand side in this set of equations is the logarithmic differential coefficient with respect to θ_p of the product

$$E_n^m = \prod_{p=1}^{m} (\alpha_1^2 + \theta_p)^{z_1} (\alpha_2^2 + \theta_p)^{z_2} (\alpha_3^2 + \theta_p)^{z_3} \prod_{q+p}^{m} |\theta_p - \theta_q|, \tag{II.122}$$

which is known as Stieltjes' formulation of the Lamé function. The system of equations defined above can be manipulated using an efficient method for solving nonlinear equations; for example, a subspace trust region method based on the interior-reflective Newton method [39, 40] was found by the author to exhibit excellent convergence behavior. In this approach, each iteration involves the approximate solution of a large linear system using the method of preconditioned conjugate gradients [40].

Numerical integration must be used to compute elliptic integrals of the form shown in Eq. II.15, as well as the constants γ_n^m. In the case of the I_n^m's, a simple analysis of the physical problem demonstrates that contributions to the integral are minute for values of the integration variable t greater than some constant multiple of α_1, i.e.

Table II.1: Values of the coefficients z_d, $d = 1, \ldots, 3$ in the characteristic equations of the Lamé polynomials

Function type	Value z_1	z_2	z_3
K	1/4	1/4	1/4
L	3/4	1/4	1/4
M	1/4	3/4	3/4
N	3/4	3/4	3/4

for $t > c\alpha_1$, where c is of $\mathcal{O}(1)$ and $c > 1$. Hence, the upper integration limit can be appropriately fixed in this case to a suitable value.

The results presented in this article show that the calculation of higher-order contributors to the electric potential and field in ellipsoidal geometry is a tedious and computationally-demanding task. This raises the question as to whether simpler techniques—such as the finite or boundary element methods—may be superior. This may indeed be the case for the forward problem of MEG or MGG; nevertheless, a certain important advantage associated with our method is not available in the BEM or FEM formalisms. This advantage refers to the fact that neither of the latter methods can clarify the issue as to how many higher-order contributors are necessary for accurate calculations of ϕ and $\mathbf{E}$ in the ellipsoidal formalism. Because of this, the issue of accuracy associated with the localization of sources from inverse procedures applied to MGG or fetal EEG data (see [62] and the discussion in [92]) cannot be settled only from an application of FEM or BEM. More research is therefore required to determine how appropriate the ellipsoidal model is in comparison with realistic models.

CHAPTER III

ELLIPSOIDAL MODELING OF GI SOURCES AND FIELDS

Introduction

Physiologically, electric fields in the human gut are produced by the exchange of ions between cells in the gastric smooth muscle. The movement of these ions creates electric currents that generate magnetic fields; although of the order of pT, these fields can be detected noninvasively using Superconducting QUantum Interference Device (SQUID) magnetometers.

To study GEA, one must become aware of how electric sources move along the body of the stomach during propagation. Numerous theoretical and computational models attempting to capture the characteristics of GEA have appeared in the literature [87, 120, 127, 137, 142], all falling into one of two broad categories, i.e. idealized or realistic. Idealized models have the advantage of simplicity since they allow both the forward and inverse problems to be studied with relative ease because both qualitative and quantitative judgments are more straightforward in idealized geometries. On the other hand, realistic models have the advantage of capturing various aspects of the modeling problem more vividly, which makes them very useful in a variety of real-life applications [30, 138, 142, 143].

The simplest of all idealized models describing GEA in the context of the quasistatic approximation to Maxwell's equations is the single-dipole model [23, 64, 87]. Although it makes use of significant simplifications of the actual phenomenon, this model has proved to be useful not only in GI modeling but also in the study of electrophysiology in other organs, most notably the brain [58, 64, 66, 125, 158, 186]. In the present chapter, a GEA model in ellipsoidal geometry is developed using current dipoles in the quasistatic approximation.

Computational approach

We adopt the approach of Kariotou [99] and compute the potential using only terms that involve polynomials of degree less than 3. The potential thus obtained is given by

$$\begin{aligned}
u^{-}(\mathbf{r}) &\approx b_0^1 + \frac{3}{4\pi\sigma}\sum_{m=1}^{3} Q_m x_m \left[I_1^m(\rho) - I_1^m(\alpha_1) + \frac{1}{\alpha_1\alpha_2\alpha_3}\right] \\
&- \frac{5}{4\pi\sigma\left(\Lambda-\Lambda'\right)}\sum_{m=1}^{3} Q_m x_{0m}\left[I_2^1(\rho) - I_2^1(\alpha_1) + \frac{1}{2\alpha_1\alpha_2\alpha_3\Lambda}\right]\frac{\mathbb{E}_2^1(\mathbf{r})}{\Lambda-\alpha_m^2} \\
&+ \frac{5}{4\pi\sigma\left(\Lambda-\Lambda'\right)}\sum_{m=1}^{3} Q_m x_{0m}\left[I_2^2(\rho) - I_2^2(\alpha_1) + \frac{1}{2\alpha_1\alpha_2\alpha_3\Lambda'}\right]\frac{\mathbb{E}_2^2(\mathbf{r})}{\Lambda'-\alpha_m^2} \\
&+ \frac{15}{4\pi\sigma}\sum_{\substack{i,j=1\\ i\neq j}}^{3} Q_i x_{0j} x_i x_j \left[I_2^{i+j}(\rho) - I_2^{i+j}(\alpha_1) + \frac{1}{\alpha_1\alpha_2\alpha_3\left(\alpha_i^2+\alpha_j^2\right)}\right]
\end{aligned} \tag{III.1}$$

Analogously, the formula for the exterior potential u^+ is given by

$$\begin{aligned}
u^{+} &\approx b_0^1\frac{I_0^1(\rho)}{I_0^1(\alpha_1)} + \frac{3}{4\pi\sigma\alpha_1\alpha_2\alpha_3}\sum_{m=1}^{3} Q_m x_m \frac{I_1^m(\rho)}{I_1^m(\alpha_1)} \\
&- \frac{5}{8\pi\sigma\alpha_1\alpha_2\alpha_3(\Lambda-\Lambda')}\times \\
&\times \sum_{m=1}^{3} Q_m x_{0m}\left[\frac{I_2^1(\rho)}{I_2^1(\alpha_1)}\frac{\mathbb{E}_2^1(\mathbf{r})}{\Lambda\left(\Lambda-\alpha_m^2\right)} - \frac{I_2^2(\rho)}{I_2^2(\alpha_1)}\frac{\mathbb{E}_2^2(\mathbf{r})}{\Lambda'\left(\Lambda'-\alpha_m^2\right)}\right] \\
&+ \frac{15}{4\pi\sigma\alpha_1\alpha_2\alpha_3}\sum_{\substack{i,j=1\\ i\neq j}}^{3} \frac{Q_i x_{0j} x_i x_j}{\alpha_i^2+\alpha_j^2}\frac{I_2^{i+j}(\rho)}{I_2^{i+j}(\alpha_1)}
\end{aligned} \tag{III.2}$$

As already noted, the formulae above involve only ellipsoidal harmonic terms of degree 1 and 2; this effectively constitutes an approximation of the expression for the total potential, which is an infinite summation of such terms. More on the possible effect of this approximation will be said in a future section.

We adopt a gain transfer matrix approach [126] to compute the electric potential due to dipoles located inside an ellipsoid. In this formulation, the vector $\mathbf{v}$ containing computed electric potential values at time j can be modeled as

$$\begin{aligned} \mathbf{v}(j) &= \sum_{i=1}^{p} \mathbf{G}(\mathbf{l}_i)\mathbf{q}_i(j) && \text{(III.3)} \\ &= \left[\mathbf{G}(\mathbf{l}_i) \cdots \mathbf{G}(\mathbf{l}_p)\right] \left[\mathbf{q}_1(j) \cdots \mathbf{q}_p(j)\right]^T && \text{(III.4)} \\ &= \mathbf{G}(\mathbf{l})\mathbf{q}(j), && \text{(III.5)} \end{aligned}$$

where the superscript T indicates the transpose of a matrix and

$$\mathbf{l} = \left[\vec{\mathbf{l}}_1 \cdots \vec{\mathbf{l}}_p\right]^T \qquad \text{(III.6)}$$

$$\mathbf{q} = \left[\vec{\mathbf{q}}_1 \cdots \vec{\mathbf{q}}_p\right]^T \qquad \text{(III.7)}$$

are column vectors that consist of concatenations of parameters for the p dipoles. The quantities $\vec{\mathbf{l}}_i$ and $\vec{\mathbf{q}}_i$ are 3-vectors indicating the locations and orientations of the dipoles, respectively. The matrix $\mathbf{G}$ is called the 'gain transfer matrix' for the ith dipole. If the dipole locations are kept constant while their orientations are varied with time, the model can be extended to capture the time-dependent variability of the sources. Thus, for n time points, we have

$$\begin{aligned} \mathbf{A} &= \left[\mathbf{a}_1 \cdots \mathbf{a}_n\right] && \text{(III.8)} \\ &= \mathbf{G}(\mathbf{l}) \left[\mathbf{q}_1 \cdots \mathbf{q}_n\right] && \text{(III.9)} \\ &= \mathbf{G}(\mathbf{l})\mathbf{Q}. && \text{(III.10)} \end{aligned}$$

In our problem, the entries in the gain transfer matrix are computed using the formulae for the potential presented in the previous section to obtain the potential due to each dipole at the required locations.

The geometry of our problem is shown in Fig. III.1. Each propagation cycle begins on the right-hand extremity of the ellipsoid (positive x) and the direction of propagation is the negative x direction. As shown in the figure, the paths assumed by the dipoles are directed longitudinally, along the greater dimension of the idealized gastric body. Each incremental time step during the propagation process brings about a change in the position of the activation front along the axis of propagation, as the image suggests. Distance increments in the activation front position along the propagation path are equal for all time segments. In other words, the longitudinal lines drawn from the positive to the negative extremity of the ellipsoid in the x direction correspond to the paths assumed by the current dipoles during propagation. The elliptic 'slices' whose lines are perpendicular to the direction of propagation correspond to the time points of the simulation. In our approach, 20 seconds are necessary for the simulated activation front to propagate from one end of the ellipsoid to the other.

To compute the appropriate locations of the dipoles during each cycle (based on the restriction that the distances between consecutive time points must be equal), the line (path) integral of each current dipole is computed along the direction of propagation, over the extent of each time segment involved. Since the path is a semiellipse as indicated by the geometry, the resulting expression assumes the form

$$\begin{aligned}\int_{t_1}^{t_2} ds &= \int_{t_1}^{t_2} \sqrt{1+\left(\frac{\partial y}{\partial x}\right)^2}\,dx \\ &= \int_{t_1}^{t_2} \sqrt{1+\frac{\alpha_2^2 x^2}{\alpha_1^4}\left(1-\frac{x^2}{\alpha_1^2}\right)^{-1}}\,dx, \qquad \text{(III.11)}\end{aligned}$$

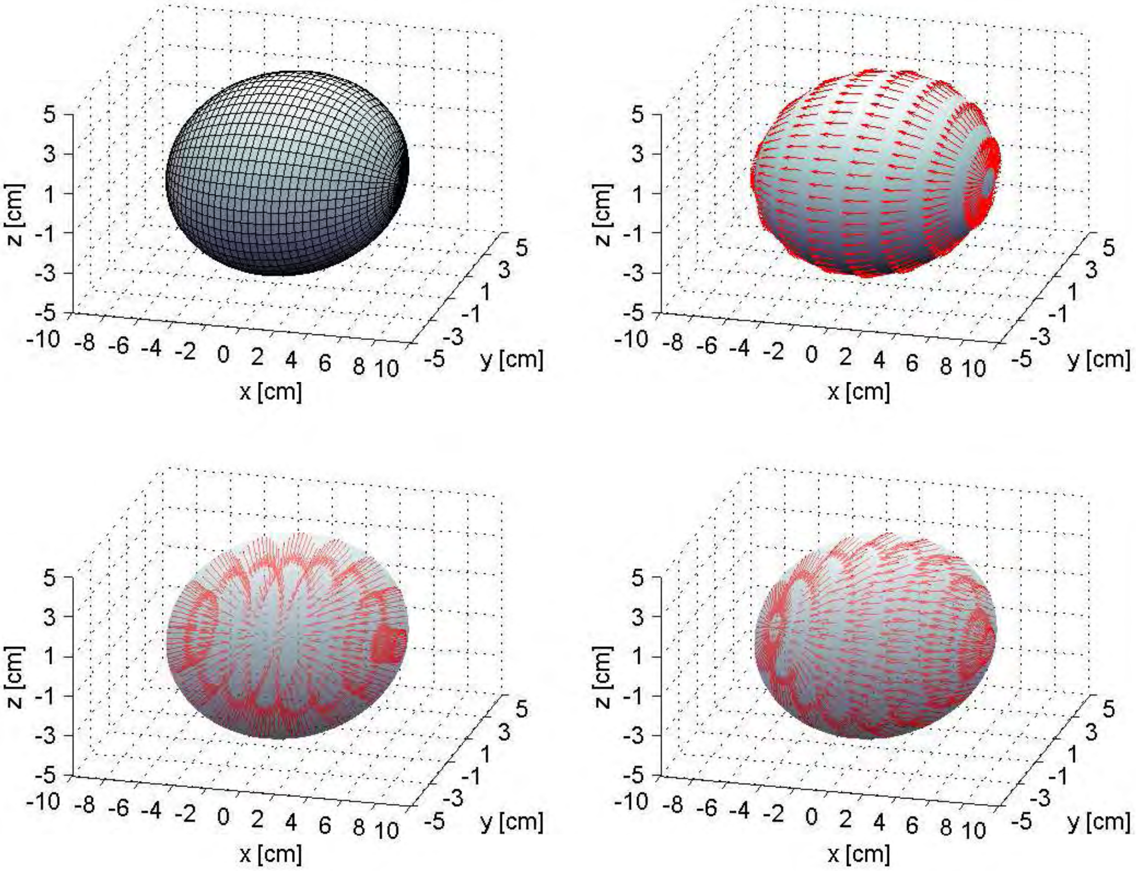

Figure III.1: Geometric models for the forward problem of electrogastrography. In these figures, the stomach is simulated as an ellipsoid with $(\alpha_1, \alpha_2, \alpha_3) = (7.5, 5.0, 4.0)$ cm. Propagation starts on the right hand side, from the extremity of the ellipsoid, and proceeds along the x axis in the negative x direction. In (a), only the mesh definition is shown. In (b), the propagation surface is shown with dipoles oriented in the direction of propagation. Each circular band of dipoles corresponds to a particular time point during the propagation cycle. For illustration purposes, dipoles are shown only for eight such equidistant time points. In (c), the dipoles are perpendicular to the propagation surface and in (d) the dipole vectors have a component that is parallel to the direction of propagation and another that is perpendicular to it. The body of the ellipsoid in (a) and (b) is opaque, whereas in (c) and (d) it is transparent so as to allow one to visualize the dipole vectors located inside the ellipsoid.

where ds is the path increment and $t_{1,2}$ are any two successive time points during the propagation cycle. In our computational approach, the integral above is computed numerically using Simpson's $\frac{1}{3}$ rule. This is also done for the elliptic integral in Eq. II.15, which is evaluated numerically. The values assumed for the ellipsoidal semiaxes are $(\alpha_1, \alpha_2, \alpha_3) = (7.5, 5.0, 4.0)$ cm and an experimentally measured value of 0.45 $1/\Omega \cdot$ m [23] is used for the conductivity σ of the gastric body.

Because the velocity of propagation along the gastric corpus varies from around 0.3 mm/s at the beginning of a cycle to approximately 4-5 mm/s at the end [120], this characteristic was also included into our model. Specifically, a linear dependence of the propagation velocity upon time was assumed for the purpose of our study and the initial and final velocities mentioned above were used to determine the appropriate velocity function. Because our dipoles travel along an ellipsoid and their trajectories are therefore semielliptical, the distances travelled by the dipoles were used to associate their locations during the simulation with corresponding time points during the propagation cycle. This was necessary because, although the distance increments used were the same due to our mesh definition (see Fig. III.1), the nature of the velocity function implies that the associated time increments are not. In computing the appropriate time intervals corresponding to equidistant points of successive displacement along the dipole trajectory, the elliptic perimeter p was calculated using the rapidly converging Gauss-Kummer series expansion, given by

$$\begin{aligned} p &= \pi(\alpha_1 + \alpha_2) \sum_{n=0}^{\infty} \begin{pmatrix} \frac{1}{2} \\ n \end{pmatrix}^2 \zeta^n \\ &= \pi(\alpha_1 + \alpha_2) \left(1 + \frac{\zeta}{4} + \frac{\zeta^2}{64} + \frac{\zeta^3}{256} + \cdots \right), \qquad \text{(III.12)} \end{aligned}$$

where

$$\zeta \equiv \left(\frac{\alpha_1 - \alpha_2}{\alpha_1 + \alpha_2} \right)^2 . \tag{III.13}$$

An interesting aspect of our problem concerns the orientation of current dipoles during the propagation cycle. In one view concerning this problem, dipoles are oriented inwards with respect to the surface of the ellipsoid, i.e. perpendicular to the surface of propagation. The motivation for this approach is the fact that the cellular exchange of ions in the stomach, mediated by the cells of Cajal, takes place between the concentric tissue layers of the stomach, hence the orientation of the dipoles should be inwards with respect to the propagation surface. The theoretical model capturing this view of the phenomenon was derived by Irimia & Bradshaw in a previous study [87], to which we refer the reader for the complete derivation. The expression predicting the orientation of current dipoles in this model is given by

$$-q_0 \frac{\boldsymbol{\nabla}\xi}{|\boldsymbol{\nabla}\xi|}, \tag{III.14}$$

where q_0 is in this case the assumed dipole strength $q_0 = |\mathbf{q}_0|$, $\boldsymbol{\nabla}\xi / |\boldsymbol{\nabla}\xi|$ is the normalized downward unit vector with respect to the ellipsoidal surface S, and ξ is a function whose gradient is perpendicular to S, such that Eq. III.14 is satisfied:

$$\xi(x_1, x_2, x_3) = x_2 - \alpha_2 \sqrt{1 - \frac{x_3^2}{\alpha_3^2} - \frac{x_1^2}{\alpha_1^2}}. \tag{III.15}$$

The second approach to this problem is based on the fact that propagation is observed in the stomach along the corpus and towards the pylorus and dipoles should therefore be oriented in the direction of propagation. This argument requires the computation of the unit tangent with respect to S, with a direction indicated by the direction of propagation along the surface.

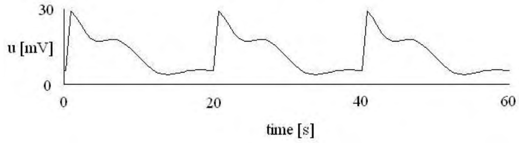

Figure III.2: The electric potential u simulated using the ellipsoidal model for a point located on the upper side of the ellipsoidal surface. The orientation of the dipoles used to produce this wave is parallel to the direction of propagation.

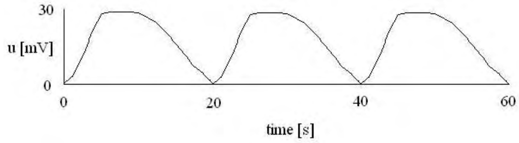

Figure III.3: Same as Fig. III.2, but the orientation of the dipoles is perpendicular (as opposed to parallel) to the direction of propagation.

To help clarify this issue, we have chosen to produce simulations using both models, in order to determine which one captures the characteristics of the GEA more suitably. In the first case, the dipole orientation function is computed analytically; in the second case, advantage is taken of the geometry and mesh definition shown in Fig. III.1 to compute the unit tangent vector numerically, using a simple interpolation algorithm. Finally, a third type of simulation was generated, in which the dipole orientation function is a linear combination with different weights of the two functions described above.

Results and discussion

Computational results of our simulations are presented in Fig. III.2 and Fig. III.3. The point for which the potential is evaluated corresponds, in both cases, to the extremity of the ellipsoid in the z (vertical) direction. Thus our waveforms attempt to reproduce the bioelectric potential as recorded on the upper extremity of the gastric wall. This simulated waveform agrees reasonably well with experiment and with other simulations obtained with various models (see, for example, [23]). Notable features are the presence of the upstroke followed by the sustained repolarization phase, two characteristics that have been observed experimentally and explained theoretically by activation models [23, 89]. In Fig. III.2, the orientation of the dipoles is along the direction of propagation, as opposed to Fig. III.3, where the dipoles are perpendicular to the ellipsoidal surface. The parallel dipole model waveform in Fig. III.2 is able to reproduce the upstroke that is characteristic of experimentally-recorded EGG, whereas the perpendicular-dipole model in Fig. III.3 is not. In addition to the two cases above, simulations were produced for the scenario where the dipoles had both a parallel ($\mathbf{Q}_p$) and a perpendicular ($\mathbf{Q}_r$) component with respect to the surface of propagation as in Fig. 1 (d), where the linear combination is given by

$$\mathbf{Q} = 0.8\mathbf{Q}_p + 0.2\mathbf{Q}_r. \tag{III.16}$$

The criterion for the choice of coefficients specified above was based on the physiology and anatomy of the problem. Thus, because the stomach wall is much thinner than it is long with respect to the propagation direction, the coefficient of the perpendicular dipole vector component was selected to be 0.2, i.e. smaller than the one for the parallel vector component, which was assigned the value 0.8. With this chosen linear combination of vectors, the resulting waveform was found to be very similar to the one in Fig. III.2; this is why, for brevity, it is not reproduced here.

Three-dimensional visualizations of the simulated gastric surface potential are shown in Fig. III.4, where the observed characteristics of the gastric electrical activity are simulated. To acquire a correct understanding of what is conveyed in this figure, it is necessary to analyze it by making close reference to Fig. III.2 because Fig. III.4 shows the evolution of the ellipsoidal surface potential as a function of time for the

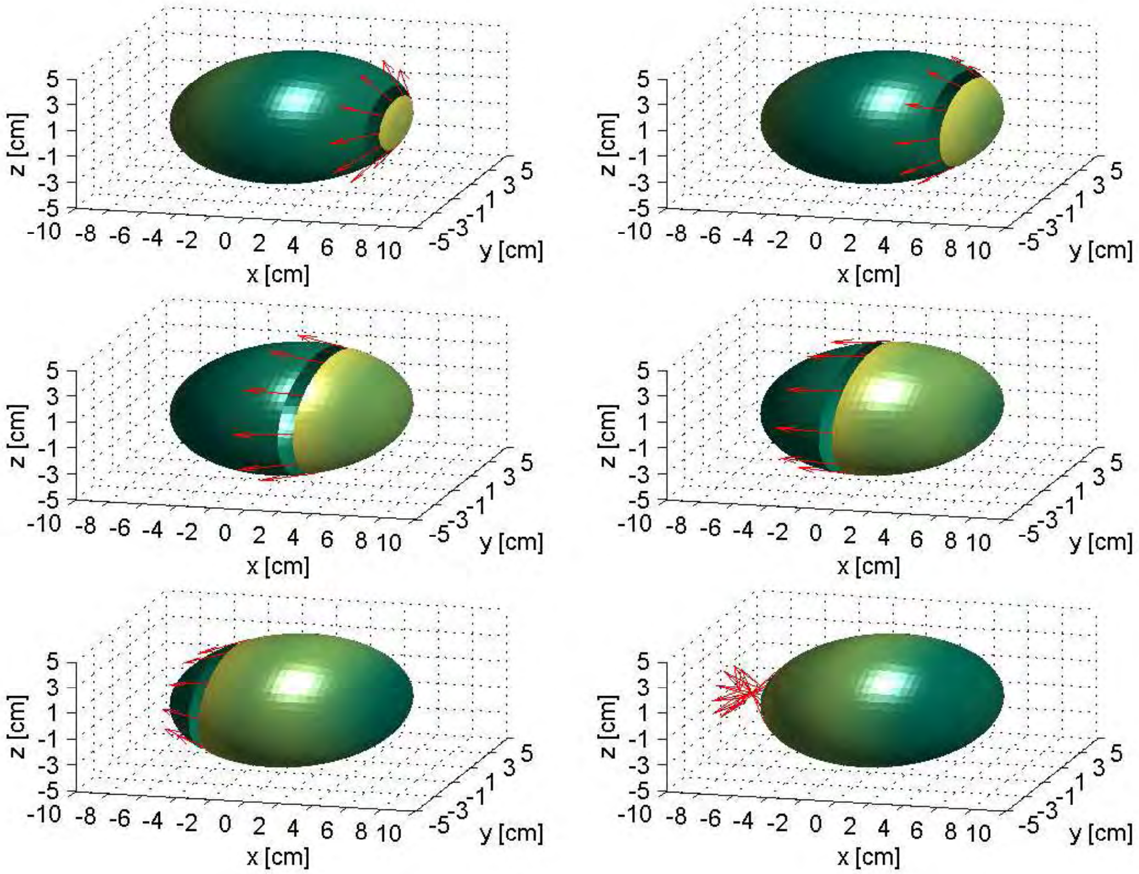

Figure III.4: Visualizations of the simulated electric potential on the surface of the ellipsoid throughout an ECA cycle of 20 seconds. The colormap varies from bright yellow at 30 mV to dark green at 0 mV. The time instants during the propagation cycle that correspond to each of the images in (a)-(f) are (left to right and top down) 3, 7, 10, 13, 17, and 20 seconds, respectively. In (a), the beginning of a propagation cycle is shown with the associated current dipoles drawn in red with orientations determined by the direction of propagation. The gastric pacemaker is located in this figure at the righ-hand extremity of the ellipsoid, in agreement with the physiological characteristics of the stomach. In (b)-(e), the band of dipoles advances along the gastric syncytium in the direction of the pylorus. In (f), the dipoles have reached the pylorus and can be seen as a concentration of red vector arrows at the left-hand extremity of the ellipsoid. On the opposite (right-hand) extremity, a new propagation cycle is about to begin.

parallel dipole model. Since the waveform simulated for this model is presented in Fig. III.2, a close relationship exists between the physical quantities depicted in these two figures. Each image in Fig. III.4 (a)-(f) depicts a snapshot of the ellipsoidal surface potential throughout the twenty-second propagation cycle. In each of these 3D plots, current dipoles are shown in red on the propagation surface with orientations specified by the direction of propagation. The dipoles are located on the isopotential ring where the electric potential reaches a maximum (bright yellow in the figures); this ring corresponds to the potential spike in Fig. III.2. In Fig. III.4 (a)-(f), one can also see an elliptic isopotential region immediately behind the ring of propagating dipoles. This band separates the dipole ring (which is at a maximum of the potential) from the portion of the ellipsoid located immediately after the band (where the potential decreases gradually from bright yellow to dark green). The portion of the separating band closest to the ring of dipoles corresponds to the resting potential plateau depicted in Fig. III.2. Finally, the region of zero potential lying in front of the dipoles on the left-hand side corresponds to the resting potential of the GI tissues after the passage of a dipole band in the previous cycle.

The ellipsoidal model is important at a theoretical level because it offers one of the very few geometries in which expressions for the electric potential and magnetic field due to current dipoles can be formulated analytically. This key aspect of theoretical GI modeling was emphasized in [87], where the ellipsoidal model was used to simulate the gastric electric potential throughout a typical GEA propagation cycle. To further our understanding of the GEA phenomenon, however, it is imperative to improve our knowledge−both qualitative and quantitative−concerning the spatial resolutions of different inverse methods in the context of EGG and MGG. This is important because, although we are now able to detect disease states of the gut, our understanding of pathological GEA remains limited; improved spatial resolution for inverse methods is thus critical for the study of GI processes at the tissue and even cellular level. In this context, the forward model presented in this article is relevant in view of future work in the area of inverse algorithm comparison and validation. To predict the possible diagnostic relevance of our model in the context of inverse modelling, it may be useful to consider the past use of ellipsoidal geometry in the area of fetal MEG (fMEG), where Gutiérrez *et al.* [62] employed an ellipsoidal head model to obtain both forward and inverse solutions that can characterize neural development in newborns. Their motivation for using the ellipsoidal model came from an earlier analysis by Vrba *et al.* [181], who had concluded that the spherical head model was superior to the uniform abdomen model in fMEG. However, because the sphere does not provide an accurate approximation to fetal head anatomy, the ellipsoid was chosen instead by the authors in order to increase the realism of their implementation as well as the ability of their model to capture important fMEG information. Thus, theirs is yet another example showing that the tendency to replace a simple idealized model with one that is more realistic is a powerful driving force in biophysical modelling. A line of reasoning analogous to that of Gutiérrez *et al.* quite possibly applies to the case of EGG, where the stomach has been modelled as a cylinder, cone or conoid [23, 120, 142, 143]. Such studies found that idealized models with closer and closer resemblance to gastric anatomy could offer greater and greater improvements in their ability to characterize normal and pathological conditions in humans [143]. Thus, although specific details regarding the superiority of the ellipsoidal EGG inverse model over other candidates are not currently available because inverse solutions have not yet been implemented for it, we believe that the ellipsoidal EGG model may nevertheless be very valuable in light of the arguments presented above. For example, we believe that the uncoupling of gastric electrical sources due to gastroparesis will be easier to characterize with our model than with a simpler, free-space dipole model, which has already been applied to human data with partial success [89].

To ensure the correctness, accuracy and complete agreement of our computational codes with the theory presented in the previous sections, all calculations were verified by hand for selected values of the electric potential. Because the theoretical model employed here makes use of a truncated infinite summation of ellipsoidal harmonic terms, we have sought to understand the effect of truncation upon the accuracy of the results obtained. In analogy with the theory of spherical harmonics as applied to Laplace's equation, one can expect that the contributions of harmonic terms to the potential should diminish as the order of these terms increases. For the case of a dipole in a sphere, this conclusion can be easily verified by inspection of the formulae for the potential that were first derived by Frank in 1952 [55] and later implemented, among others, by Purcell *et al.* [139], Schmidt and Pilkington [159], and He and Norgren [70]. For the sphere, the expressions for the potential involve, in a manner analogous to the ellipsoidal case, an infinite summation over spherical harmonic terms. However, these expressions have closed forms associated with them [55], which eliminates the need for truncating the infinite summations over spherical harmonics when the potential is evaluated. Furthermore, since closed form solutions are available, one does not have to worry about the issue of accuracy that must be taken into account when a truncated expansion is used. In the ellipsoidal case, closed form solutions are not available in the literature. This is a serious drawback because one is then forced to investigate the error associated with the ellipsoidal expansion used to compute the potential. For the problem at hand, expressions for the potential u involving higher-order harmonics (degree > 3) have not yet been derived (April 2005). As a result, we have attempted to address the issue of accuracy by investigating the extent to which first- and second-order terms contribute to u in our simulations. Because these

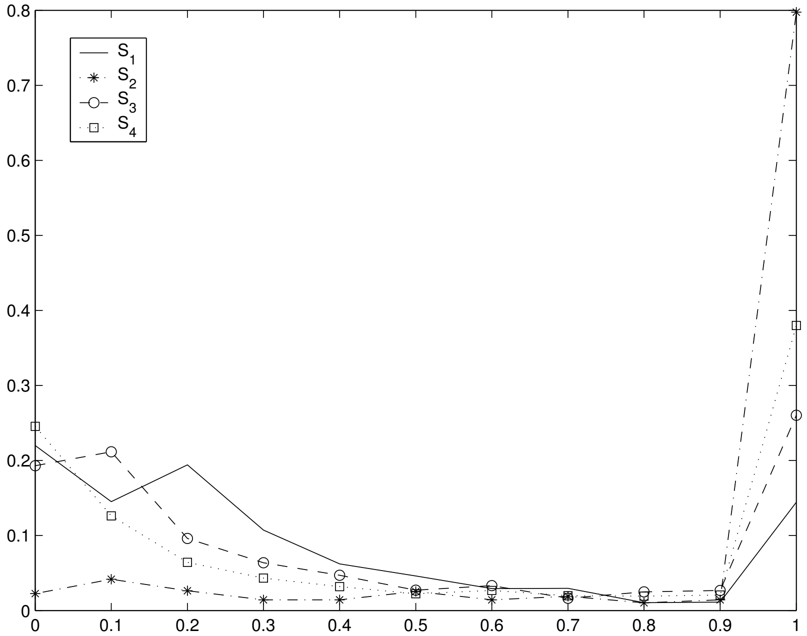

Figure III.5: Probability density functions for the magnitudes of ellipsoidal harmonic terms contributing to the potential u computed for the surface of the simulation ellipsoid. The terms S_i, $i = 1, \cdots, 4$ are the four summations (terms of order lower than 3) in Eq. III.1. Although lowest-order terms are important, the magnitudes of second-order terms are also non-negligible.

harmonic terms can be of either negative or positive sign, acquiring a quantitative understanding of how much higher- vs. lower-order terms contribute to the actual potential is a delicate matter due to the possible effect of cancellation between terms of identical or different order in Eq. III.1.

In light of these issues, we have chosen to compare the magnitudes of harmonic terms that contribute to each individual value of u computed during a typical simulation. The results of this quantitative comparison is presented in Fig. III.5. To produce this figure, we first normalized the magnitude of every harmonic term contributing to each value of u with respect to that contributor that had the highest magnitude. To explain this in mathematical notation, consider a computed potential value, call it u_1, given numerically by the four terms in Eq. III.1, i.e.

$$u_1 = b_0 + S_1 - S_2 + S_3 + S_4, \tag{III.17}$$

where S_1, S_2, S_3 and S_4 are the four summations (terms of order less than 3) in that equation. To compare the contributions of these terms to the potential, the values of S_i, $i = 1, \cdots, 4$ were normalized with respect to $\max\{S_i\}$. During our simulations, the values of these normalized harmonic terms were recorded for all values of the potential evaluated on the surface of the ellipsoid. Furthermore, the probability distribution functions for each of these terms were computed to acquire a quantitative understanding of how important they are to the evaluated potential.

In Fig. III.5, the probability distribution functions of the normalized harmonic terms are presented. As the figure demonstrates, there is a high probability that any of the terms included—regardless of their order—contributes substantially to the computed potential. This becomes apparent upon examination of the probability range [0.9, 1.0] in our figure. Another issue to be noted is that the significance of contributions by first- and second-order terms to the potential oscillates greatly between the two extremes. What this may imply is that, from a quantitative standpoint, both first- and second-order harmonic terms can be equally important in the evaluation of the potential, at least in the case of the problem at hand. To better understand our argument, it is useful to consider the same potential problem but for the case of the sphere, where the magnitudes of higher-degree contributors to the potential decreases rapidly as the degree of such terms increases. If this feature of the spherical problem were to be used to predict the behavior of high-degree terms in the ellipsoidal case at hand, one would expect that, overall, second-degree terms would contribute less than first-degree terms. This, however, is not what Fig. III.5 suggests. Letting f_k represent the probability density function associated with ellipsoidal terms of order k, Fig. III.5 makes it clear that the terms S_3 and S_4 associated with second-degree terms are important because the integral

$$\int_{0.9}^{1.0} f_k df \tag{III.18}$$

for $k = 2$ is comparable in magnitude with the same integral associated with the first-degree terms, for which $k = 1$. In other words,

$$\int_{0.9}^{1.0} f_1 df \sim \int_{0.9}^{1.0} f_2 df. \tag{III.19}$$

This means that, probabilistically, the contributors to the potential associated with the first- and second-degree terms are comparable in magnitude and that the spherical case does not provide a clear analogy with the ellipsoidal case. This may suggest that further theoretical and/or computational investigation is required in order to obtain expressions for u that include harmonic terms of degree higher than 2. Such work may help in clarifying how large the approximation (series truncation) error is for Eq. III.5 as derived in [99]. Finally, we note that the importance of high-order ellipsoidal harmonic terms was also emphasized by Sona, who demonstrated that such terms have a significant role when solving geodetic boundary value problems [165].

In our modeling case, higher-order harmonic terms may not significantly affect the simulated waveforms presented in this article from a qualitative standpoint. We believe this is the case because of the good qualitative agreement of our present results with experiment and previous studies that used other models. For example, a free-space dipole model [25] yielded waveforms very similar to ours; furthermore, both our present results and those in [25] are in agreement with earlier theoretical studies by Familoni *et al.* (who simulated the propagation of dipoles in cylindrical geometry [52, 53]) and even with the earlier study of Sarna *et al.*, who employed a coupled oscillator model [154]. Our theoretical results are also in agreement with a wide range of experimental results, ranging from a very early study by Bozler [19] conducted in 1945 to recent ones (2001-2004) by Zhu & Chen [191], Parkman *et al.* [135] and Horiguchi *et al.* [75], etc. Thus, higher-order contributors to the potential may not be essential when only forward modeling is concerned. However, the situation may be quite different in the case of inverse modeling. There, because of the ill-position of the inverse problem, small changes in the measured or simulated potential can cause significant changes in the reconstructed sources. The ellipsoidal expansion derivations of Kariotou were published in 2004 [99]. Already, a very recent study by Gutiérrez *et al.* [62] published in 2005 used the very same geometry and harmonic expansions to second order that were employed in this article to obtain inverse solutions from fetal magnetoencephalographic recordings. Since their approach was applied in the context of encephalography and involved a different number of dipoles with different activation patterns being studied, our observations regarding the issue of accuracy may not be directly applicable to their study; it would therefore be premature and ill-advised to criticize the accuracy of their results solely on this basis. However, we believe that our present study is timely and extremely important because our results can draw attention to the fact that the issue of ellipsoidal forward model accuracy is not entirely elucidated and needs further investigation. Solving this matter possibly involves the process of validating the use of inverse procedures in ellipsoidal geometry based on an analysis of the error associated with the number of harmonic terms included in the forward model.

Modeling the GEA using the ellipsoidal model is useful because it allows one to explore many important problems related to gastric physiology in a simplified and idealized geometry. Although the approximation errors associated with this formulation remain an open issue, we have shown here that the electric waveform simulated with this model is able to reproduce very well key characteristics of the GEA waveform. Future research will have to determine the optimal size of the ellipsoidal harmonic expansion to be included in the forward model when inverse solutions based on such a model are to be attempted.

CHAPTER IV

DETECTION OF GASTRIC ELECTRICAL RESPONSE ACTIVITY USING PCA

In humans and other mammals, GEA consists of (1) an electrical control activity (ECA) that can be recorded as an electrical slow wave and (2) an electrical response activity (ERA) that is characterized by spiking potentials during the plateau phase of the ECA. From a theoretical perspective, it was proposed by Sarna et al. that ECA can be modelled using a system of bidirectionally coupled relaxation oscillators [154, 155, 156]. Within the framework provided by this formalism, ERA was later shown to correspond to a bifurcation solution to the set of higher-order partial differential equations that describe the dynamics of this coupled gastric activation system [59, 28].

Thus far, ERA has only been detected in animals using EGG and the only human study available was performed with invasive serosal electrodes [77]. In 1995, Atanassova *et al.* recorded spiking activity from anesthesized dogs using implanted and cutaneous electrodes [9, 10]. In 1999, Akin and Sun recorded the spike activity of the canine stomach using EGG [1]. These authors concluded that ERA in serosal recordings occupies the frequency range of 50-80 cpm and later proposed an analysis method to extract the motility information from the EGG signal in the frequency range of ERA [2]. In 2001, Wang *et al.* investigated canine ERA using a blind source separation algorithm [182, 183, 184]. An increasing number of studies point to the possible use of ERA to identify and study gastric diseases. A study by Ouyang *et al.* involving electroacupuncture of the canine stomach used ERA to quantify the improvement of gastric emptying brought about by the procedure [133]. Another investigation by Garcia-Casado *et al.* used spike potential recordings made using surface electrodes to investigate and monitor intestinal mechanical activity in dogs

[56]. Finally, Xu *et al.* studied the effects of enhanced viscosity on canine gastric and intestinal motility from invasive ECA and ERA recordings [190].

The purpose of this chapter is to report the first noninvasive detection of ERA in humans and to show that significant differences in ERA patterns exist in pre- and post-prandial GEA. The application of principal component analysis (PCA) to magnetogastrographic recordings with the purpose of isolating and characterizing ERA patterns in the human stomach is demonstrated. In the following section, the PCA method is described and the noninvasive detection of ERA is demonstrated using the analysis of pre- and post-prandial ERA patterns recorded from 10 healthy human patients. Detecting ERA is useful in a clinical context because ERA characteristics can be used in a noninvasive way in order to differentiate between neurological and physiological causes of GI diseases.

Methods

MGG signals were recorded using the multichannel SQUID magnetometer in the Vanderbilt University GIST Laboratory. Informed consent was obtained from a healthy human volunteer and the study was approved by the Vanderbilt University Institutional Review Board. Subjects were positioned underneath the SQUID magnetometer inside the magnetically shielded room of the GIST Laboratory. Each volunteer was asked to suspend respiration and lie quietly for a period of at least one minute during each recording. For each recording, the magnetometer was oriented such that the coils measuring the $\hat{\mathbf{x}}$ and $\hat{\mathbf{y}}$ components of the signal tangential to the body surface were oriented in the sagittal and horizontal planes, and the coil measuring the $\hat{\mathbf{z}}$ component normal to the body surface was oriented in the frontal plane. Sample plots of the MGG signals recorded from one healthy subject are presented in Fig. IV.1.

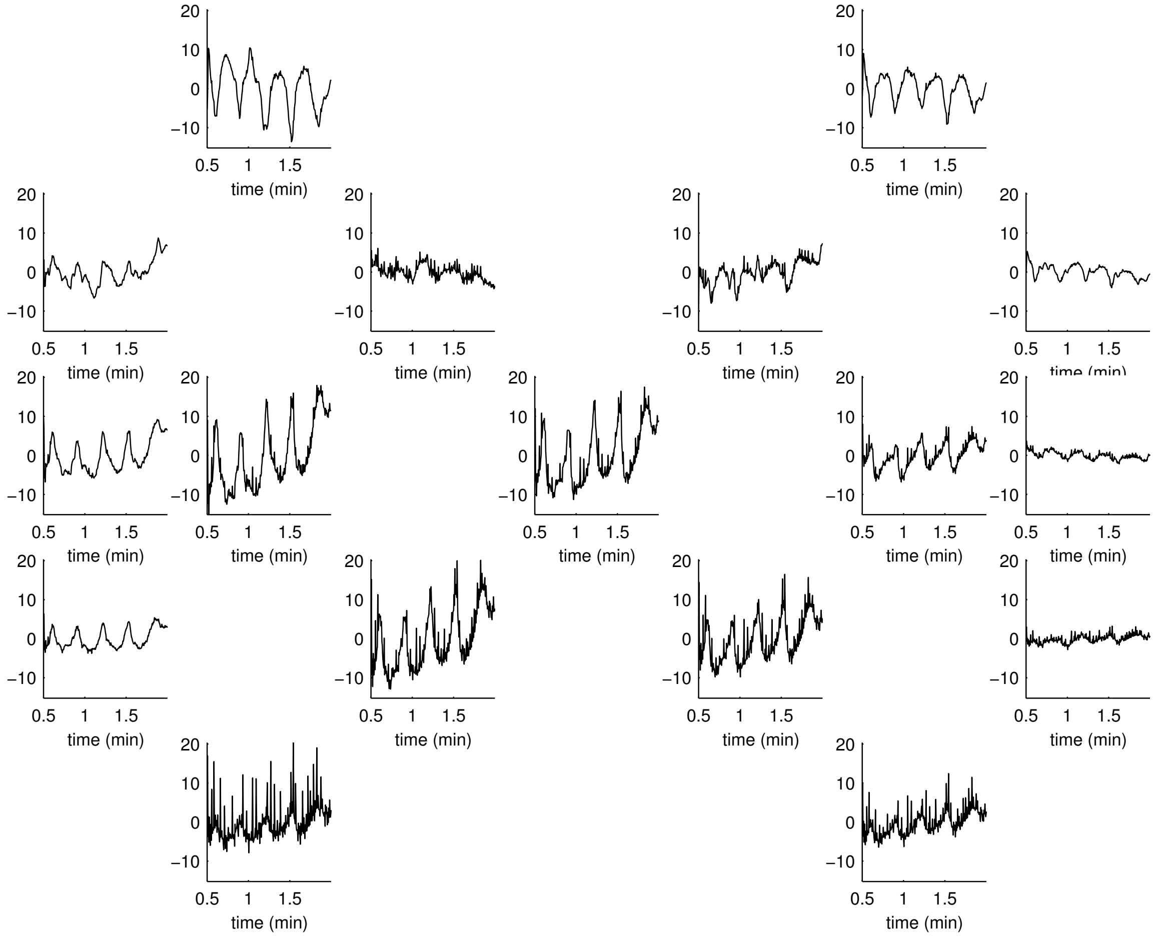

Figure IV.1: Sample raw MGG SQUID recording (B_z field component signals) acquired from a healthy human patient for a time interval of 1.5 minutes. Plots are shown in the approximate spatial arrangement of the SQUID magnetomer coils.

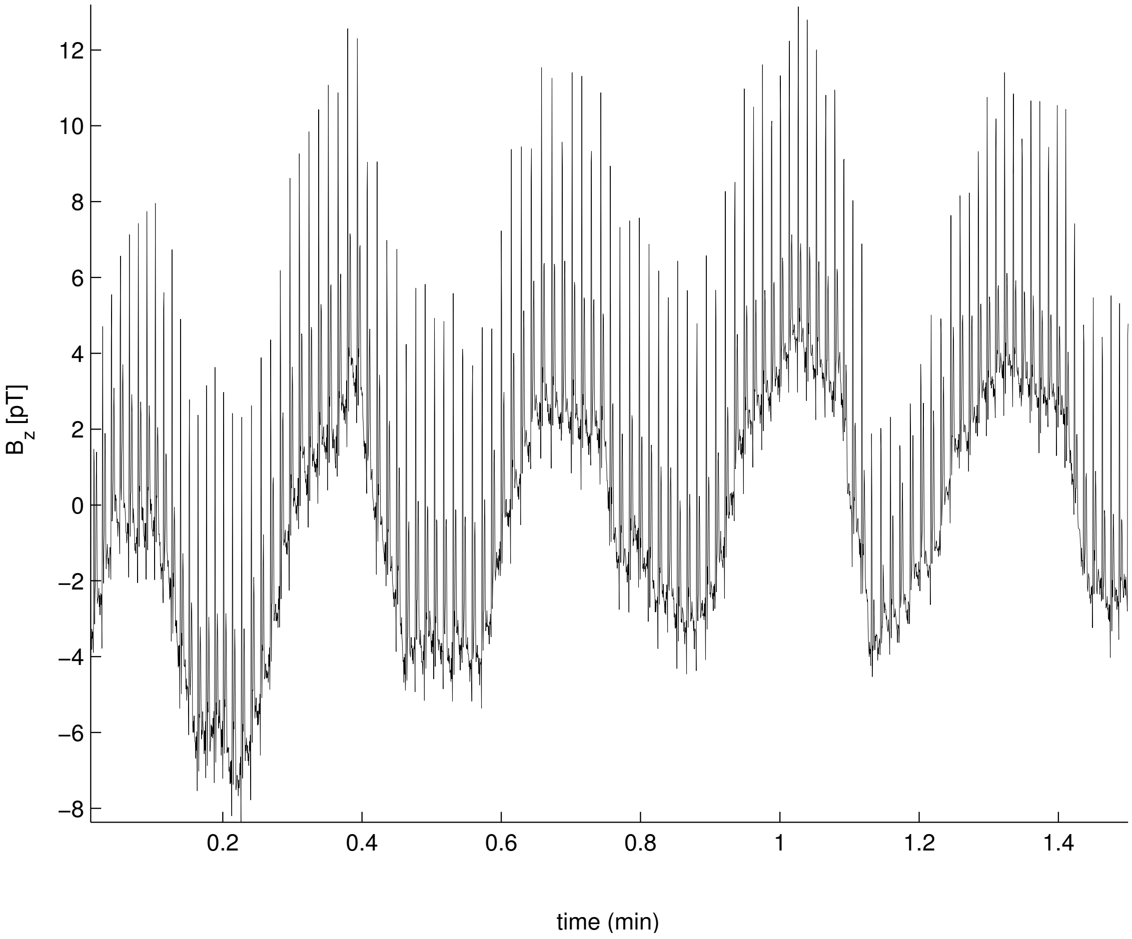

Figure IV.2: Selected gastric PC computed from the information provided by the signals in Fig. IV.1. The PC exhibits the characteristic waveform of ECA at a dominant frequency of 3 cpm.

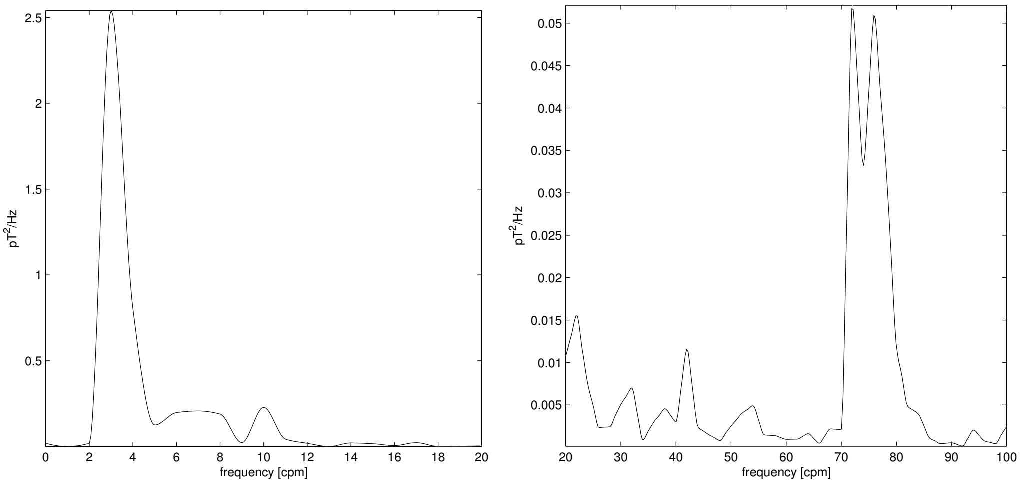

Figure IV.3: Frequency spectrum of the gastric PC in Fig. IV.2: (A) 1-20 cpm and (B) 20-100 cpm. The spectral energy present in the range 2-4 cpm corresponds to the gastric signal, whereas the peaks at 70-80 cpm is due to the cardiac artifact. A visual comparison of the ranges displayed on the vertical axes of the two plots (A) and (B) reveals that the gastric ECA signal is by far much stronger than both the respiration and cardiac artifacts. The power value associated with the highest peak in the frequency spectrum for the interval 100-500 cpm was found to be about 5×10^{-6} pT^2/Hz, which is significantly lower than both (A) and (B); this demonstrates that high-frequency components in this range contribute very little to the signal; for this reason, the associated plot for the interval 100-500 cpm is not reproduced for brevity.

PCA was employed to reduce the dimensionality of the acquired MGG recordings. After computing the PC's of an MGG data set, the so-called labeling problem of PCA must be addressed. This problem can be defined as the "task of finding substantive interpretations of some set of hypothetical latent variables which have been derived through PCA" [69]. In the case at hand, this translates into the challenge of associating one of the computed PC's with the gastric signal, which constitutes in this case the latent variable of interest. For the present study, the labeling problem was addressed using a visual analysis of the PC's that sought to identify the particular PC whose waveform best matched the gastric ECA waveform, which has a distinct frequency of 3 cpm. For the data set in Fig. IV.1, the selected PC is displayed in Fig. IV.2. As an aid to the decision process concerning the optimal PC to select, the power spectral density (PSD) of each PC was computed using the classical fast Fourier transform (FFT) and analyzed visually, thus providing a time-frequency representation of the MGG data. The frequency spectrum of the PC in Fig. IV.2 is shown in Fig. IV.3. For the data set in Fig. IV.1, the selected PC is displayed in Fig. IV.2. As an aid to the decision process concerning the optimal PC to select, the power spectral density (PSD) of each PC can computed using the classical fast Fourier transform (FFT) and analyzed visually, thus providing a time-frequency representation of the MGG data. The frequency spectrum of the PC in Fig. IV.2 is shown in Fig. IV.3.

After selecting a suitable PC, the signals provided by the chosen PC was processed for further analysis. First, linear detrending was applied to eliminate short-lived data trends due to extraneous causes, thus ensuring that low-frequency noise was eliminated. Then, a number of bandpass, second-order Butterworth filters are designed. The Butterworth filter is maximally flat in the pass band and monotonic overall, which reduces the effect of pass band ripples in the signal to a minimum. This type of filter sacrifices rolloff steepness for monotonicity in the pass- and stopbands. To generate each filter, z-transform coefficients were created for a lowpass digital Butterworth filter of order n with user-specified cutoff frequencies for each filter. Filter coefficients were specified in our approach in two rows a and b of length $n+1$, with coefficients listed in descending power of z:

$$\begin{aligned} H(z) &= \frac{A(z)}{B(z)} && \text{(IV.1)} \\ &= \frac{b(1) + b(2)\frac{1}{z} + ... + b(n+1)\frac{1}{z^n}}{1 + a(2)\frac{1}{z} + ... + a(n+1)\frac{1}{z^n}}. && \text{(IV.2)} \end{aligned}$$

Results

The cutoff frequencies used for our analysis and the resulting filtered waveforms obtained from the processing of the PC in Fig. IV.2 are presented in Fig. IV.4, where plots of magnetically recorded ECA and ERA are shown. It is well known that the ECG and MCG signals due to the human heart have characteristic components that are spread in a wide range of frequencies [38]. Thus, unavoidably, although the dominant frequency of the cardiac signal is around 75 cpm for the example in Fig. IV.4, the frequency ranges of ERA and MGG must overlap at least partially. For this reason, both signals are displayed using the method of Fig. IV.4 (C), where the cutoff frequencies for the Butterworth filter were 60-100 cpm. In that figure, the cardiac waveform can be seen in the time interval between 0.45-0.80 min. However, another signal is also present in Fig. IV.4 (C); this signal is both qualitatively and quantitatively different from the cardiac MCG signal and why this is the case is explained both below and by the analysis provided in Fig. IV.5.

1. the amplitude of the second signal identified in Fig. IV.4 (C) (i.e. the non-cardiac signal corresponding to the signal in Fig. IV.5 (C)) is twice as high as that of the MCG signal. The latter signal remained approximately constant throughout the

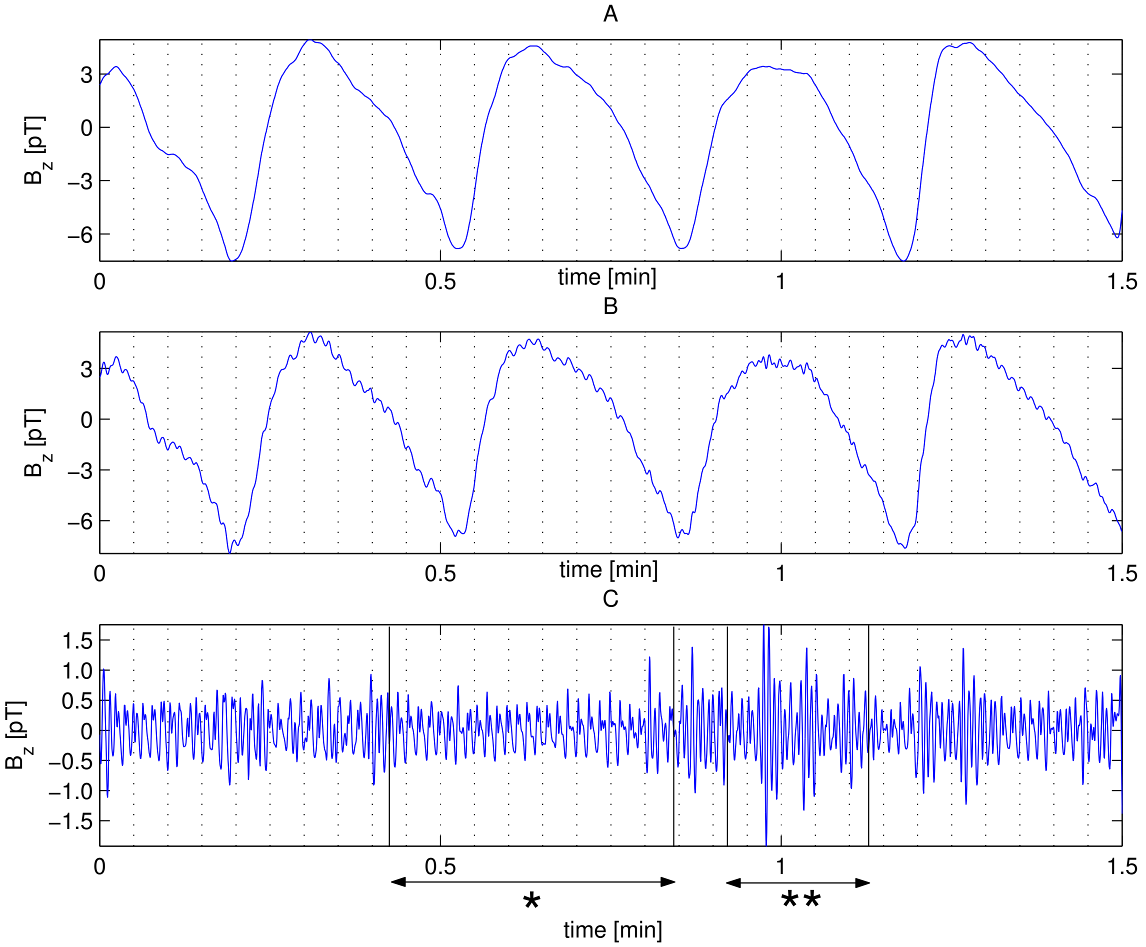

Figure IV.4: Human MGG and MCG recordings indicating the possible presence of ERA. Vertical grids are provided for convenience to emphasize the relationships that exist between the three waveforms. (A) gastric ECA waveform obtained from the gastric PC using a Butterworth filter with cutoff frequencies 1.8-40 cpm. (B) superimposed gastric (ECA *and* ERA) and cardiac (magnetocardiogram - MCG) signals obtained by applying a Butterworth filter with cutoff frequencies of 1.8-100 cpm to the PC. (C) superimposed gastric ERA and cardiac MCG signals obtained by applying a Butterworth filter with frequencies 60-100 cpm. The characteristic shape of the MCG signal is more evident throughout time segment 0.45-0.80 min, while the suspected ERA signal can be distinguished within time segments 0.20-0.45, 0.85-1.15 and 1.2-1.3 min. It can be noticed that ERA has a higher amplitude and a lower frequency than the MCG signal and that it appears only during the plateau phase (i.e. after the beginning) of the associated ECA wave. Signals plotted within time intervals [*] and [**] (delineated by vertical bars and horizontal arrows) are drawn separately and discussed further in Fig. IV.5.

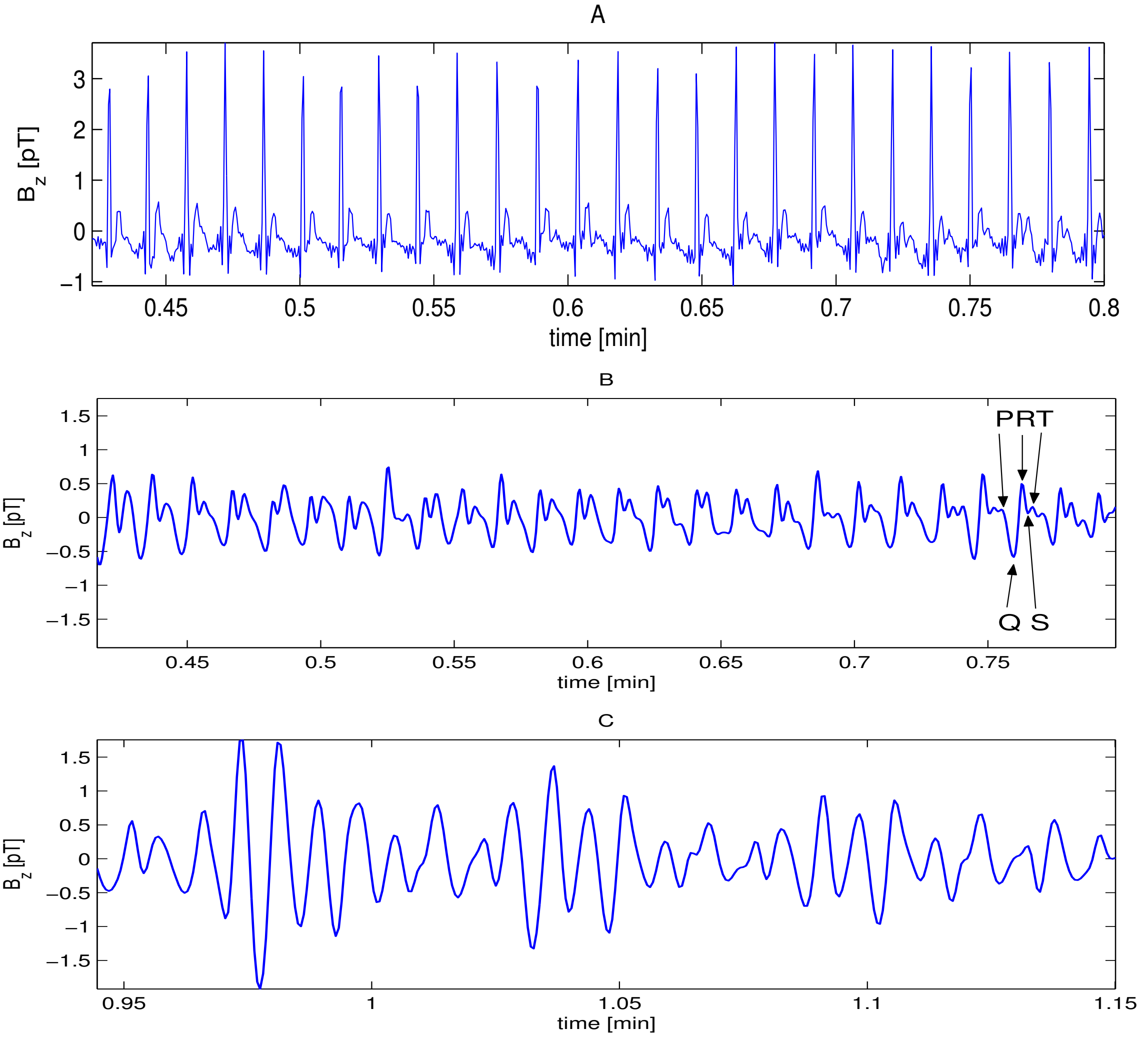

Figure IV.5: MCG (A,B) and suspected ERA (C) waveforms isolated from Fig. IV.4 (C). Time interval indications Time interval indications are identical to those in Fig. IV.4; note that the time scale in (A) and (B) differs from that in (C) because two different time intervals are displayed, i.e. (A) and (B) correspond to [*] in Fig. IV.4 while (C) corresponds to [**] in Fig. IV.4. Verticale scale intervals are the same in both (B) and (C) to emphasize the difference in magnitude between the MCG and ERA signals. In (A), the *unfiltered* cardiac PC is shown; because no filter was applied there, the magnitude of the signal is higher than in (B), where the *filtered* MCG signal for the same time period in (A) is nevertheless still identifiable; the P, Q, R, S and T waves that are characteristic of cardiac activity are labeled for a sample MCG interval. In (C), the ERA waveform is of greater magnitude and does not exhibit MCG characteristics. The fact that the MCG and ERA are out of phase with each other is indicated by the presence of an oscillating envelope associated the ERA signal, indicating again two distinct generating sources for the two phenomena.

entire analyzed time segment because the human subject lay still and did not move throughout the data acquisition process.

2. the waveform of the second identified signal differs categorically from the MCG waveform (see Fig. IV.5).

3. the non-cardiac signal was identified in the frequency range of 60-100 cpm, i.e. in approximately the same frequency range where ERA had been detected in animals (see, for example, [9, 1]).

4. Most importantly, the non-cardiac signal in Fig. IV.4 (C) is seen only during the plateau phase of the corresponding ECA waveform in Figure IV.4 (A). This can be demonstrated by analyzing time segments 0.20-0.45 min, 0.85-1.15 min and 1.2-1.3 min, where it is clear that the second identified signal appears on the plateau of the ECA wave. Thus the non-cardiac signal satisfies the properties of the ERA signal previously observed in canines and felines by a plethora of other GI researchers [9, 1, 182, 183]. It is reasonable to assume that human ERA would be seen in about the same frequency range because the depolarization and contractile mechanisms of the gastric muscles that are responsible for ERA are very similar for both humans and animals.

5. The second observed signal cannot be due to small or large intestine activities because the frequency ranges of these two types of electrical activity are far below the frequency range investigated here (i.e. 10-15 cpm for the small intestine and 8-12 cpm for the large intestine). In addition, skeletal muscle activity exhibits frequencies above the frequency range of 60-100 cpm investigated here and neither intestinal nor muscular activity are time-locked with the plateau phase of the ECA cycle.

In view of the reasons enumerated above, one can conclude that the non-cardiac signal in Fig. IV.4 (C) is generated by the ERA signal from the human stomach. This figure provides an example of what motivates our belief that we detected ERA from the MGG signal. Because our subjects lay still throughout the data acquisition process, there is no reason to consider the possibility of abrupt changes in the characteristics of the MCG signal for the time periods analyzed. One might argue, however, that the presence of the non-cardiac signal on the plateau phase of the ECA wave in Fig. IV.4 (point 4 above) is due to mere coincidence. In our analysis approach, however, this possibility was refuted in light of a statistical test applied to the 10 human MGG data sets used in our study. This test was applied as follows. First, a computer-based analysis identical to the one in Fig. IV.4 (A)-(C) was conducted for every human data set used in this study. Then, for each slow wave detected in a data set (Fig. IV.4 (A)), the associated plot analogous to the one in Fig. IV.4 (C) was analyzed and every non-cardiac signal detected using the analysis above was subjected to criteria (1), (2) and (3) above. It was then found that, when the non-cardiac signal fulfilled all these three criteria, it also fulfilled criterion 4 above in more than 19 out of 20 cases (confidence level $>$ 95%). Thus it is statistically reasonable to conclude that the appearance of our non-cardiac signal only during the plateau phase of the ECA is not a coincidence and that the signal is human ERA.

Postprandial changes in ECA patterns have been investigated by a number of authors. Terasaka *et al.* was among the first to show that that cellular coupling decreases post-prandially [172]. Postprandial changes in electrical control activity that are recordable from serosal and cutaneous EGG recordings have been investigated, among others, by Lin *et al.* [105, 106]. Prompted to investigate this phenomenon by the controversial interpretations that have been given to the postprandial increase in the dominant power of the EGG, these researchers concluded that exogenous stimulation−such as water ingestion− may change ECA amplitudes that are reflected in the EGG.

To study the effect of eating upon ERA characteristics, the analysis methods

Table IV.1: ERA analysis results for pre- and post-prandial human data (pre and post). Percentage differences were computed according to the formula (post−pre) × 100 / pre.

	ECA waves with ERA spikes(%)		
Subject	Pre-prandial	Post-prandial	Difference(%)
1	28	47	68
2	30	50	67
3	36	54	50
4	38	63	66
5	39	61	56
6	40	67	68
7	46	62	35
8	46	63	37
9	52	67	29
10	56	72	29
Mean	**41**	**61**	**47**

presented in the previous section were applied to the MGG data acquired from ten healthy human volunteers. Both pre- and post-prandial recordings were acquired for each patient and 20 minutes of recordings (10 of pre- and 10 of post-prandial data) were analyzed for each patient. After acquiring pre-prandial data, subjects were given a standard turkey sandwich and 300 ml of water, whereafter post-prandial data were acquired.

The results of our data analysis are summarized in Table IV.1. For each patient, the number of ECA waves was counted and the percentage of those waves that exhibited what we suspect to be ERA patterns detectable using our algorithm was also computed. The fact that the percentage of ECA waves with ERA activity is different from subject to subject is an indicator of inter-patient anatomical and physiological variability as well as other factors such as different signal-to-noise ratios for each experiment, small experimental setup differences, etc. Nevertheless, as a result of

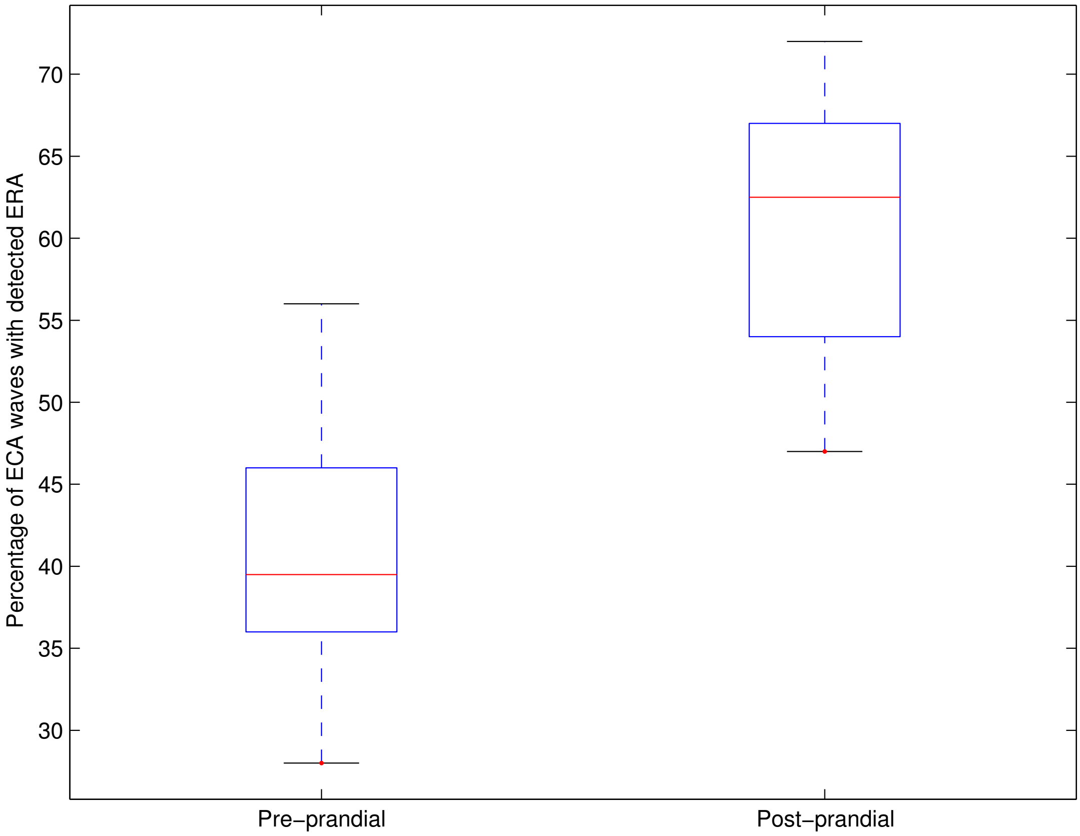

Figure IV.6: Box plot of post-prandial percentages of ECA waves exhibiting ERA vs. similar pre-prandial percentages. Horizontal lines indicate the mean (red), first and third quartiles (blue) and ranges (black) of the percentage values (no outliers were found). The statistical difference between the means of the two quantities plotted indicates that eating leads to a statistical increase in ERA ($p < 0.0001$).

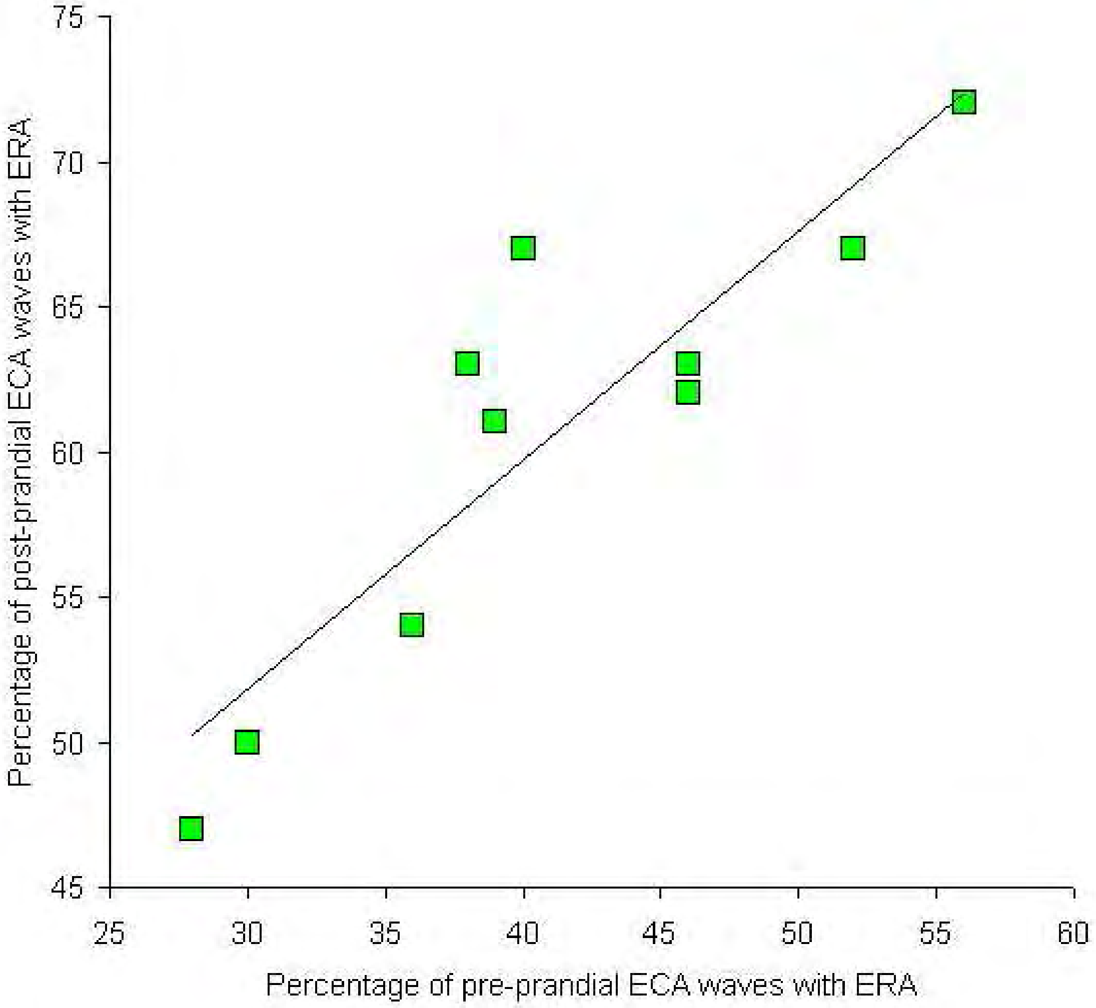

Figure IV.7: Plot of post-prandial percentages of ECA waves believed to exhibit ERA vs. similar pre-prandial percentages. The line of best fit in the least squares sense is also displayed. The fit to the data indicates that a linear increase in ERA amplitude is associated with eating.

applying a two-tailed paired t test, a statistically significant difference between pre- and post-prandial ERA recordings was found ($p < 0.0001$). This may be evidence that, as a result of eating, the amplitude of ERA increases by approximately one half of its pre-prandial value in normal humans. This conclusion is supported by the box plot in Fig. IV.7, where it can be seen that a statistical difference exists between pre- and post-prandial averages of ECA wave percentages with exhibited ERA.

A simple plot of the quantities in the third column of the table (post-prandial percentage) vs. those in the second table (pre-prandial percentage) is shown in Fig. IV.7. The least-squares line of best fit was computed using a nonlinear optimization algorithm. The result of applying this technique shows that a linear relationship between the two quantities (pre- and post-prandial percentages) is quite suitable. What this indicates is that the amplitude of ERA in the human stomach increases linearly from pre- to post-prandial recordings by approximately 50%. Whereas this is expected on physiological grounds because ERA is associated with the contractile behavior of the stomach (which increases post-prandially during digestion), this is the first study to report and quantify this increase in humans. Thus these results may represent an independent confirmation of the close relationship of direct dependence between ERA and the contractile activity of the gastric smooth muscle using the novel biomagnetic method of investigation. Moreover, the fact that this result could be obtained from our analysis without having treated it as an assumption throughout our investigation is an indicator in favor of biomagnetic method reliability.

The ECA patterns detected using our algorithm were found to exhibit a dominating frequency of 61.2 ± 2.4 cpm (mean ± SE, where the standard error SE of the sample was computed based on its standard deviation $\hat{\sigma}$ using the formula $\mathrm{SE} = \hat{\sigma}/\sqrt{n}$ where n=10 is the sample size). This value differs significantly from the dominating frequency of the cardiac signal, which was found to be 77.6 ± 1.7 cpm (mean ± SE).

What this may imply is that there is relatively little overlap between the frequency contents of the two signals, which is of course benefic from the standpoint of isolating and studying ECA during the analysis process.

An important issue to note at this point is that, since this is the first reported ERA detection from noninvasive MGG recordings, some type of independent validation of the results presented here must be obtained by means of a highly-reliable method such as invasive serosal recordings from humans. Although such recordings are not available in our case, one can state confidently that we have detected and analyzed a type of signal that is time-locked with the plateau phase of ECA and that we strongly believe to be a human ERA signal. To fully ascertain the validity of our claim, a future correlation study involving direct serosal or mucosal electrode recordings−which has been done before and is therefore a trusted method−and MGG recordings is necessary.

In conclusion, by means of a PCA of non-invasively acquired MGG signals, a biological signal with characteristics that strongly resemble those of gastric ERA in humans was detected. By analyzing the frequency spectrum of the gastric PC, suspected human ERA was found in the frequency range of 60-100 cpm, as well as post-prandial increases in the contractile activity of the smooth gastric muscle. The analysis technique employed opens a new avenue of investigation into the characterization of gastric diseases in man, including the possible future development of noninvasive methods of diagnosis that could potentially differentiate between gastric diseases of neurological and muscular origin based on the principal component analysis of ERA recordings.

CHAPTER V

BIOMAGNETIC SIGNAL EXTRACTION USING FAST ICA

Introduction

The artifact removal problem for magnetic fields recorded from GI electrical activity is at least as difficult as it is in electro- (EEG) and magneto-encephalography (MEG) or electro- (ECG) and magneto-cardiography (MCG). In the case of MEG compared to MGG, the head is positioned farther away from other organs that produce strong magnetic fields (such as the heart and abdomen) [66]. In MCG, the magnetic signal of the heart is quite strong compared to that of the surrounding organs, which is beneficial in terms of the signal-to-noise ratios of MCG experiments [42].

The stomach is positioned just below the diaphragm, which implies that respiration artifacts can be very strong if the subject is breathing. In the case of conscious humans, this problem can be partially addressed by asking subjects to hold their breath for specified periods of time [22]. This solution is not entirely satisfactory, as it significantly limits the length of data segments. Moreover, frequency analysis is very limited by the time length of the data segments, which may obscure bradygastria since its frequency is of about 0.5 cpm. Longer segments can be acquired while the subject is breathing; however, for such data to be easily analyzable, a method is required in order to address the respiratory artifact issue. Thus far, both conventional filtering [21] and adaptive respiration signal subtraction [134] have been implemented for MGG, but only with modest success. Conventional methods−such as Butterworth and Tchebyshev filters−are capable of removing respiration artifacts−albeit imperfectly−but, in doing so, they can also remove important biological information from the data [129]. Adaptive respiration subtraction can be implemented by subtracting a (scaled) respiration signal recorded in a reference sensor from channels that record magnetic data. However, the implementation of this method is problematic—to say the least—in realistic contexts because, while the frequency of the respiration signal recorded by the reference respiration channel may be identical to that recorded by the magnetic data channels, the waveform assumed by the respiration artifact signal can differ greatly across channels, which can make signal subtraction more problematic [180].

A major problem of MGG data acquisition is related to the presence of motion artifacts caused by small movements made by subjects in the waking state while data are being acquired. Very often, MGG measurements are made both pre- and post-prandially for periods of time of the order of hours. This is required because certain pathological changes in gastric activity as a result of eating occur only gradually in time, which can require lengthy data acquisition sessions [135]. In view of this, motion artifacts caused by movements of the human subject under the measurement apparatus are often unavoidable.

Another important problem consists of the fact that the gastric ECA signal is often obscured in MGG recordings by the presence of cardiac, muscular and/or intestinal artifacts, which can also reduce the quality of MGG signals. Although cardiac activity usually has its frequency peak between 60-80 cpm in resting humans (as opposed to the frequency peak of ECA, which is located around 3 cpm), the power spectrum of the cardiac signal does contain a large amount of energy in the low frequency range [38]. The same can be said about cardiac and intestinal signals because the dominating frequency of the latter is between 8-12 cpm, which is also in the range of low-frequency cardiac activity. Finally, the fact that respiration causes motion artifacts implies that SQUID sensors record magnetic field information at different positions with respect to the location of the stomach throughout the data acquisition process. This complicates the issue of applying inverse procedures with accuracy.

The purpose of this chapter is to describe and demonstrate the use of the fast independent component analysis (fast ICA) technique for the separation of the gastric signal from MGG data in the presence of severe motion, cardiac and respiratory artifacts. In the following section, an overview of the fast ICA algorithm is first given. Then, the application of fast ICA to an experimental MGG data set containing a significant amount of artifacts is illustrated. In particular, the isolation of the gastric signal as well as that of cardiac, respiratory and other motion artifacts is demonstrated. An accuracy analysis of the results is then carried out to conclude that the method is quite robust and appropriate for the analysis of MGG signals.

Methods

The MGG signals used here were recorded using the multichannel SQUID magnetometer in the Vanderbilt University GIST Laboratory. The study was approved by the Vanderbilt University Institutional Review Board. Human volunteers were positioned underneath the SQUID magnetometer inside the magnetically shielded room of the GIST Laboratory. Informed consent was obtained from each of these volunteers. Throughout the recording period, the magnetometer were oriented such that the coils measuring the $\hat{\mathbf{x}}$ and $\hat{\mathbf{y}}$ components of the signal tangential to the body surface were oriented in the sagittal and horizontal planes, and the coil measuring the $\hat{\mathbf{z}}$ component normal to the body surface was oriented in the frontal plane. Sample plots of the MGG signals recorded from one healthy subject in which substantial noise and artifact components are present are presented in Fig. V.1.

Fast independent component analysis (fast ICA) was employed to analyze MGG

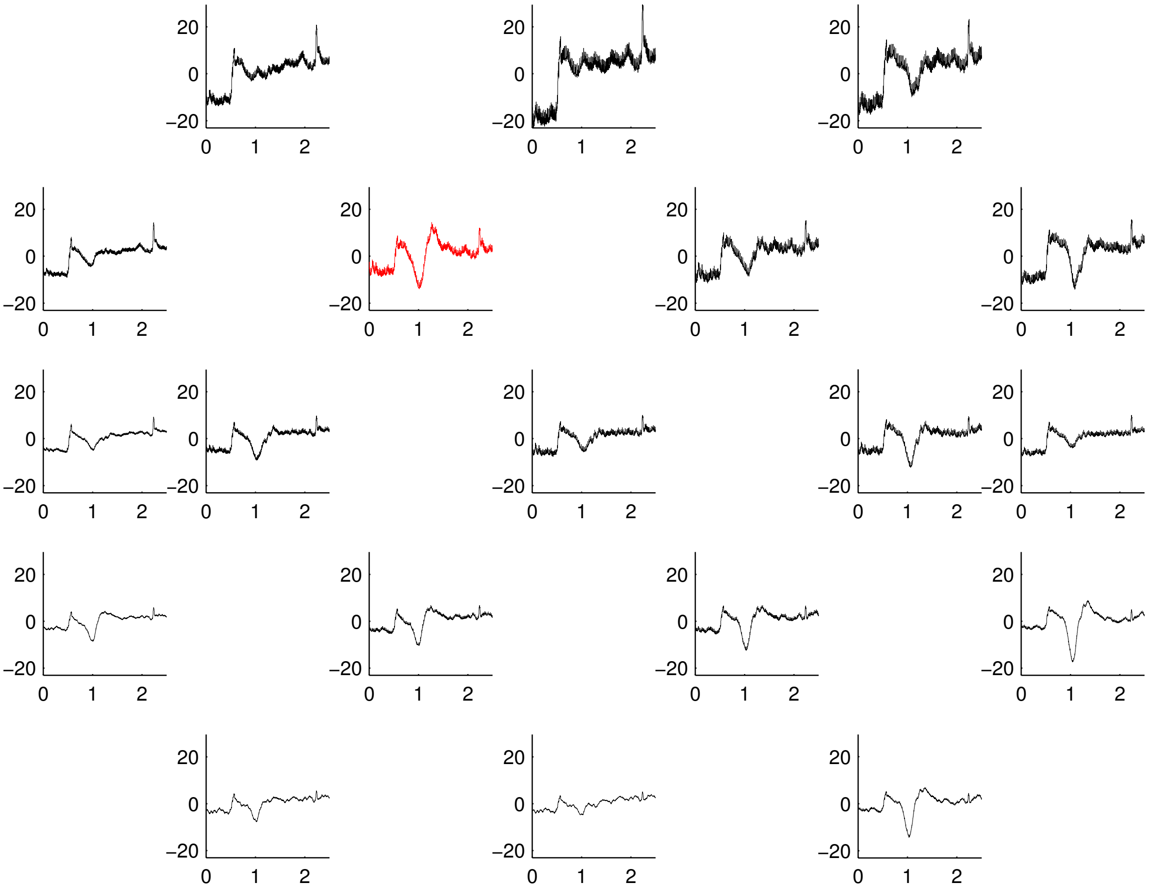

Figure V.1: Sample raw MGG SQUID recordings (B_z field component signals) acquired from a healthy human patient for a time interval of 2.5 minutes. Magnetic field values (pT) are plotted against time (minutes). Plots are shown in the approximate spatial arrangement of the SQUID magnetometer coils. The signal due to the stomach is not apparent from these recordings due to the presence of severe motion, cardiac and respiratory artifacts.

recordings from ten healthy adult human volunteers. Since ICA involves the computation of the covariance matrix of the MGG data—which can be (near)-singular—data dimensionality was reduced in our approach [91] using principal component analysis (PCA), whereafter the fast ICA algorithm described below was applied to the reduced data.

Originally introduced independently by Pearson in 1901 and by Hotelling in 1933, PCA is a multivariate analysis technique that attempts to describe the variation of a set of multivariate data in terms of a set of uncorrelated variables, each of which is a particular linear combination of the original variables [51]. The recorded MGG signal includes not only the gastric ECA and ERA, but also other underlying variables that can be considered, in our case, to be artifacts due to respiration, cardiac activity and to the rest of the GI tract (duodenum, small and large intestine). Each computed principal component (PC) of the MGG observation set is a linear combination of the underlying variables in that set. Specifically, they are those particular combinations which maximize the variances of each PC subject to the constraint of orthonormality. . Letting x_k represent one of these original n variables ($k = 1, ..., n$), the i-th PC y_i can be formally defined as

$$y_i = \sum_{k=1}^{n} \alpha_{ik} x_k, \tag{V.1}$$

where α_{ik} are the linear coefficients (weights) assigned to each variable x_k for the i-th PC y_i. In matrix notation,

$$\begin{aligned} \boldsymbol{x} &= (x_1, x_2, ..., x_n) && \text{(V.2)} \\ \boldsymbol{\alpha}_i^T &= (\alpha_{i1}, \alpha_{i2}, ..., \alpha_{in})^T && \text{(V.3)} \end{aligned}$$

where $\boldsymbol{\alpha}_i^T$ denotes the transpose of the column matrix $\boldsymbol{\alpha}_i$. The definition of y_i can now be written simply as

$$y_i = \boldsymbol{\alpha}_i^T \boldsymbol{x}. \tag{V.4}$$

In PCA, the i-th PC is that linear combination $\boldsymbol{\alpha}_i^T \boldsymbol{x}$ which maximizes the value of the variance var (y_i) subject to the orthonormality constraint specified by

$$\boldsymbol{\alpha}_i^T \boldsymbol{\alpha}_j = \delta_{ij}, \tag{V.5}$$

where δ_{ij} is the usual Kronecker delta function. The variance is computed from

$$\begin{aligned} \mathrm{var}(y_i) &= \mathrm{var}(\boldsymbol{\alpha}_i^T \boldsymbol{x}) \qquad \text{(V.6)} \\ &= \boldsymbol{\alpha}_i^T \boldsymbol{S} \boldsymbol{\alpha}_i, \qquad \text{(V.7)} \end{aligned}$$

where $\boldsymbol{S}$ is the variance-covariance matrix of the original variables. The optimization technique of Lagrange multipliers [123, 34] is applied in our approach to maximize the variance of each PC, which leads to the calculation of the eigenvectors of $\boldsymbol{S}$. These eigenvectors correspond to the eigenvalues of the variance-covariance matrix arranged in descending order according to their magnitude; thus the first PC can be interpreted as that linear combination of the original variables which maximally discriminates among a set of subjects. Z scores, defined as the data formed by transforming the original data into the space of the PC's, are also computed. An important statistic associated with PCA is Hotelling's T^2 statistic, which provides a measure of the multivariate distance of each observation from the center of the data set. In our computational approach, in addition to the PC's, we also compute Z scores, the eigenvalues of the covariance matrix as well as Hotelling's T^2 statistic for each time data point. After dimensionality reduction, the number of PCs that was retained was set to the number of input signals, which account for most of the explained variance in the data.

ICA is a data analysis technique that attempts to recover unobserved signals or 'sources' from observed mixtures, i.e. typically from the output of an array of sensors [33]. ICA has already been employed quite successfully in a variety of fields, including EEG [108, 109, 98], MEG [177, 178, 179], fetal ECG [102] and MCG [42]. In GI research, ICA was used by Wang *et al.* to blindly separate slow waves and spikes from invasive measurements of gastrointestinal electrical activity [182] in animals. In 2005, it was used by Liang [104] to extract the ECA waveform from invasive EGG measurements. Our study is the first one to demonstrate the use of ICA for noninvasive MGG gastric signal extraction.

Let x_1, x_2, ..., x_n be a set of n observed random variables expressed as linear combinations of another n random variables s_1, s_2, ..., s_n, i.e.

$$x_i = a_{i1}s_1 + a_{i2}s_2 + ... + a_{in}s_n = \sum_{j=1}^{n} a_{ij}s_j, \tag{V.8}$$

where $i = 1$, ..., n and $a_{ij} \in \mathbb{R}$. The s_i are assumed to be statistically mutually independent. Let $\mathbf{x}$ and $\mathbf{s}$ denote the random vectors containing the mixtures x_1, x_2, ..., x_n and s_1, s_2, ..., s_n, respectively and let $\mathbf{A}$ denote the matrix with entries $A_{ij} = a_{ij}$. The mixing model above can then be written simply as

$$\mathbf{x} = \mathbf{A}\mathbf{s}. \tag{V.9}$$

In terms of the formalism provided above, the task involved in ICA consists of finding $\mathbf{s}$ (in our case, the underlying gastric, cardiac, etc. signals) in terms of some given $\mathbf{x}$ (i.e. SQUID-recorded signals for our purposes) by identifying a suitable choice of the matrix elements of $\mathbf{A}$. We have used the fixed-point fast ICA algorithm of Hyvärinen as described in [79]. Since the details of this algorithm are extensively discussed elsewhere [81, 82, 83], the method is only summarized here.

Let the differential entropy H of a random vector $\mathbf{y} = (y_1, y_2, ..., y_n)^T$ with probability density function $f(.)$ be defined as

$$H(\mathbf{y}) = -\int \mathrm{d}\mathbf{y}\ f(\mathbf{y})\ \mathrm{ln} f(\mathbf{y}). \tag{V.10}$$

In the present case, the term entropy refers to the basic information-theoretic quantity for continuous one-dimensional random variables. The negentropy J can be interpreted as a measure of nongaussianity and can be defined as

$$J(\mathbf{y}) = H(\mathbf{y}_g) - H(\mathbf{y}), \tag{V.11}$$

where $\mathbf{y}_g$ is a Gaussian random vector of the same covariance matrix as $\mathbf{y}$. The mutual information I between the n scalar random variables y_i is a natural measure of the dependence between random variables that can be defined as

$$I(y_1, y_2, ..., y_n) = J(\mathbf{y}) - \sum_i J(y_i), \tag{V.12}$$

where

$$J(y_i) = H(y_{ig}) - H(y_i) \tag{V.13}$$

since y_i is a *scalar* random variable. The ICA of the random vector $\mathbf{x}$ can now be defined as the invertible transformation $\mathbf{s} = \mathbf{W}\mathbf{x}$ chosen in such a way that $I(s_1, s_2, .., s_n)$ is minimized. This is equivalent to the task of finding the direction in which negentropy is maximized. To achieve this, negentropy is first approximated in our approach

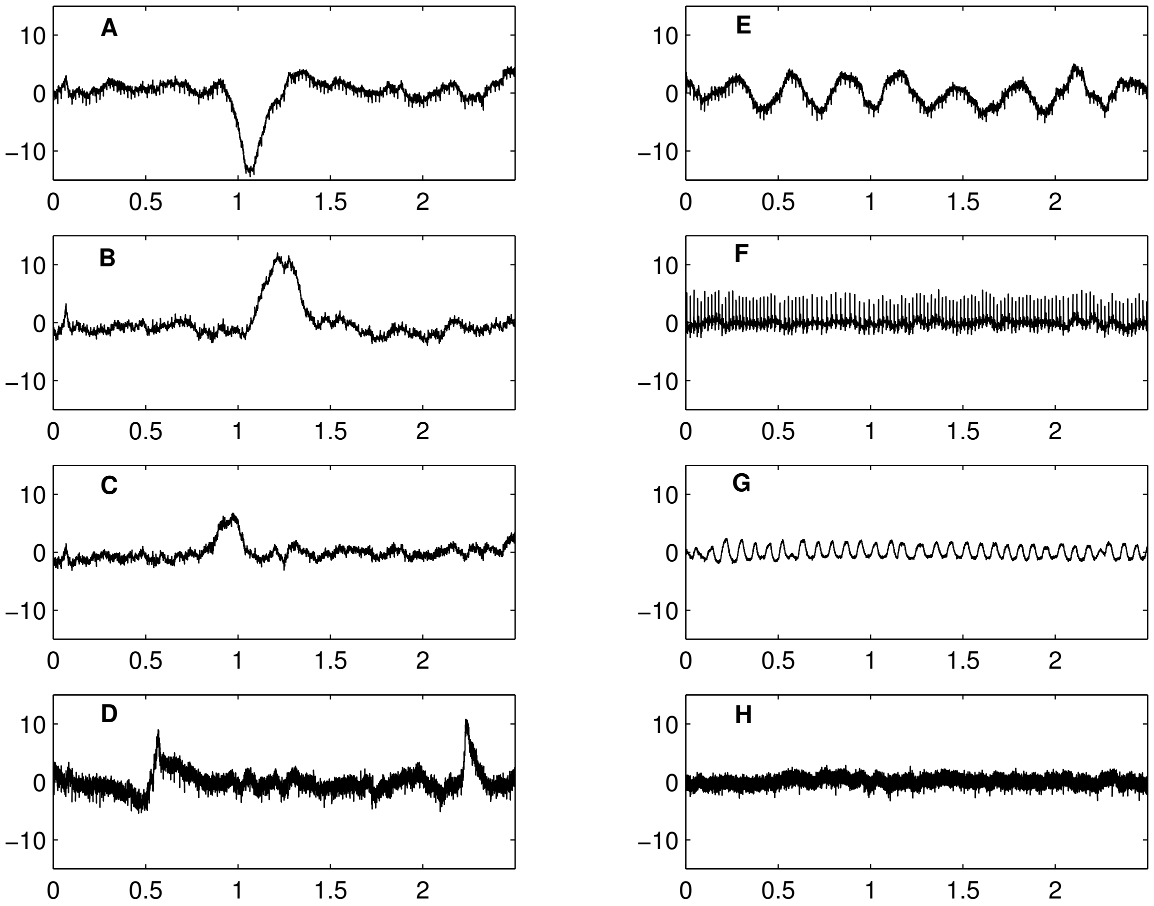

Figure V.2: ICs obtained from the SQUID data input in Fig. V.1. Magnetic field values (pT) are plotted against time (minutes). The ICs in (a), (b), (c) and (d) are believed to correspond to (partially overlapping) motion artifacts in the data while (e) shows the gastric slow wave of ECA that was isolated as a separate IC with a dominating frequency of 3 cpm. The ICs corresponding to cardiac activity and to respiration are presented in (f) and (g), respectively. High-frequency noise in the data was also isolated by fast ICA as a separate IC shown in (h).

using

$$J(\mathbf{w}) = [\mathrm{E}\ \{G(\mathbf{w}^T\mathbf{x})\} - \mathrm{E}\ \{G(\nu)\}]^2, \tag{V.14}$$

where E $\{.\}$ is the expectation operator, $\mathbf{w}$ is an m-dimensional weight vector subject to the constraint E $\{(\mathbf{w}^T\mathbf{x})^2\} = 1$, ν is a standardized Gaussian variable and G is the so-called contrast function (g and g' denote the first and second derivatives of G). Theoretically, G can be any non-quadratic form; however, three contrast functions are most commonly used, namely

$$\begin{aligned} G_1(u) &= \frac{1}{a_1} \ln \cosh(a_1 u) && \text{(V.15)} \\ G_2(u) &= -\frac{1}{a_2} \exp\left(-\frac{a_2 u^2}{2}\right) && \text{(V.16)} \\ G_3(u) &= \frac{u^4}{4}, && \text{(V.17)} \end{aligned}$$

where $1 \leq a_1 \leq 2$ and $a_2 \approx 1$ are constants. Our experience showed that most of the ICs isolated from our MGG data were sub-Gaussian; therefore, of the three functions above, G_3 was selected for our calculations because it is very suitable as a general purpose contrast function in such cases [14, 80, 82].

The task of maximizing negentropy can be rephrased as the goal of finding max $\{\sum_i J_G(\mathbf{w}_i)\}$, $i = 1, ..., n$, subject to the constraint E $\{(\mathbf{w}_j^T\mathbf{x})(\mathbf{w}_k^T\mathbf{x})\} = \delta_{jk}$, where δ_{jk} denotes the Kronecker delta function. In our fixed-point approach, after data sphering (whitening) has been performed, each new value of $\mathbf{w}$ (denoted by $\mathbf{w}^+$) is obtained iteratively from the old value of $\mathbf{w}$ (denoted by $\mathbf{w}^-$) using the formulae

$$\begin{aligned} \mathbf{w}' &= \mathrm{E}\ \{\mathbf{x}g(\mathbf{w}^{-T}\mathbf{x})\} - \mathrm{E}\ \{g'(\mathbf{w}^{-T}\mathbf{x})\}\ \mathbf{w}^- && \text{(V.18)} \\ \mathbf{w}^+ &= \frac{\mathbf{w}'}{||\mathbf{w}'||}, && \text{(V.19)} \end{aligned}$$

where $||\mathbf{w}'||$ indicates the Euclidian norm of $\mathbf{w}'$ and $\mathbf{w}^{-T}$ indicates the transpose of $\mathbf{w}^{-}$ (not to be confused with $(\mathbf{w}^{-1})^{T}$, i.e. the inverse of $\mathbf{w}$ taken to the power T). Because our form of the Hyvärinen algorithm makes use of the Newton-Ralphson method of convergence (which is not guaranteed), a stabilizing step is introduced in our approach so as to ensure its convergence.

The expression for the stabilizing step of the algorithm can be derived by making use of the Kuhn-Tucker conditions [107], according to which the optima of $\mathrm{E}\left\{G(\mathbf{w}^T\mathbf{x})\right\}$ under the constraint $\mathrm{E}\{\left(\mathbf{w}^T\mathbf{x}\right)^2\} = ||\mathbf{w}|| = 1$ are obtained at points where

$$\mathrm{E}\left\{\mathbf{x}g(\mathbf{w}^T\mathbf{x})\right\} - \beta\mathbf{w} = 0. \tag{V.20}$$

The symbol β used above denotes the quantity

$$\beta = \mathrm{E}\left\{\mathbf{w}^{-T}\mathbf{x}\, g\, (\mathbf{w}^{-T}\mathbf{x})\right\}. \tag{V.21}$$

To solve Eq. V.20 using Newton's method, one can label the left hand side of the equation above as a function F that must be set to zero. The Jacobian matrix JF of this function can be computed from

$$JF = \mathrm{E}\left\{\mathbf{x}\mathbf{x}'g'(\mathbf{w}^T\mathbf{x})\right\} - \beta\mathbf{I}, \tag{V.22}$$

where $\mathbf{I}$ is the identity matrix. Using the set of approximations

$$\begin{aligned} \mathrm{E}\left\{\mathbf{x}\mathbf{x}'g'(\mathbf{w}^T\mathbf{x})\right\} &\approx \mathrm{E}\left\{\mathbf{x}\mathbf{x}^T\right\}\mathrm{E}\left\{g'(\mathbf{w}^T\mathbf{x})\right\} && \text{(V.23)} \\ &\approx \mathrm{E}\left\{g'(\mathbf{w}^T\mathbf{x})\right\}\mathbf{I}, && \text{(V.24)} \end{aligned}$$

the Jacobian matrix becomes diagonal and can be inverted. Then, by applying Newton's method, Eq. V.20 yields

$$\begin{aligned} \mathbf{w}' &= \mathbf{w}^{-} - \mu \frac{\mathrm{E}\left\{\mathbf{x}\, g\left(\mathbf{w}^{-T}\mathbf{x}\right)\right\} - \beta \mathbf{w}^{-}}{\mathrm{E}\left\{g'\left(\mathbf{w}^{-T}\mathbf{x}\right)\right\} - \beta} && \text{(V.25)} \\ \mathbf{w}^{+} &= \frac{\mathbf{w}'}{||\mathbf{w}'||}, && \text{(V.26)} \end{aligned}$$

where μ is a step size parameter. In our study, the parameter μ was assigned the value of 0.005. As far as the number of ICs to be separated by fast ICA is concerned, it was found that a very suitable choice for this was given by the number of SQUID magnetometer channels, i.e. the number of signals acquired during each experiment. Within the theoretical framework of fast ICA, this choice does have a reasonable amount of merit [69] since most of the explained variances of the original signals are accounted for in this approach.

After computing the IC's of an MGG data set, the so-called labeling problem of PCA must be addressed. This problem can be defined as the "task of finding substantive interpretations of some set of hypothetical latent variables which have been derived" [69]. In the case at hand, this translates into the challenge of associating one of the computed IC's with the gastric signal, which constitutes in this case the latent variable of interest. For the present study, the labeling problem was addressed using a visual analysis of the IC's that sought to identify the particular IC whose waveform best matched the gastric ECA waveform, which has a distinct frequency of 3 cpm.

Results and discussion

The results of the fast ICA analysis of MGG data are shown in Figs. V.2-V.5. In Fig. V.2, the ICs isolated with our fast ICA algorithm are presented. These ICs are

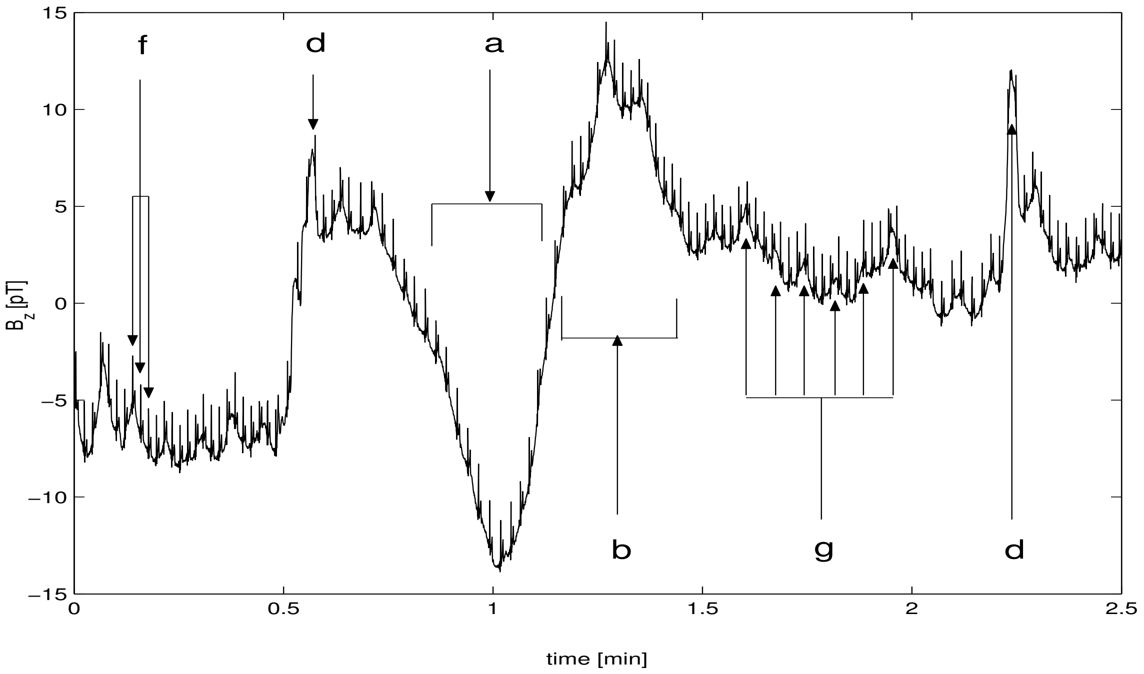

Figure V.3: Plot of the SQUID signal shown in red (i.e. the signal plotted in the second column and second row) in Fig. V.1. The contributors of each of the ICs separated by fast ICA in Fig. V.2 are pointed out by arrows. The labels for each arrow correspond to the ICs displayed in the associated subplot of Fig. V.2 that is labeled by the same letter. Thus, the features labeled by (a), (b), (d) are artifacts while those indicated by (f) and (g) are of cardiac and respiratory origin, respectively. The artifact shown in Fig. V.2 (c) is not readily apparent due to a cancellation effect between the waveforms due to artifacts (a), (b) and (d). In the cases of cardiac and respiratory activities, only a few selected artifact features are labeled by arrows due to the their large number in the featured plot. Because of these artifacts, the waveform of the signal does not allow one to visually identify the gastric IC of the signal. However, the fast ICA technique does allow one to do this quite well (see Fig.V.2 (e)).

arranged from (a) to (h) in the order of their contributions to the variances of the raw SQUID signals. The ones in Fig. V.2 (a)-(d) can be identified as motion artifacts caused by the movement of the human subject under the SQUID. These ICs have higher magnitudes than those in Fig. V.2 (e)-(h) and dominate in fact the waveforms of the raw SQUID signals shown in Fig. V.1. Because of these artifacts, the waveform of the gastric ECA signal is not distinguishable in the latter plots. Fig. V.2 (e) shows a sinusoidal waveform with a dominating frequency of approximately 3 cpm, corresponding to the gastric signal. The cardiac MCG signal was also isolated by the algorithm as a separate IC with a dominating frequency of about 75 cpm, as shown in Fig. V.2 (f). The respiratory artifact in the SQUID data is of smaller magnitude than both the gastric and the cardiac signals and has a dominating frequency of approximately 13 cpm (Fig. V.2 (g)). Finally, the fast ICA algorithm was also found to be capable of isolating a high-frequency IC that we believe to correspond to environmental and magnetometer noise (Fig. V.2 (h)), although further study is required for clarification. If fast ICA is indeed able to obtain a quantitative assessment of noise, the algorithm may be very suitable for measuring the signal-to-noise ratio of MGG experiments.

Some of the ICs in Fig. V.2 can be identified from the raw SQUID data in Fig. V.1; this is demonstrated in Fig. V.3. The most important conclusion that can be drawn from this figure is that, if artifacts due to motion, cardiac and respiratory activities are present, the gastric ECA waveform can be very difficult−if not impossible−to distinguish visually. This, together with the other results of our study, points out that the fast ICA algorithm is extremely suitable for the analysis of MGG signals.

Although sometimes difficult, the issues of (1) relating individual ICs to signals produced by actual biological sources and (2) determining realistic polarities and intensities for these signals from ICA information can be addressed in several ways. A common procedure is to retrieve field pattern information from the mixing vector $\mathbf{a}_i$ of the i-th IC [179]. A spatial mapping technique where mixing vector coefficients are associated with individual spatial locations on the horizontal grid of SQUID channel sensors can then be employed in many cases to determine the sources for which fast ICA has captured signal information in the ICs. In most cases of interest to our study (including those of gastric or cardiac signals), improved confidence regarding the realism of the IC extraction procedure is provided when ICs have both (1) waveforms that resemble those of biological signals originating in the organs of interest (stomach and heart, in our case) and (2) field patterns that are convincingly associated with the spatial locations of the organs where these biological signals are known to be generated based on *a priori* information. For example, a field pattern revealing the presence of a current dipole in the anatomic region of the gastric corpus and associated with a sinusoidal IC waveform that resembles the gastric ECA signal provides strong indication that the isolated IC corresponds to a signal generated in the stomach. It should be noted that the field patterns discussed here display mappings of dimensionless coefficients in the mixing vector $\mathbf{a}_i$ rather than actual magnetic field values. Thus, these visual tools depict the *pattern* of the field associated with a particular IC rather than its actual physical *values*.

An example that illustrates the method of analysis described above is presented in Fig. V.4. There, the field pattern due to the isolated gastric IC in Fig. V.2 (e) is displayed. Because the SQUID sensors of the Tristan 637i biomagnetometer are distributed horizontally, the pattern displayed is two- rather than three-dimensional as in the case of MEG, where field patterns are often used [179]. The field pattern in Fig. V.4 reveals the presence of a current dipole oriented in the direction of gastric ECA propagation; the location of the dipole under the measurement grid can be inferred based on a simple geometric argument [189] which shows that the dipole is located on the line segment that connects the points on the grid where the extrema of the field are located. The approximate orientation of the dipole can then be determined by applying the right hand rule of electrodynamics. The outline of the stomach is presented solely for illustrative purposes. Aside from being two- rather than three-dimensional, this type of field pattern is very similar to those used in MEG research [179]. What can be inferred from our figure is that the characteristics of the field pattern do satisfy the anatomic (i.e. dipole position) and physiologic (i.e. orientation along the propagation axis) conditions expected for a current dipole that approximates gastric ECA. In conclusion, the field pattern approach−coupled with the visual inspection method for analyzing IC waveforms−does seem to provide conclusive information that can allow us to identify the gastric IC with a reasonable amount of certainty.

This analysis would be incomplete if it did not offer a measure of fast ICA accuracy with respect to its ability to recover biological and non-biological signals satisfactorily. To demonstrate the algorithm's ability to extract these ICs faithfully, a comparison plot of fast ICA-reconstructed and electrode-measured respiration activity is presented in Fig. V.5. This figure shows excellent agreement between the reconstructed and the directly-measured waveform. The decision to choose this particular type of activity for validation is motivated by the practical ease associated with the noninvasive measurement of respiratory activity. As one may point out, our plot only offers an indirect measure of the accuracy associated with the ability of fast ICA to reconstruct the gastric IC with high accuracy. To obtain a direct measure of accuracy, an invasive method of validation (e.g. serosal electrode measurements of ECA) would also be required.

The ability of fast ICA to extract the gastric signal from MGG data can be made more obvious using a comparative analysis of this technique to a more traditional

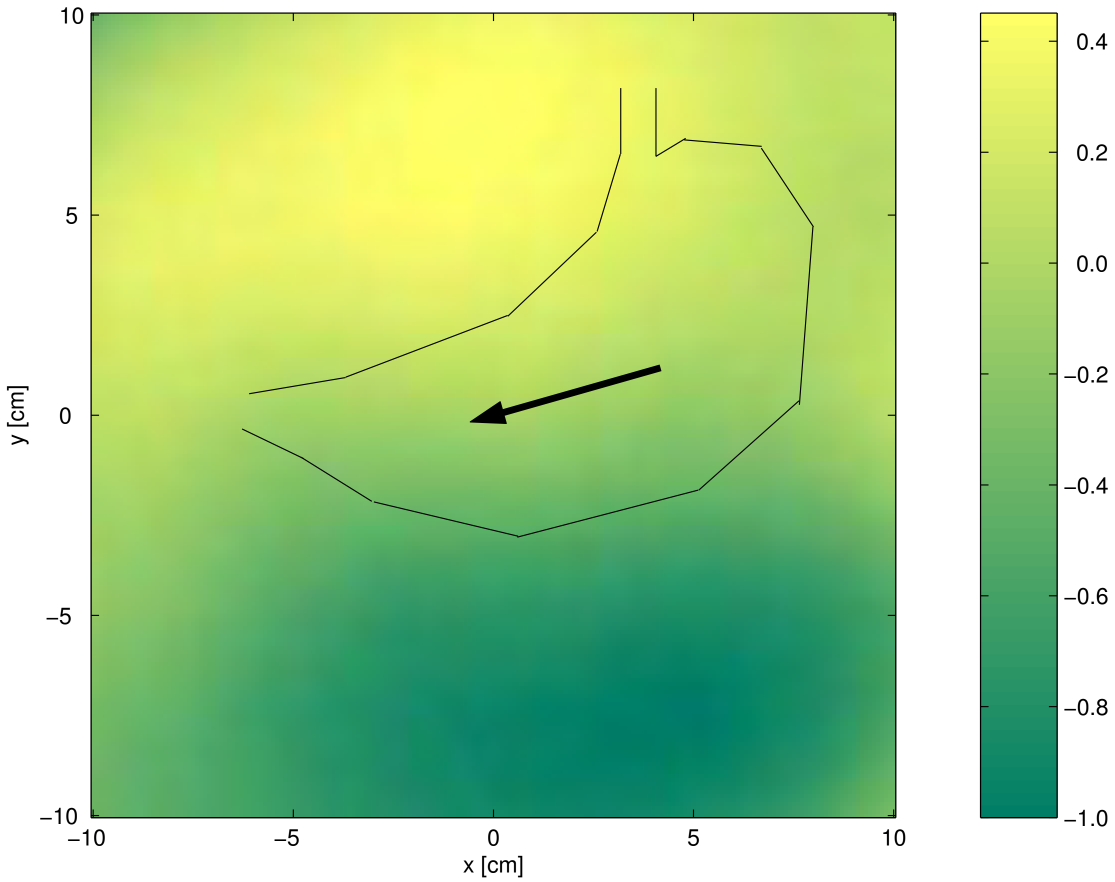

Figure V.4: Two dimensional field pattern associated with the gastric IC in Fig. V.2 (e). The map was generated by associating the coefficients of the mixing vector $\mathbf{a}_i$ for the gastric IC with the appropriate locations of corresponding SQUID channel sensors. To generate field values for the remaining nodes of the grid where no data had been recorded, two-dimensional biharmonic spline interpolation [153] was employed. The field pattern values displayed are dimensionless and are normalized for simplicity with respect to $|\max\{\mathbf{a}_i\}|$ (the largest absolute value among the coefficients in the mixing vector of the selected IC). The black arrow indicates the approximate location and projection onto the 2D plane of the gastric current dipole that generates the magnetic field being measured (the orientation of the dipole is determined using the right hand rule of magnetism). The approximate outline of the stomach is shown for orientation purposes only.

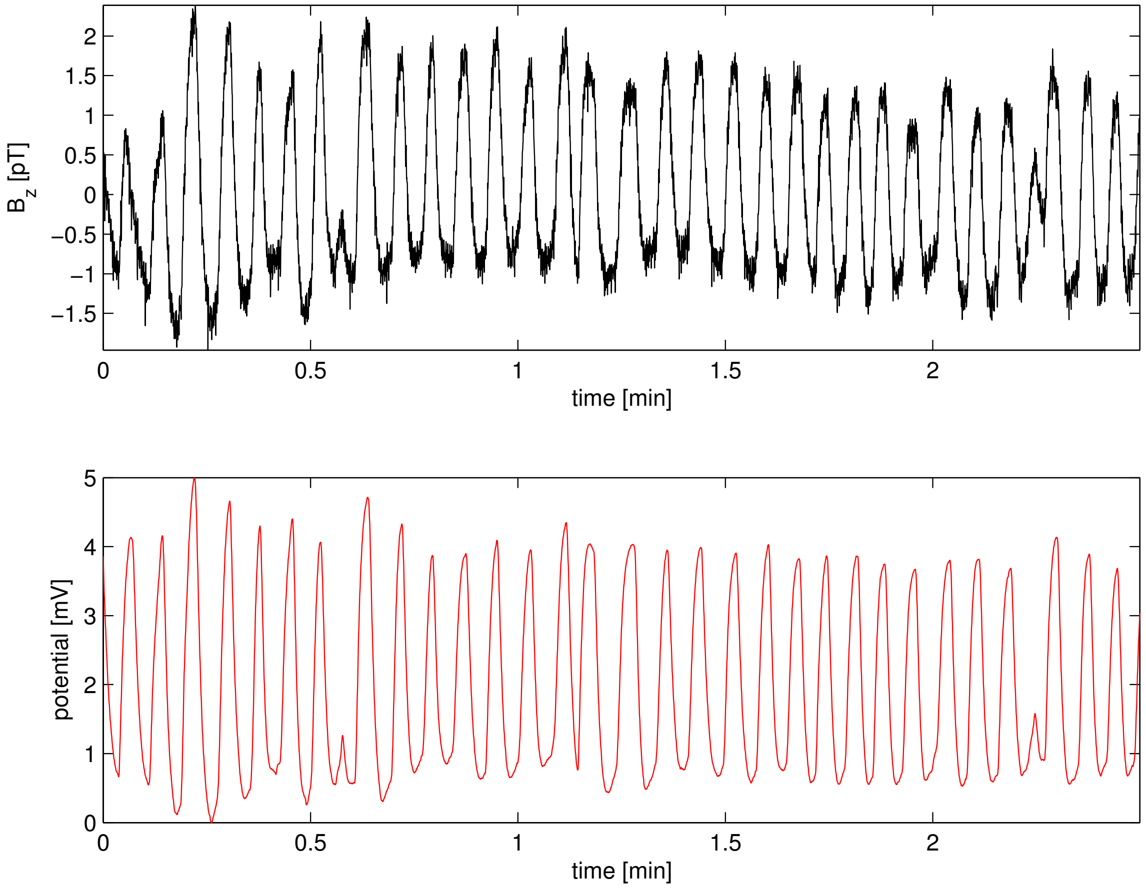

Figure V.5: Comparison plot of fast ICA-reconstructed (a) and directly-recorded (b) respiration activity. In (a), the plotted respiration signal is the same IC as the one presented in Fig.V.2 (g). This IC was reconstructed solely from the data. The signal shown in (b) was directly recorded from the human subject during the experiment using a nasal sensor that records variations in the temperature of the subject's breath. The two plots have different scales and units because the first one is an IC corresponding to a magnetic field component whereas the second one is an electric potential signal that was directly measured with an electrode system. Upon fitting the signal in (a) to the one in (b) in a least-squares sense, the value of the correlation coefficient r between the two quantities was found to be 0.957.

method such as digital filtering. A filter that has been widely used in MGG studies is the Butterworth filter [22, 24]. The second-order Butterworth filter that was applied for the purpose of our comparison is maximally flat in the pass band and monotonic overall, which reduces the effect of pass band ripples in the signal to a minimum. This type of filter sacrifices rolloff steepness for monotonicity in the pass- and stop-bands. To generate the filter, z-transform coefficients were created for a lowpass digital Butterworth filter with the user-specified cutoff frequencies of 1 and 20 cpm. The low cutoff of 1 cpm was selected in order to eliminate high frequency noise from the resulting waveform, while the upper cutoff of 20 cpm was chosen so as to take into account the high-frequency components of the gastric signal, whose dominant frequency is 3 cpm. Moreover, the selection of the value for the upper cutoff was motivated by the need to prevent the occurence of aliasing effects that can appear when filtering windows are too restrictive.

In Fig. V.6, two traces are presented, namely (1) the extracted gastric IC and (2) the waveform produced as a result of applying the Butterworth filter described above to the SQUID signal drawn in red in Fig. V.1 and reproduced in Fig. V.3. The fact that high-frequency signal components are present in the IC waveform as opposed to the filtered signal waveform is due to the fact that the application of fast ICA did not involve filtering in any way. One conclusion that can be drawn from Fig. V.6 is that, compared to the filtered signal, the waveform produced by fast ICA is more similar to the typical gastric ECA signal that has been recorded using both invasive and noninvasive procedures [17, 24]. Moreover, there is little similarity between the gastric IC and the filtered signal aside from their comparable magnitudes. The filtered SQUID signal contains a large number of spurious, short-lived oscillations that may be due to filtering artifacts; its waveform does not exhibit close similarity to the expected sinusoidal shape of the gastric ECA waveform. Nevertheless, any claim that

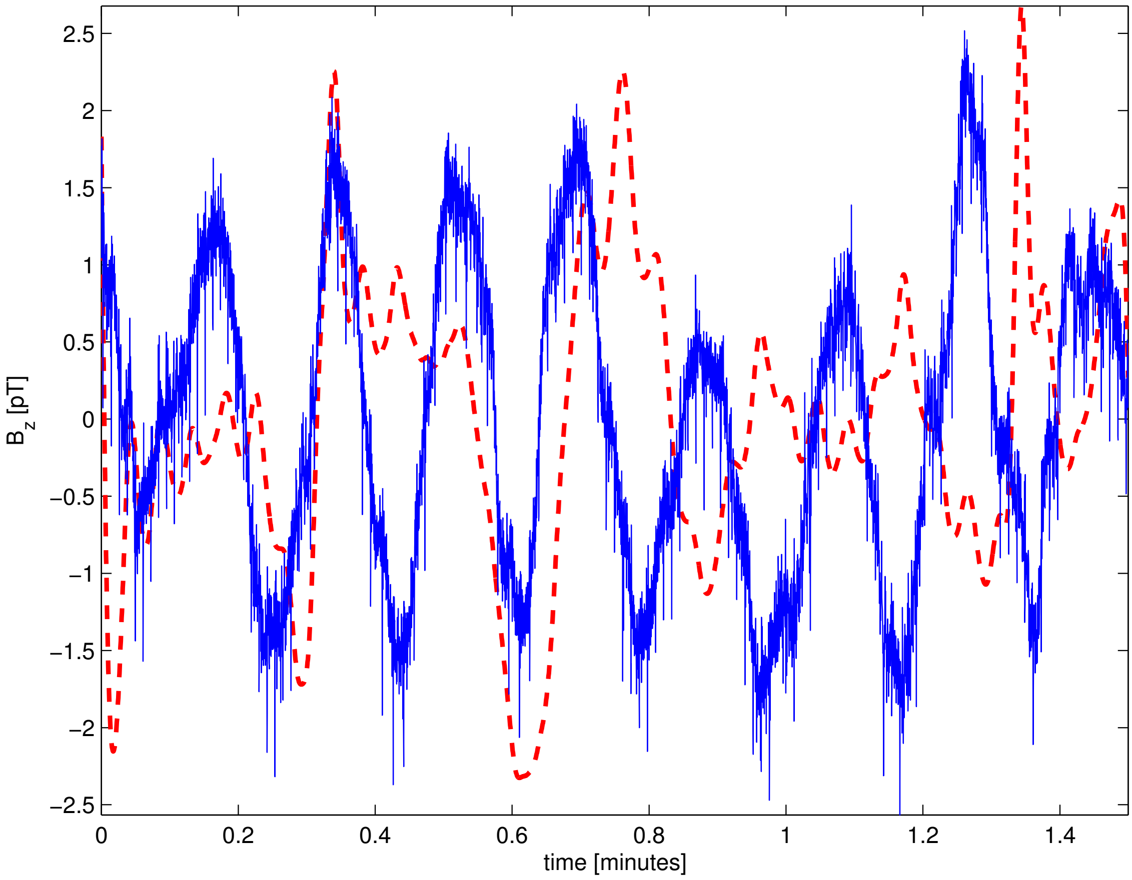

Figure V.6: Comparison between the gastric IC (blue, continuous) and the filtered SQUID signal in Fig. V.3 after the application of the Butterworth filter (red, dashed). Whereas the magnitude range of the two waveforms is comparable, there are significant differences between the abilities of the two methods to reproduce the expected sinusoidal waveform of the gastric ECA as the latter has been recorded using other procedures [17, 24].

ICA produces better waveforms has to be confirmed using simultaneous electrode and magnetic field recordings.

data set being analyzed. In our case, this was due to the fact that SQUID hardware resets can occur when noise levels inside the shielded room vary between two extremes within a short period of time. Because the Tristan 637i biomagnetometer is equipped with an automatic signal reset algorithm that is triggered whenever such noisy conditions occur, SQUID resets of the baseline signal can occur unexpectedly. When data are written to digital storage, such resets are recorded as sharp spikes whose order of magnitude is often many times larger than that of the biological signals that are being acquired. Thus, due to the presence of such high-magnitude reset spikes, the fast ICA algorithm was found to perform poorly unless the short time segment containing the reset spike was removed from the data processed using fast ICA. This poor performance was due, quite expectedly, to the fact that spikes were being identified as ICs which explained a large percentage of the signal variance but which had no association with the biological signals of interest. When, however, the removal of SQUID reset artifacts was implemented, the ability of the algorithm to extract the gastric signal was restored. Specifically, it was found that splitting the data before analysis into segments spanning 2-5 minutes of acquisition time that did not include reset artifacts was very useful in terms of allowing the fast ICA algorithm to extract the gastric component. It may also be possible that an alternative−albeit more computationally intensive−approach to the problem of SQUID resets can be implemented by selecting a larger number of PCs and ICs during fast ICA.

By applying the methods described in the previous sections to the human ten-subject data set, fast ICA was found to be able to identify the gastric and cardiac signals in all ten subjects. Comparisons between the extracted and the directly-measured respiration signals (as shown in Fig. V.5) were also performed for these volunteers, with resulting values for the cross-correlation coefficient r ranging between 0.87 and 0.98; the mean value of r across volunteers was found to be $r = 0.93 \pm 0.02$ S.E.M.

In conclusion, the use of fast ICA for the extraction of the gastric ECA signal from artifact-contaminated MGG data was demonstrated. The analysis was carried out using a fixed-point version of the fast ICA model with a stabilization constraint imposed for ill-conditioned MGG data. Although the algorithm was shown to extract the respiration activity signal accurately, invasive serosal electrode measurements may be required to directly clarify how powerful the method is for the reconstruction of the gastric ECA signal. Nevertheless, since it is quite probable that such invasive measurements would also be affected by motion artifacts, other types of validation may also be required in cases where such artifacts are also present. The visual analysis of field patterns associated with various ICs was found to be a useful tool in determining the sources of the isolated signals with reasonable certainty. Finally, more research is required to address the applicability of fast ICA for the characterization of pathological conditions.

CHAPTER VI

FILTERING VS. ICA FOR ARTIFACT REDUCTION

Introduction

As mentioned in previous chapters, three methods used for acquiring gastric ECA recordings are gastric electromyography (EMG), electrogastrography (EGG) and magnetogastrography (MGG). EMG and EGG involve the use of electrodes that record the bioelectric fields due to ECA. In the case of EMG, electrodes are positioned directly onto the serosa, which makes this technique strictly invasive. In the case of EGG, the electrodes are attached to the abdominal skin. Whereas the signal to noise ratio (SNR) of EMG is excellent, that of EGG is extremely poor. For this reason, the reliability of the latter technique has been questioned due to the high dependence of cutaneous electrical recordings upon tissue conductivity, the thickness of the abdominal wall, and the variable propagation velocity of ECA [103].

In the previous chapter, we demonstrated the use of ICA for the removal of both biological and non-biological artifacts from multi-channel MGG recordings. There, the accuracy of the method was analyzed by comparing ICA-extracted vs. electrode-measured respiratory signals to conclude that reliable results could be obtained with MGG in terms of ECA signal extraction. In what follows, we describe the use of ICA for signal extraction from simultaneous EMG/MGG recordings rather than from MGG recordings alone. Through the use of this improved technique, we demonstrate the accuracy of our method by comparing not respiratory signals as in the previous case, but rather the gastric signals themselves. Moreover, we show that ICA is superior to conventional filtering (CF) in its ability to remove artifacts from MGG recordings.

Methods

Two techniques were used for data acquisition, namely magnetogastrography (MGG) and electromyography (EMG). The electrode equipment employed for EMG data acquisition consisted of 18 pre-gelled, disposable, pickup/ground electrodes (Rochester Electro-Med Inc., Tampa, FL, USA) connected to an isolated bioelectric amplifier (James Long Co., Caroga Lake, NY, USA). Twelve electrodes were manually affixed to the skin of a fasted, anesthetized healthy pig of approximately 20 kg, which was placed horizontally under the SQUID inside the magnetically shielded room. Initial anaesthesia consisted of intravenous injections of Telazol, Ketamine and Xylazine, each at a concentration of 100 mg/ml. The dosage administered was 4.4 mg/kg Telazol, 2.2 mg/kg Ketamine and 2.2 mg/kg Xylazine. The animal was intubated and maintained on isoflurane anaesthesia with a concentration of 2%. A respiration sensor was placed on the mouth and nose. EMG data were acquired using a personal computer (Dell, Austin, TX, USA) through analog-to-digital conversion boards interfaced with custom LabVIEW software (PCI-6033E, National Instruments, Austin, TX, USA) with a sample frequency of 3 kHz and decimation to 300 Hz. Simultaneous EMG/MGG data were acquired for a duration of 15 minutes. To investigate and compare the ability of CF and ICA to remove respiration artifacts from the data, one-minute breathholds were induced twice throughout the recording.

Two data analysis methods were implemented separately for comparison, namely conventional filtering (CF) and ICA. The CF analysis performed consisted of the application of a bandpass, second-order Butterworth filter. As explained in the previous chapter, the Butterworth filter is maximally flat in the pass band and monotonic overall, which reduces the effect of passband ripples in the signal to a minimum.

Because our ICA implementation has already been described, its details are omitted. After computing the ICs, a set of 'ICA-reconstructed' signals were obtained as follows. First, the frequency spectrum was computed for each IC. Then, the energy content percentage, call it p, within the range of GI activity (1.5-15 cpm) was computed. In the next step, those rows in the matrix $\mathbf{W}$ that corresponded to ICs with $p \leq 0.15$ (15% or less GI frequency content) were set to zero. The new matrix, call it $\mathbf{Z}$, is thus similar to the matrix $\mathbf{W}$ described before, with the difference that $\mathbf{Z}$ does not contain information pertaining to ICs that contribute little to the GI content of the original signals $\mathbf{x}$. By performing the matrix operation $\mathbf{x}' = \mathbf{Z}^{-1}\hat{\mathbf{s}}$, one can obtain a new set of signals $\mathbf{x}'$, which are similar to the original recorded signals $\mathbf{x}$ but with the difference that no information is included that comes from ICs that have $p \leq 0.15$. In practice, such ICs contain cardiac, respiration, motion and other similar artifacts whose elimination is of course warranted. The signals $\mathbf{x}'$ are the set of 'ICA-reconstructed' signals, that is the set of recordings which contain only GI signal components and which are 'artifact-reduced'. These ICA-reconstructed signals are the ones based on which the comparison with CF is made in the following section. The motivation for using these reconstructed signals rather than the original ICs is the fact that a *comparison* of CF and ICA was attempted in this study. In our previous undertaking [91] it was of course demonstrated that gastric signals can be isolated using ICA, but no comparison of methods was attempted there. To compare ICA and CF fairly, however, it was necessary, for the purpose of the present study, to identify a manner of studying the results of the two methods in a similar data format. As a result, the method of ICA-reconstructed signals was used in order to focus on the abilities of the two methods to extract artifacts without introducing any bias in favor of ICA.

Results and discussion

Our first comparative analysis of waveforms obtained using CF and ICA is presented in Fig. VI.1. There, simultaneous EMG/MGG data are shown for one minute of recording time. Two different segments were chosen, namely one acquired during a breathhold (first column) and another acquired during respiration (second column).

In the case of raw data acquired during the breathhold (top left), no respiration artifact is visible, as expected. The most easily identifiable artifact in this case is of cardiac origin and has a frequency of about 80 cpm. This artifact is visible only in MGG data (shown using a continuous black trace) while the EMG raw signal (red dashed trace) is not affected by cardiac activity. The reason for this is the fact that EMG signals are generated primarily by sources in the immediate physical proximity of the sensor, while MGG signals can also be affected by sources that are farther away. Because electrode signals depend to a very large extent on tissue conductivity, electrical sources that are far from the recording site do not contribute to the signal appreciably. In the case of MGG, the quality and strength of the signal is dependent on tissue permeability, which is very nearly equal to that of free space for biological matter. This is why, although SQUID coils are farther from the source than electrodes are during a typical experiment (the latter being affixed directly to the external gastric surface), the MGG signal is more sensitive to cardiac activity than the EMG signal.

The raw data segment acquired during the breathhold (top left) can be compared to the raw data segment acquired during respiration (top right). In the latter, the respiration artifact is clearly visible in the case of MGG at a frequency of about 32 cpm. The cardiac artifact is also present, though its amplitude is lower. The EMG signal is not appreciably affected by respiration. This is because the relative electrode position with respect to the gastric electric source remains unchanged throughout

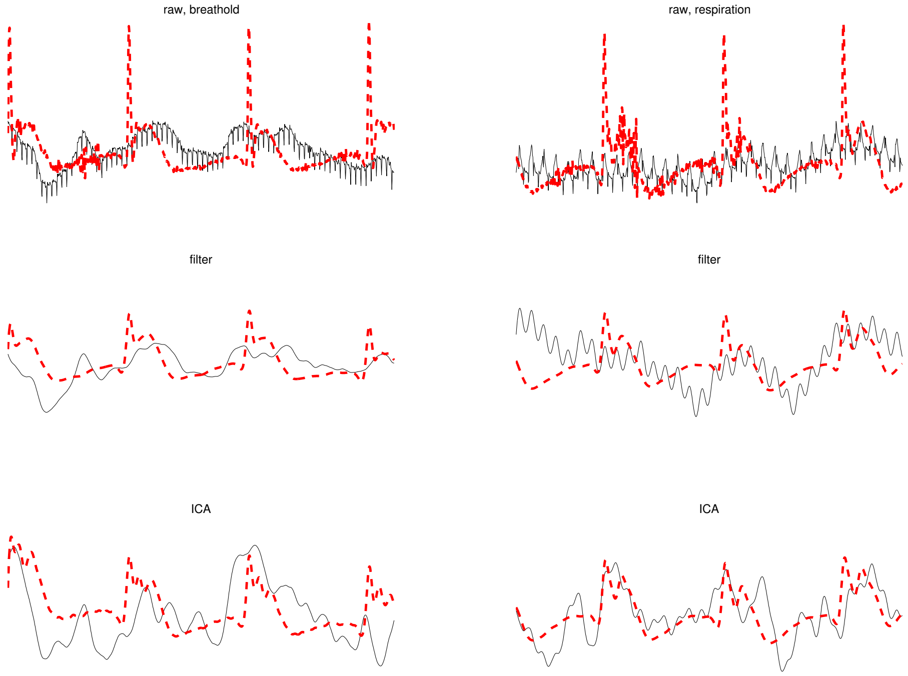

Figure VI.1: Validation across techniques of conventional filtering and ICA for artifact removal. MGG signals are shown as continuous (black) traces while EMG signals are shown as dashed (red) traces. The left column displays data acquired during a breathhold while the right column displays data acquired during respiration. The time interval shown is of one minute in both cases. The first row displays raw data, the second row displays filtered data and the third row displays ICA-processed data.

respiration, whereas for MGG this is not the case. As a result, EMG signal properties remain largely unchanged whether acquired during respiration or during a breathhold.

The second row in Fig. VI.1 displays the EMG and MGG signals after CF processing. In the case of EMG, results are very similar for breathhold and for respiration data. In the case of MGG, large differences exist. First of all, the CF method is not capable of removing the respiration artifact in a satisfactory manner, as shown in the plot on the middle right. Secondly, the EMG and MGG processed signals are more strongly correlated during the breathhold than they are during respiration.

The ICA results are shown in the third row of Fig. VI.1. There it can be seen that ICA is largely unaffected by the presence of respiration artifacts in the original data. Moreover, the correlation between the EMG and MGG waveforms is higher in both ICA cases as compared to CF-processed data.

In conclusion, Fig. VI.1 suggests that ICA may be superior to CF for simultaneous EMG/MGG recordings in at least two respects, namely (1) the agreement (amount of correlation) between the signals acquired using the two procedures and (2) the ability to minimize respiration artifacts from MGG data. This conclusion is supported by the contents of Fig. VI.2. This figure displays the same traces as in Fig. VI.1, though in a different manner that makes comparison easier from another perspective. Whereas Fig. VI.1 is useful to investigate the agreement between EMG and MGG (i.e. comparison of acquisition methods), Fig. VI.2 can be used to compare the artifact removal abilities of CF and ICA (i.e. comparison of signal processing methods).

In the top left section of Fig. VI.2, MGG raw data acquired during the breathhold (black continuous trace) is presented against the CF-processed signal (red dashed trace) and the ICA-processed signal (blue dotted trace). From this it can be seen that CF and ICA yield qualitatively similar results for data acquired during breathholds. In the top right section of the same figure, MGG raw data acquired during respiration

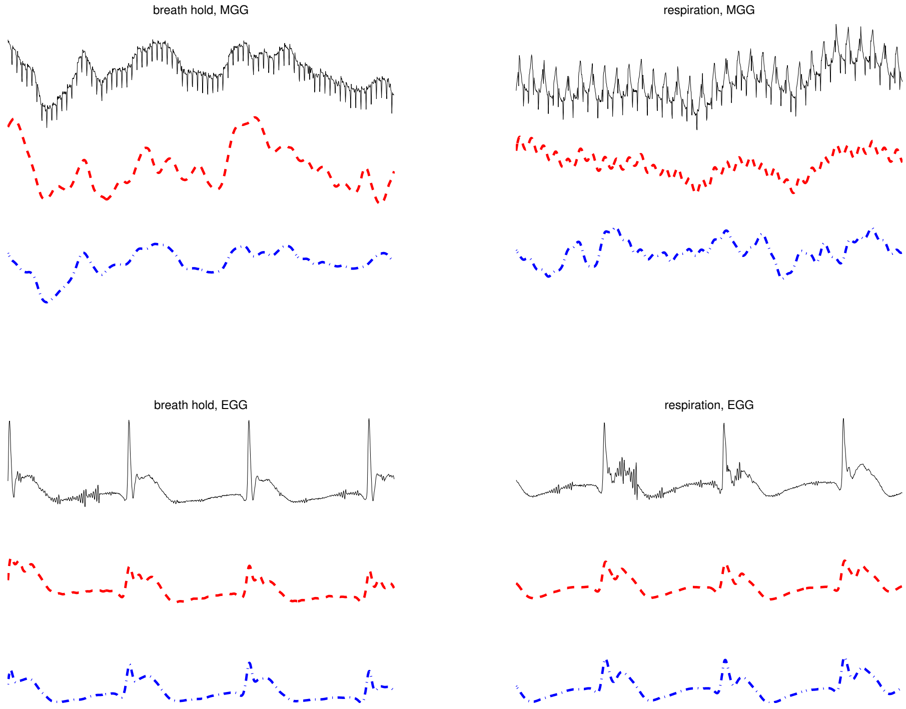

Figure VI.2: Comparison of conventional filtering and ICA for artifact removal in simultaneous EMG and MGG (II). Raw signals are shown as continuous (black, top) traces, filtered signals are shown as dashed (red, middle) traces and ICA-processed signals are shown as dot-dashed (blue, bottom) traces. The left column displays data acquired during a breathhold while the right column displays data acquired during respiration. The time interval shown is of one minute in both cases. The first column displays MGG data while the second column displays EMG data.

is compared to the CF and ICA signals using the same type of traces as in the previous example. In this case, however, it can be seen clearly that the respiration artifact is much larger in magnitude after CF than it is after ICA.

Finally, the bottom-row traces of Fig. VI.2 display EMG raw and processed data acquired during the breathhold (bottom left) and during respiration (bottom right). This comparison is largely unremarkable, as both CF and ICA are found to perform very similarly for EMG signals. However, as pointed above, the main differences between the two methods lie in their unequal abilities to process MGG data, which clearly separates them from the standpoint of their utility.

In addition to signal waveform comparison between CF and ICA, we have also undertaken a frequency analysis comparison of the two methods. The motivation for this is the fact that, as explained in the introduction, the frequency characteristics of EMG/MGG are important in distinguishing between healthy and diseased stomach. Because of this, it is important to understand how CF and ICA are different in their ability to capture the information contained in the frequency characteristics of EMG/MGG signals.

Fig. VI.3 displays an FFT frequency analysis of the same one-minute data segments presented in Fig. VI.1 and VI.2. The top left plot in Fig. VI.3 displays the frequency analysis of the raw data as acquired during respiration. Because the FFT method was used and the analyzed segment consisted of one minute of data acquired at 200 Hz, false peaks exist due to harmonics present at integer multiples of the dominant frequency. For example, in the case of EMG, a false peak is clearly visible at approximately 6 cpm, though the true peak at 3 cpm evident of gastric activity is clearly superior in magnitude.

The frequency analysis results for this segment after CF and ICA processing are shown in the same first column of Fig. VI.3 (middle left for CF and bottom left for ICA). Several conclusions can be drawn from inspecting these two plots. First, because of the filtering window used for CF and ICA before generating the FFT spectrum (1-30 cpm), the energy content due to low-frequency trends in the data is removed from the CF and ICA plots (middle and bottom left), as distinct from the original raw data (top left). Secondly, a comparison of the CF and ICA plots for the breathhold segment leads to the conclusion that, as far as breathhold data are concerned, the frequency content of the analyzed signal is qualitatively the same whether the latter is analyzed using CF or ICA.

The results of our frequency analysis for the respiration signal are presented in the second column of Fig. VI.3. Comparing the ICA plot (bottom right) to the raw data plot (top right) shows that ICA has the ability to preserve the frequency peak due to gastric activity at the same frequency as in the original raw data, i.e. at 3 cpm. On the other hand, comparing the CF plot (middle right) to the original raw data plot (top right) shows that the CF method is not able to do this. Instead, the gastric frequency peak appears to be shifted to a frequency lower than the true frequency as determined from the raw data plot. Moreover, a large amount of energy is found, for the CF plot, in the neighborhood of the peak at 8 cpm. This is misleading because it suggests that the dominant frequency of the signal is in that region, which is not true because the raw data frequency analysis plot suggests otherwise. In conclusion, while the CF and ICA methods yield comparable frequency analysis results for breathhold data, ICA seems to be superior when respiration data are analyzed.

Fig. VI.4 displays the frequency waterfall plots of the entire data sets from which the waveforms discussed up to this point were selected. For this figure, each spectrum displayed was created from a segment covering a period of 4 minutes, with an incremental step of 30 seconds for each successive spectrum. The first row displays CF-processed data and the second row displays ICA-processed data. Similarly, the

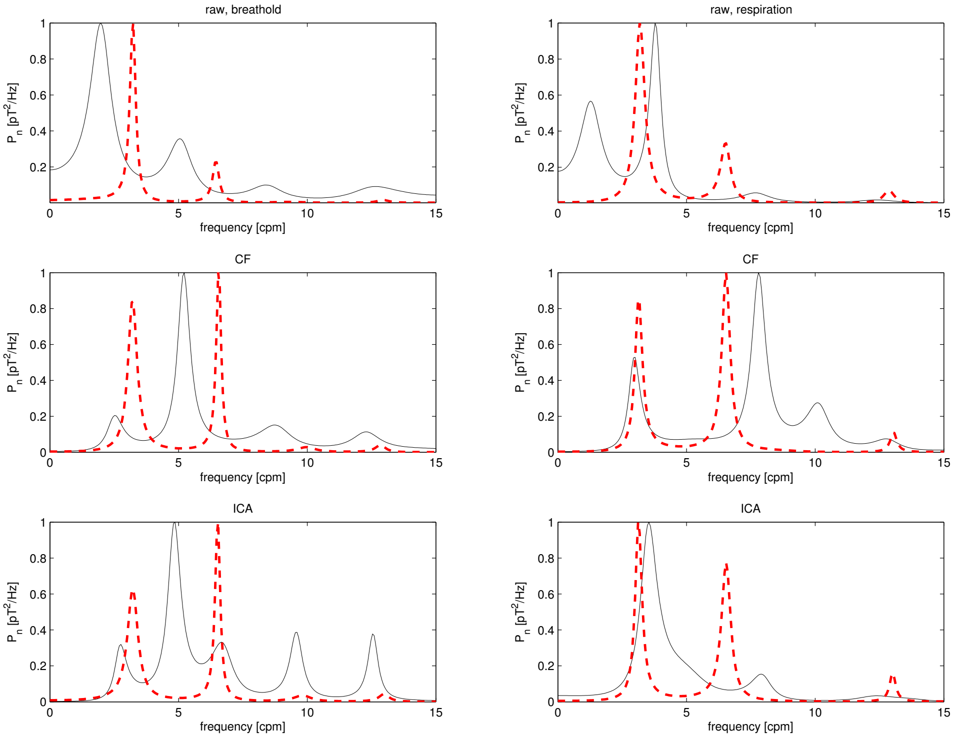

Figure VI.3: Frequency analysis results for the EMG/MGG data segments displayed in Figs. VI.1 and VI.2. MGG spectra are shown as continuous (black) traces while EMG spectra are shown as dashed (red) traces. The left column displays data acquired during a breathhold while the right column displays data acquired during respiration. The first row displays spectra for raw data, the second row displays spectra for filtered data and the third row displays spectra for ICA-processed data.

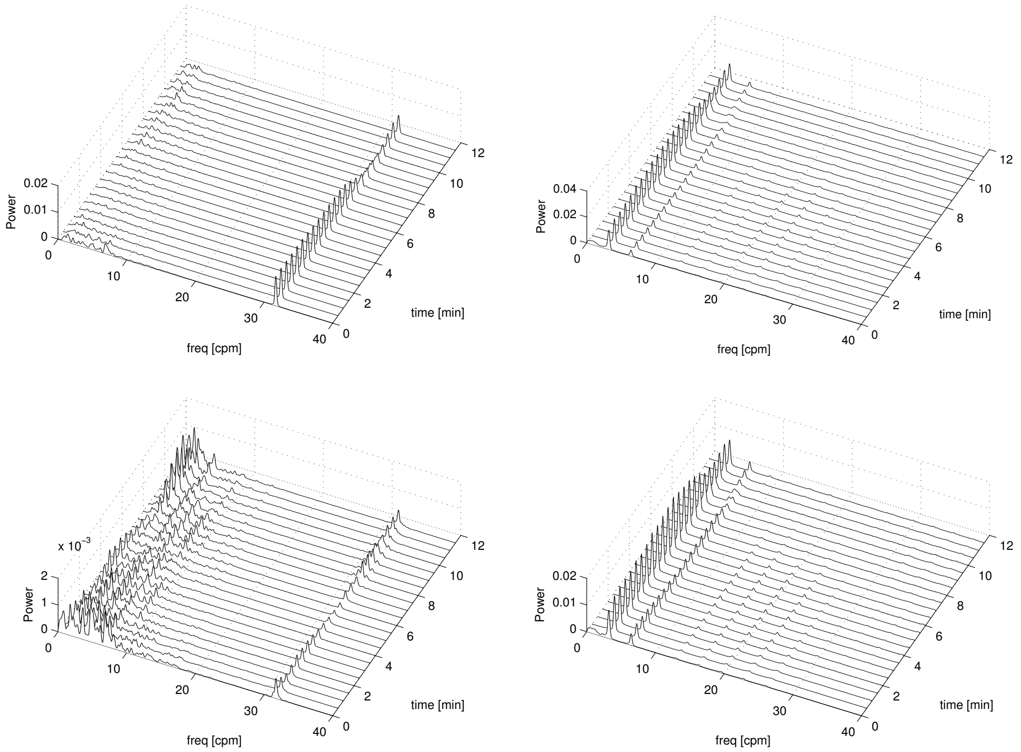

Figure VI.4: Comparison of waterfall plots for simultaneous EMG and MGG. The first columns displays MGG results and the second column displays EMG results. The first row refers to filtered data and the second row refers to ICA-processed data. The frequency range displayed is 0-40 cpm.

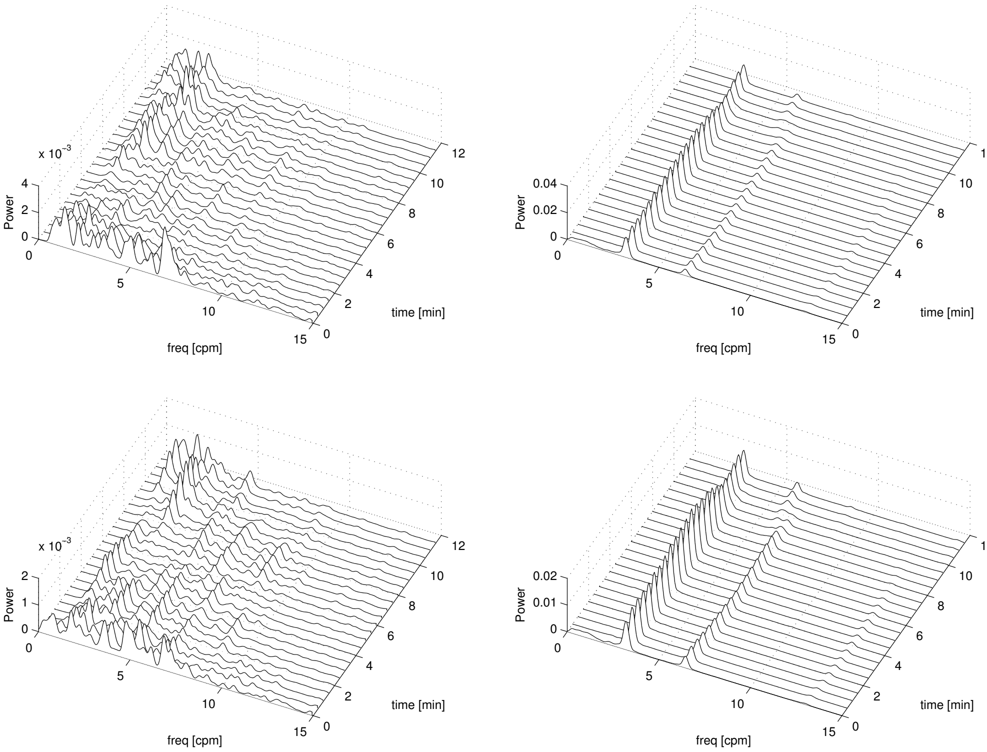

Figure VI.5: Same as Fig. VI.4, but with a frequency range displayed of 0-15 cpm.

first column displays MGG data while the second column displays EMG data. In the case of EMG, the results are very similar for CF and ICA. In the case of MGG, however, an important difference is that the height of the peak due to respiration (32 cpm) relative to the GI frequency content (1-10 cpm) is much higher for CF-processed data (top left) than it is for ICA-processed data (bottom left). This is true because, in the case of the CF waterfall plot, the respiration peak 'overshadows' the GI frequency content. In contrast to this, the ICA plot clearly demonstrates that the energy due to the respiration artifact is lower than that due to the GI content of the signal. This suggests that ICA is superior to the CF method from the standpoint of its ability to remove respiration artifacts from MGG data.

Fig. VI.5 displays the same information as Fig. VI.4 but the frequency range displayed is 0-15 cpm as opposed to 0-40 cpm in Fig. VI.4. Whereas the purpose of Fig. VI.4 was to emphasize the respiration artifact content of each signal, that of Fig. VI.5 is to focus on the GI content of each spectrum. The conclusion to be drawn is that the two methods are largely similar from a qualitative standpoint regarding their ability to capture the frequency information of the original signal. For both MGG and EMG plots, the temporal evolution of the frequency components is loosely the same in the CF as in the ICA case. Though differences exist, their nature is predominantly quantitative rather than qualitative. However, as Fig. VI.3 suggests, ICA can sometimes be more trustworthy than the CF method for the purpose of frequency analysis though the reverse may occur in some cases. Nevertheless, as Fig. VI.5 shows, the two methods are comparable from this standpoint and qualitatively very similar.

Several important conclusions were reached after our comparison of CF and ICA for the analysis of simultaneous EMG/MGG signals. First, it was determined that the two methods yield very similar results for breathhold data. Second, ICA was found to be superior to the CF method in the case of segments acquired during respiration. Because the large majority of our data sets consist of such segments, our study indicates that ICA may be preferable to the CF method for the analysis of EMG/MGG signals. Third, it was found that, qualitatively, the two methods yield comparable results regarding their ability to capture the frequency information of the signals. In conclusion, our study suggests that ICA is the more reliable and trustworthy technique for the purpose of artifact reduction in EMG/MGG.

CHAPTER VII

MEASUREMENT OF ECA PARAMETERS USING SPATIAL ICA

Introduction

The study of gastric motility is of clinical interest due to the relationship between gastrointestinal (GI) disorders and the characteristics of gastric electrical control activity (ECA). ECA is a slow, sinusoidal wave with a frequency of 3 cycles per minute (cpm) originating in the antral gastric region and propagated along smooth muscle cells. Abnormal ECA has been associated with many GI disorders, such as gastroparesis, diabetic gastropathy, and gastric myoelectrical dysrhythmia [140]. Two methods for characterizing ECA are electrogastrography (EGG) and magnetogastrography (MGG). EGG involves the placement of cutaneous electrodes on the abdomen to record the bioelectric fields due to ECA at the body surface. The reliability of this procedure has been questioned due to the high dependence of electrical recordings upon tissue conductivity, the thickness of the abdominal wall, and the variable propagation velocity of ECA [103]. MGG involves the positioning of a magnetometer in close proximity to the abdomen to detect the biomagnetic field generated by the electric current of ECA. The measurement of biomagnetic fields is advantageous because they are more strongly dependent on tissue permeability, which is nearly equivalent to that of free space.

In recent years, much attention has been devoted to the task of accurately measuring ECA spatiotemporal parameters such as its amplitude, direction and propagation velocity[176]. Clinically, it is important to understand the time behavior of these parameters because statistically significant differences in their average values have been found between subjects in the healthy and diseased states [29]. Thus, monitoring

ECA using a set of sensitive and reliable physiological parameters may one day provide a noninvasive method for detecting certain diseases whose diagnosis is otherwise problematic.

This chapter describes the application of PCA and ICA for measuring ECA parameters from simultaneous, noninvasive MGG/EGG recordings. The approach makes use of ICA to isolate the gastric signal, whereafter gastric dipole locations and orientations can be determined from ICA field maps. Results are compared, based on magnetic data, to analogous ones obtained using simultaneous electrode recordings.

Methods

MGG recordings were acquired using the SQUID biomagnetometer in the Vanderbilt University GIST Laboratory. The study was approved by the Vanderbilt University Institutional Review Board. Subject are asked to lie horizontally under the SQUID in the magnetically shielded room of the GIST Laboratory and the magnetometer is oriented so that the coils measuring the $\hat{\mathbf{x}}$ and $\hat{\mathbf{y}}$ components of the signal (tangential to the body surface) are oriented in the sagittal and horizontal planes, while the coils measuring the $\hat{\mathbf{z}}$ component (normal to the body surface) are oriented in the frontal plane. The electrode equipment employed for this experiment consisted of 18 pre-gelled, disposable, pick-up/ground electrodes (Rochester Electro-Med Inc., Tampa, FL, USA) connected to an isolated bioelectric amplifier (James Long Co., Caroga Lake, NY, USA). The electrodes were manually affixed to the skin in the configuration shown in Fig. VII.1. The relative spatial positioning between the MGG and EGG channels is also depicted in that figure.

The fast ICA method was separately implemented for each of the simultaneous MGG and EGG data sets to determine the independent components (ICs) derived

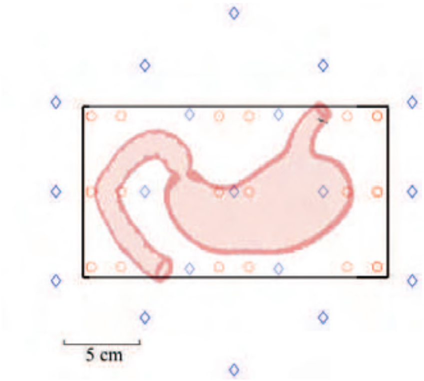

Figure VII.1: Data acquisition grid for simultaneous MGG/EGG experiments. Bipolar electrode channels are indicated by red circles and SQUID magnetometer channels by diamonds. The black rectangle enclosing the electrode channels indicates the extent of the area shown in the maps of Fig. VII.3. The outline of the stomach is approximate and is meant to serve as a guide to the eye.

from magnetic field and electric potential recordings, respectively. The labeling problem was addressed using an automated analysis of the ICs, whose purpose was to identify the IC whose waveform best matched the gastric ECA waveform (which has a distinct frequency of 3 cpm in humans). In most cases, the gastric IC was found to be among the first few ICs that accounted for the highest percentage of the variance in the recorded signals. We found this to be the case because the gastric signal is relatively strong compared to other components of biological origin and because it is superseded, in most cases, only by motion artifact signals.

Although there are advantages to performing a visual, offline analysis of ICs to determine the optimal ones to be used for analysis, an automated algorithm was developed instead. As an aid to the decision process, the power spectral density (PSD) of each IC (denoted henceforth by $\rho(f)$, where f is the frequency) was first computed using the classical fast Fourier transform, thus providing a time-frequency representation of MGG/EGG data. Both signal- and zero-padding were applied to reduce picket fence effects. In addition, appropriate Hamming windows were used. To investigate frequency changes in the gastric signal as a function of time, the recorded signals were split into segments denoted by $j = 1, \ldots, n$ and fast ICA was applied separately to each of them. Suppose that m ICs were computed for the i-th segment and let k represent the index of each IC, i.e. $k = 1, \ldots, m$ (it is assumed that the ICs are ordered in decreasing order of the variance in the data for which they account). If we let the symbol I represent some given IC, the notation I_{jk} denotes, in this convention, the k-th IC in data segment j. In the first step of our approach, we computed $\rho(I_{1k}; f)$, i.e. the PSD for each IC in the first time segment of the data set. To assess the similarity between the PSDs of different ICs (as described below), ρ values were normalized to $\tilde{\rho}$:

$$\tilde{\rho}(f) = \frac{\rho(f)}{\int_0^\infty \rho(f)\mathrm{d}f}, \qquad \text{(VII.1)}$$

where in practice the upper limit of integration is constrained by the Nyquist Theorem. Next, the energy integral

$$\mathcal{E}(\alpha, \beta) = \int_\alpha^\beta \tilde{\rho}(f)\mathrm{d}f \qquad \text{(VII.2)}$$

was calculated, where α and β are the cutoff frequencies for the signal of interest. In our case, the choice made was $[\alpha, \beta] = [2, 5]$ cpm, which is the frequency interval where most of the energy in the human gastric signal is contained. One can see that the quantity

$$\frac{\mathcal{E}(\alpha, \beta)}{\mathcal{E}(0, \infty)} = \frac{\int_\alpha^\beta \tilde{\rho}(f)\mathrm{d}f}{\int_0^\infty \tilde{\rho}(f)\mathrm{d}f} = \int_\alpha^\beta \tilde{\rho}(f)\mathrm{d}f \qquad \text{(VII.3)}$$

is maximized by the IC that has the largest proportion of energy in the interval $[\alpha, \beta]$. For this reason, the IC selected for analysis from the first segment of data ($i = 1$) was chosen based on this criterion. Let this IC be denoted by I_{1c} (c for 'chosen').

In the second stage of the selection algorithm, the subsequent time segments of data $j = 2, \ldots, n$ were processed. For each of these, the squared energy residuals

$$\Delta\mathcal{E}_{jk}^2 = \left[\int_0^\infty \tilde{\rho}(I_{1c}; f)\mathrm{d}f - \int_0^\infty \tilde{\rho}(I_{jk}; f)\mathrm{d}f\right]^2 \tag{VII.4}$$

were evaluated. What $\Delta\mathcal{E}_{jk}^2$ provides is a measure of the 'similarity' between the first chosen independent component (I_{1c}) and each of the components in the subsequent time segments (I_{jk}). Naturally, this measure is minimized when the similarity is highest. For this reason, the IC with the lowest value of the squared energy residual was selected for analysis. A legitimate question can be raised by the reader as to why different selection criteria were chosen for the two steps of our algorithm. The reason lies in the fact that fast ICA can very possibly separate more than one gastric component from the data. Naturally, since these components may account for distinct dipolar patterns with distinct locations and rhythms, it is important to distinguish between the IC that was chosen initially (I_{1c}) and other ICs. This is because, since one wishes to determine the spatiotemporal evolution of I_{1c}, it is more useful to identify ICs in subsequent data segments that are most similar to I_{1c} (and therefore most likely to represent the signal due to the source being sought) rather than other dipoles−whether gastric or not−whose evolution is not under focus. Thus, to identify $I_{2c}, \ldots, I_{nc}$, the use of the quantitative measure $\Delta\mathcal{E}_{jk}^2$ is preferable. After selecting suitable ICs for each time segment in the data set, the signals provided by the chosen ICs were analyzed. First, each data set was detrended using a linear fit to eliminate short-lived trends that are due to extraneous causes, such as low-frequency noise. Then, a number of bandpass, second-order Butterworth filters were applied.

The source model adopted for this study consists of a current dipole $\mathbf{Q}_1$ that approximates a current density $\mathbf{J}(\mathbf{r}')$ with spatial extent at $\mathbf{r}'$ in an ellongated cylinder with an inhomogeneous conductivity profile. Since the ECA is a depolarization/repolarization wavefront advancing along the corpus, the current dipole approximation is appropriate in our context. For our purposes, the inhomogeneity of the spatial conductivity function σ can be approximated through the use of small regions of piecewise homogeneous conductivity. The sources $\mathbf{Q}_i$ are assumed to be buried beneath the skin surface, which is taken to be the plane $z = 0$ cm. It is relatively straightforward [173] to show that, if the distance between the two extrema of $\mathbf{B}(\mathbf{Q}_i)$ on the surface is taken to be γ and the dipole is approximately parallel to the surface, then the dipole lies at a depth $z = -\gamma/\sqrt{2}$ on the vertical plane that passes through the extrema. the magnetic field $\mathbf{B}$ above the surface of the body can be approximated, in the context of the quasistatic approximation to Maxwell's equations [173], by

$$\mathbf{B}(\mathbf{r}) = \frac{\mu_0}{4\pi}\left[\int \mathbf{J}_i(\mathbf{r}')\mathrm{d}\mathbf{r}' - \sum_{\nu\eta}(\sigma_\nu - \sigma_\eta)V(\mathbf{r}')\mathrm{d}S_{\nu\eta}\right] \times \nabla' \frac{1}{||\mathbf{r}-\mathbf{r}'||}, \qquad \text{(VII.5)}$$

where V is the electric surface potential, $\mathbf{r}$ and $\mathbf{r}'$ are the field and source points, respectively, μ_0 is the permeability of the vacuum and $||\cdot||$ is the Euclidian norm. The summation is carried out over all the regions ν and η of the surface S that have different piecewise constant conductivities. For example, the quantity $(\sigma_\nu - \sigma_\eta)$ is the conductivity difference between two regions ν and η that are adjacent. We refer the reader to [173] for the derivation of this formula.

Similarly, the relationship for the electric potential analogous to (VII.5) is given by

$$V(\mathbf{r}) = \frac{1}{4\pi\sigma}\left\{\int [\mathbf{J}_i(\mathbf{r}_i)\mathrm{d}^3\mathbf{r}' - \sum_{\nu\eta}(\sigma_\nu - \sigma_\eta)V(\mathbf{r}')\mathrm{d}\mathbf{S}'_{\eta\nu}] \cdot \nabla' \frac{1}{||\mathbf{r}-\mathbf{r}'||}\right\}. \qquad \text{(VII.6)}$$

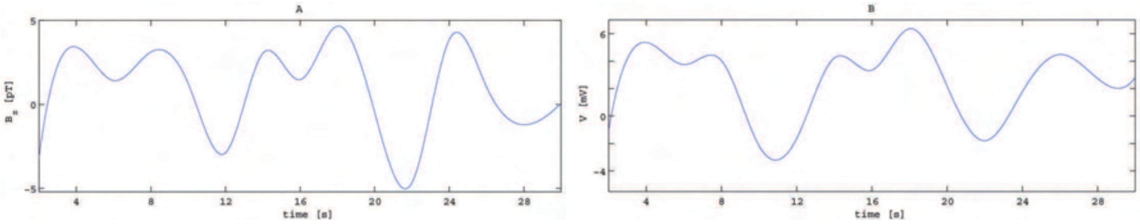

Figure VII.2: Sample ECA waveform as recorded using simultaneous MGG (A) and EGG (B). Signal extraction was performed using fast ICA and appropriate Butterworth filters and Hamming windows were applied to the selected ICs to generate these plots. Both waveforms display the characteristic gastric frequency of 3 cpm.

The process of identifying the location and orientation of bioelectric sources from information provided by ICA has already been successfully implemented in magnetoencephalography [45] and magnetocardiography [42]. Our particular approach closely follows the method proposed by Tang and colleagues [171]. Spatial information regarding a separated IC is provided by its sensor projection (field map), which represents the measured sensor response to the activation of the component $\hat{\mathbf{s}}_{jk}$. The information required to construct the map of component k in time segment j is contained in the k-th column of the estimated attenuation matrix $\hat{\mathbf{A}}$ for that particular IC, which we denote by $\hat{\mathbf{A}}_k$. The values in $\hat{\mathbf{A}}_k$ were used to create a two-dimensional field/potential map using adaptive cubic spline interpolation. This method was then employed to generate 2D spatial maps that show, in addition to the underlying field/potential maps, the locations of the current dipoles as inferred from the field/potential map data.

Results and discussion

Sample simultaneous MGG/EGG waveforms are shown in Fig. VII.2. In Fig. VII.3, examples of field/potential maps from three non-consecutive time points (A, B, C) are shown. The quantity visualized in each spatial map is the *normalized* amplitudes of the magnetic field ($\tilde{B}_i$) and electric potential ($\tilde{V}_i$) due to three identified gastric sources, where $\tilde{B}_i = B_i/\max\{B_i\}$ and $\tilde{V}_i = V_i/\max\{V_i\}$. Also depicted are the inferred locations of the associated current dipole producing the fields/potentials shown in the map. The decision to plot $\tilde{B}_i$ and $\tilde{V}_i$ rather than B_i and V was made so as to simplify the visual comparison of different maps. Because only one colorbar and colormap were used for *all* maps (although $\max\{B_i\}$ and $\max\{V_i\}$ are different for each map), plotting $\tilde{B}_i$ and $\tilde{V}_i$ ensured that the same proportional scaling was used for all maps. Thus, comparison between different maps is simplified.

All maps have a spatial extent of 17 × 10 cm. Because simultaneous MGG/EGG recordings were acquired, maps were computed from both magnetic field (B) and electric potential (V) signals. This procedure allowed for the comparison of noninvasive biomagnetic recordings to cutaneous electrode data. In Fig. VII.3, the orientations of MGG-based dipoles are more realistic and are similar, in fact, to those obtained from MGG data in a previous study using the surface current density method [26].

One important observation to be made from the analysis of our figure is that, due to its higher spatial resolution, the magnetic sensor grid is superior to the electrode grid from the standpoint of its ability to capture the configuration of the gastric biomagnetic field. In spite of grid coarseness issues, electric maps are nevertheless valuable because they offer a method of comparison between the dipole locations and orientations obtained using the two protocols. Quite possibly, differences in location and orientation between MGG- and EGG-based dipoles are due to the different signal-to-noise ratios of the two procedures as well as to the difference in the finesse and configurations of the two grids. In conclusion, there is agreement between the two although magnetic recordings are superior in their ability to portray the underlying physiology.

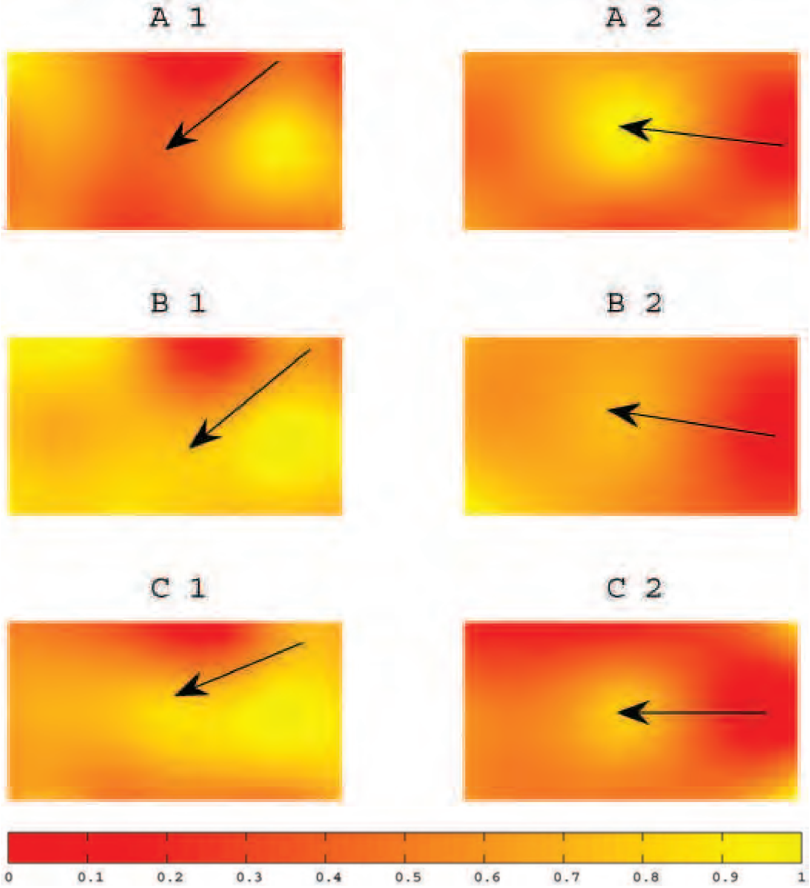

Figure VII.3: Examples of field/potential maps from three non-consecutive time points (A, B, C). Maps of magnetic field (B_z, see A1, B1, C1) and electric potential (V, see A2, B2, C2) patterns were extracted from simultaneous MGG/EGG recordings using fast ICA. Pictured are spatial maps of *normalized* (see text) B and V values as inferred via fast ICA (the first column depicts $\tilde{B}_i$, the second column depicts $\tilde{V}$). Grid dimensions are 17 × 10 cm. Black arrows are shown as guides to the eye to indicate the locations and orientations of the underlying current dipoles as inferred from the spatial maps using the right hand rule.

Black arrows visually track the spatial displacement of this dipole throughout the ECA cycle, allowing us to compute the average propagation velocity of electrical activity. The six black arrows in the last 6 frames (3 seconds) indicate the emergence of a second current dipole in the anatomic region of the gastric corpus. This phenomenon is associated with the reset of ECA to the gastric syncytium and with the beginning of another propagation cycle.

In conclusion, the comparison of magnetic field and electric potential maps obtained from simultaneous MGG/EGG recordings is important due to the uncertainties associated with the spatial accuracy of such methods. An interesting next step would involve subjecting our ICA-computed data components to three-dimensional inverse algorithms, which may allow us to determine ECA parameters not only for the stomach but also for the intestine.

CHAPTER VIII

NONLINEAR DYNAMICS OF THE GI SYSTEM

Introduction

The study of nonlinear dynamics is important for the elucidation of complex pathological states such as arrhythmia, ischemia and muscle injury [60, 95]. Since the first magnetocardiography (MCG) experiments of the late 1960s and early 1970s [35, 36], significant progress has been made towards the use of chaos theory for the characterization of normal and abnormal states of the mammalian heart. Differences between chaos patterns in the healthy and pathological states have been revealed in the context of cardiac fibrillation, heart rate variability and chronic heart failure [57, 110, 15, 168, 27]. In neuroscience, nonlinear analysis techniques have been useful for the study of various phenomena of the brain, including epilepsy, cerebral hemisphere synchronization, depression and schizophrenia [11, 166, 141].

Recent literature describes the use of chaos analysis for the study of many other biological systems such as muscular structures, biliary ducts and renal calyces [60]. Nevertheless, very little research has been conducted regarding the content and characteristics of chaos patterns in the gastrointestinal (GI) system [68, 132, 118], where their clinical significance is nevertheless comparable. Moreover, little progress has been made towards revealing the connection between abnormal states of the circulatory system and circulation-related GI pathology.

Much is now known regarding the electrical activity of the heart [63]. Cardiac fibers are made of individual cells connected in series and in parallel with one another and the cardiac action potential is caused by the opening of fast sodium and slow calcium channels. While the slow calcium channels are open, a large quantity of calcium and sodium ions flow to the interior of the cardiac muscle fiber. This maintains a prolonged period of depolarization, which is the cause of the plateau phase of the action potential. Cardiac rhythmicity is controlled by the sinus node, which acts as a pacemaker of the normal heart. Cardiac arrhythmias can be caused by a variety of conditions, including abnormal rhythmicity of the pacemaker, shift of the pacemaker from the sinus node to other locations, abnormalities in the spread of the impulse through the heart, etc. In the case of the stomach and intestine, two major phenomena of the GI tract−the electrical control and response activities (ECA and ERA, respectively)−are responsible for the measurable electric potentials and magnetic fields recorded via magneto -gastrography and -enterography. ECA originates in the gastric antrum due to the presence of the interstitial cells of Cajal, which impose periodic waves of cell membrane depolarization and repolarization that advance along the corpus of the stomach at a rate of 3-6 cycles per minute (cpm) in porcines. Each of these waves consists of a potential upstroke followed by a plateau and then by a sustained depolarization phase. Gastric smooth muscle cells respond to this cycle by regulating L-type Ca^{2+} currents that are responsible for the contractile behavior of the stomach. Associated with this contractile behavior is gastric ERA, which is characterized by spiking potentials during the plateau phase of ECA. The electrical activity initiated in the stomach propagates along the entire length of the GI tract, although propagation frequencies depend upon position along the tract and mammalian species. Previously, chaos in the GI system has been explored within the framework of the FitzHugh-Nagumo equations [3, 4]. From a theoretical perspective, GI electrical activity can be modeled using a system of bidirectionally coupled relaxation oscillators where ERA interestingly represents a bifurcation solution to the set of partial differential equations governing the system [154, 155, 156].

One tool of particular importance in nonlinear dynamical analysis is the Lorentz attractor. This 3D object can be formally defined as the subspace of the total state space of a system to which the trajectory of the system converges after the initial transients have died out [166]. The term ‘attractor’ originates from the fact that such an object attracts towards it trajectories from all possible initial conditions. A linear dissipative deterministic system has an attractor that consists of a single point (hence the term ‘point attractor’) because such a system converges to a steady state after which no further changes occur unless external disturbances are present. In a chaotic system, however, the attractor can be very complex and usually assumes a fractal geometry. The dynamics corresponding to such an object is called deterministic chaos, which means that the system is deterministic only in the short term although system trajectories are confined to the attractor.

Attractor analysis typically involves one or several quantitative measures. Among the wide variety of such measures that can be used to describe attractor dynamics, three common ones−capacity dimension, information dimension and correlation integral−were selected for our study. A 3D attractor can be divided using a partition of boxes of edge length ϵ. If $N(\epsilon)$ is the minimum number of boxes required to cover the spatial extent of the attractor, the capacity dimension of the system (also commonly referred to as Kolmogorov entropy or box-counting dimension) can be defined as

$$C = \lim_{\epsilon \to 0} \frac{\ln N(\epsilon)}{\ln(1/\epsilon)}. \tag{VIII.1}$$

The capacity dimension of a system is a measure of the ‘spatial extent’ of an attractor. In a practical sense, the capacity dimension is a measure of how tightly packed the sheets of the attractor are. The second measure that was used is the information dimension δ, first introduced by Balatoni & Rényi [13], which is a generalization of the capacity dimension concept that weighs each non-empty cube i by its probability

p_i:

$$\delta = \lim_{\epsilon \to 0} \frac{1}{\ln \epsilon} \sum_{i=1}^{N(\epsilon)} p_i \ln(1/p_i). \tag{VIII.2}$$

This measure can be thought of as the number of information bits required to specify a certain point to a certain degree of accuracy specified by ϵ. Another popular measure is the correlation dimension

$$\nu = \lim_{\epsilon \to 0} \frac{\ln \mathcal{I}}{\ln \epsilon}, \tag{VIII.3}$$

where $\mathcal{I}(\epsilon)$ is the correlation integral

$$\mathcal{I}(\epsilon) = \lim_{N \to \infty} \frac{1}{N(N-1)} \sum_{i=1}^{N} \sum_{j=1}^{N} \Theta(\epsilon - |\mathbf{r}_i - \mathbf{r}_j|), \tag{VIII.4}$$

Above, $\Theta(x)$ is the Heaviside function (-1 if $x \geq 0$, 0 otherwise) and $|\mathbf{r}_i - \mathbf{r}_j|$ is the distance between two points $\mathbf{r}_i$ and $\mathbf{r}_j$.

Similar to Lorentz attractors are return maps, which are 2D phase space plots [49]. A 3D phase space attractor is a visualization technique that allows one to study the time evolution of a system's return map. In this approach, the outline (perimeter) of the map is first determined based on a time segment of data of appropriate length. The process is then repeated for the entire length of the data set, which results in the creation of m return map outlines. If y and z are the two dimensions of the map, time can be plotted on the x dimension of a 3D plot and each section can be drawn on the $y - z$ plane at a constant value of x specified by the time span of the data segment from which the return map was generated. A 3D surface can then be drawn that connects the outlines of adjacent sections; this creates a 3D, spatiotemporal phase space attractor, which demonstrates the evolution of the chaos content in the signal throughout time. In our approach, an active shape contour (commonly known as 'snake' in image processing literature) based on a gradient vector force (GVF) algorithm [8] was employed to automatically determine the perimeter of each return map.

In the remainder of this chapter, the time evolution of normal and arrythmic cardiac and gastric biomagnetic signals is compared using simultaneous MCG and MGG. Normality and pathology in the two organs is then studied using various measures, both visual (Lorentz attractors, 2D return maps) and quantitative (capacity dimension, correlation integral, etc). It is proposed that a shared feature of circulation-related arrhythmias in mammals is that their onset and development are associated with statistically significant fluctuations in chaotic attractor dimensionality. Evidence in favor of this hypothesis is presented in the context of an animal model and validated using statistical testing procedures.

Experimental protocol and data analysis

The present study is focused on three mammalian organs–the heart, stomach and small intestine–in the attempt to capture those nonlinear dynamical properties of the three systems that are common. Our study made use of both MCG and MGG. The use of MGG is arguably more advantageous than that of electrogastrography (EGG) because the quality and strength of recorded EGG signals are strongly dependent upon the permittivity of tissues, whereas MGG depends primarily on their permeability, which is approximately equal to that of free space. EGG signals are thus attenuated by the layers of fat and skin located between internal organs and the recording electrodes, while MGG does not suffer from this setback [118].

Signals were acquired using the multichannel 637i SQUID biomagnetometer (Tristan Technologies Inc., San Diego, CA, USA) in the Vanderbilt University Gastrointestinal SQUID Technology (VU-GIST) Laboratory. The animal subject set consisted of 10 healthy domestic pigs (*sus domesticus*) of approximately 20 kg each. Each anesthetized animal was placed horizontally under the SQUID inside the magnetically shielded room. The protocol for the study was approved by the Vanderbilt University Institutional Animal Care and Use Committee (VU-IACUC). Initial anaesthesia consisted of intravenous injections of Telazol, Ketamine and Xylazine, each at a concentration of 100 mg/ml. The dosage administered was 4.4 mg/kg Telazol, 2.2 mg/kg Ketamine and 2.2 mg/kg Xylazine. Each animal was intubated and maintained on isoflurane anaesthesia with a concentration of 1.5-2.5%. Because the extent of the SQUID input grid is comparable to the size of the animal's chest and abdomen, simultaneous MCG/MGG signals could be recorded.

The set of pigs was divided into two and one of two important pathological GI conditions was induced in each group. In 10 of the 20 pigs used, the stomach was surgically divided and post-division data were acquired. In the other 10 pigs, intestinal ischemia was surgically induced by ligating the mesenteric artery of each animal and post-ligation data were then recorded. Thus, exactly one abnormal condition of the gut—gastric electrical source uncoupling in the first case and mesenteric ischemia in the second case—was induced. After one hour of post-surgery recording time, euthanasia was induced in pigs using an intravenous injection as data were being acquired. All animals were under monitored anaesthesia while euthanasia was being induced. The euthanasia solution consisted of pentobarbital sodium with a concentration of 390 mg/ml and a dosage of 860 mg/kg (1 cc/10 lb). This procedure allowed us to record not only the abnormal gastric and intestinal signals of each pig resulting from stomach division or ischemia induction, but also the increasingly arrhythmic cardiac signals induced by the euthanasia injection and culminating in cardiac arrest. The signals from these three organs were recorded simultaneously.

A common problem in nonlinear analysis is that there is usually not a one-to-one correspondance between the number of measured signals and the number of underlying sources. More often, the recorded signals are due to an unknown mixing of the true system variables [166]. This important issue was addressed in our case with a technique called embedding, where one or more simultaneous time series are converted to a series of vectors in an m-dimensional space, where m is often (as in our case) equal to 3 for convenience in view of three-dimensional (3D) visualization. In our case, the simultaneous time series are MCG/MGG signals. If certain conditions are satisfied [166], the so-called 'equivalent attractor' of the embedded system has the same dynamical properties as the true attractor. This fundamental statement of nonlinear analysis theory is known as Takens' embedding theorem [169]. In addition to embedding, another signal processing technique that is very suitable to this problem was employed, namely fast ICA.

To investigate the chaotic content of our recordings, three visualization methods were employed, namely the Lorentz attractor, return map and 3D spatiotemporal phase space attractor. First, fast ICA was used to recover the cardiac and gastric sources of interest from the SQUID-recorded mixtures. In doing so, the dimensionality of each data set was first reduced using PCA, whereafter fast ICA was applied.

Lorentz attractors were used to visualize MCG/MGG data. Differences in attractor characteristics between the healthy and pathological states were quantified numerically using four measures already described, namely the capacity dimension, information dimension, correlation dimension and correlation integral.

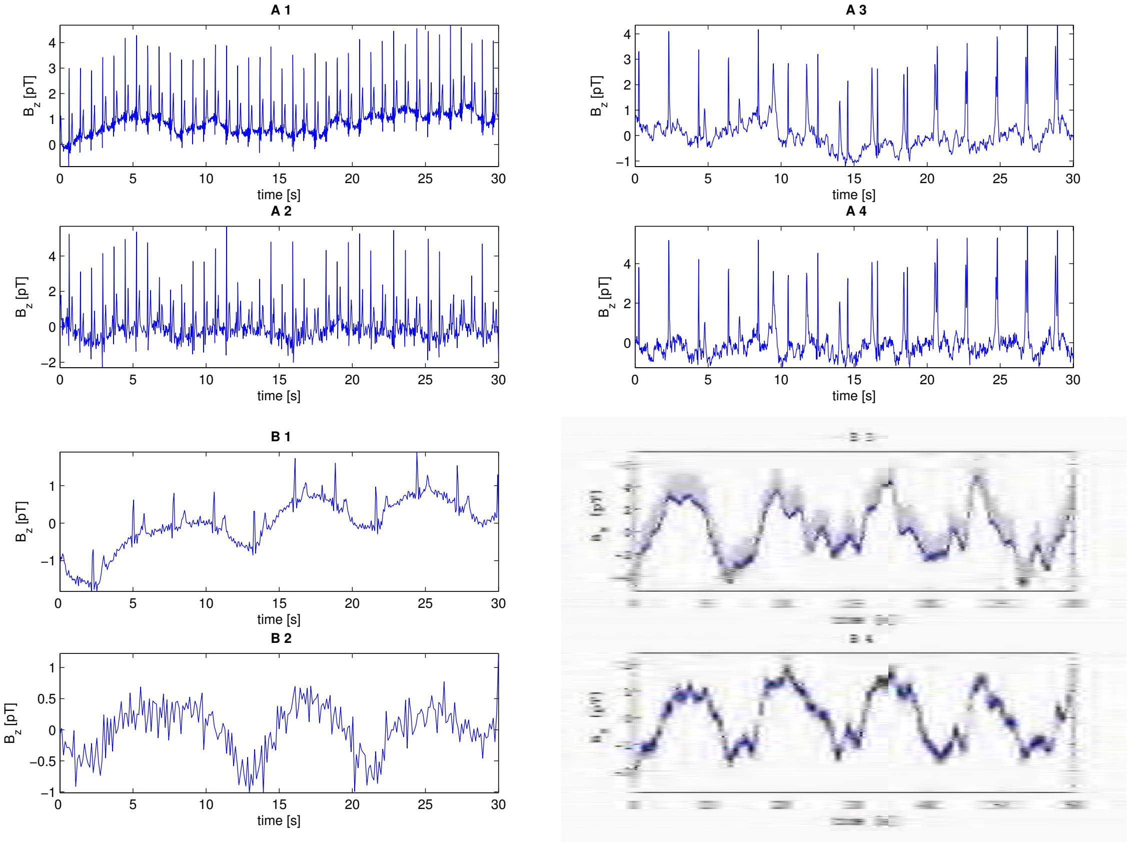

Figure VIII.1: Sample normal and pathological magnetic signals for the heart (A1-A4) and stomach (B1-B4) acquired from a porcine subject. The first column contains normal signals while the second one displays pathological signals. A1 and B1 show *normal* raw magnetic field (B_z) data, while A2 and B2 show FICA-processed, artifact-reduced signals. Similarly, A3 and B3 display *pathological* raw magnetic field (B_z) signals, while A4 and B4 show FICA-processed, artifact-reduced pathological data.

Results and discussion

Sample raw and ICA-processed MCG and MGG signals acquired from a porcine subject are shown in Figure VIII.1. What can be concluded from the analysis of this figure is that the underlying properties of the two biological sources are more readily apparent from their respective ICs (A2, A4, B2, B4) than from the raw data traces (A1, A3, B1, B3). Although cardiac interference (A1) is a significant artifact in the gastric signals of (B1), its presence was reduced via fast ICA. In A3 and A4, arrhythmic heart signals are shown while B3 and B4 display a tachygastric signal induced by stomach division. The differences between the normal and pathological signals of the heart are readily visible from our figure. Whereas the periodicity of the PQRST complex in the first case is normal ((A1) and (A2)), pronounced bradycardia is visible in (A3) and (A4). In the case of the gastric signals, the dominant GEA frequency is of approximately 3 cpm in (B1) and (B2), whereas (B3) and (B4) show a tachygastric rhythm of approximately 4.5 cpm.

Examples of Lorentz attractors created from our data are shown in Figure VIII.2. The normal cardiac attractor (A1) has a characteristic shape due to the high rhythmic pattern of the heart signal. This feature is disrupted in the arrhythmic state, which is also reflected in the attractor (A2), which has a more irregular shape. Comparing normal (B1) and abnormal (B2) gastric signals, one can see that a larger amount of chaos is present in the abnormal case (B2) compared to (B1).

Sample return maps generated from our analysis are presented in Fig. VIII.3, where both healthy and pathological data are shown for the heart, stomach and intestine. A dashed line is included for each plot to emphasize the symmetry of the return map. The increased asymetry of the pathological attractor (A2) with respect to the diagonal axis compared to the normal attractor (A1) is visually apparent. The ribbon in the top right corner of (A1)−corresponding to the cardiac R wave (ventricular depolarization)−includes more points than the corresponding ribbon in (A2). There, the number of points in this particular feature of the attractor is lower due to the bradyarrhythmic character of the cardiac signal. Because bradyarrhythmia is a state where the frequency of cardiac activity is lower than normal, fewer points in the attractor are due to the standard PQRST complex. Thus, the number of attractor points generated by this complex is considerably lower in (A2) compared

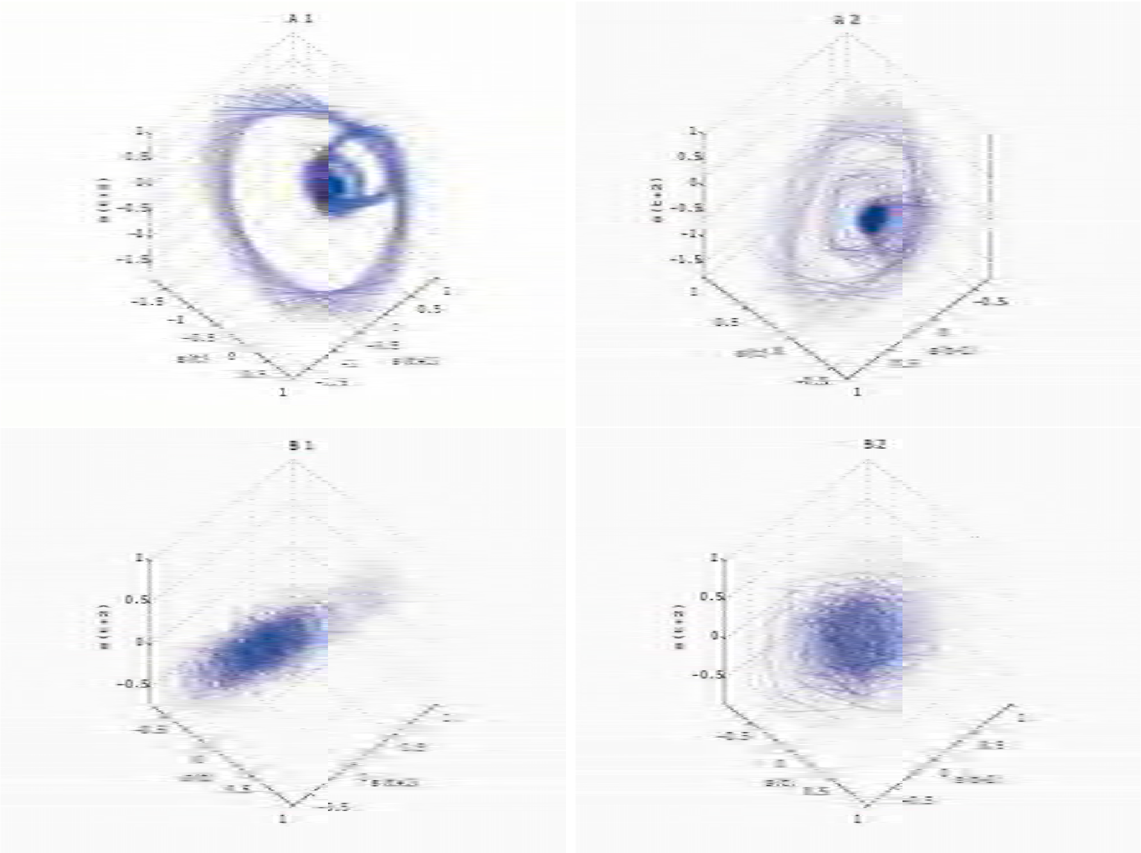

Figure VIII.2: Example of Lorenz attractors for heart (A) and stomach (B) signals. Both normal (1) and pathological (2) data were used and normalization was applied as in the previous figure.

to (A1). However, (A1) and (A2) contain an equal number of points, meaning that more points in (A2) are due to the resting state of the heart. In the case of the stomach (B1-B2) and intestine (C1-C2), return maps based on pathological signals have different shapes and exhibit visible clusters of points in the lower left-hand corner of each map.

A sample 3D spatiotemporal attractor is presented in Fig. VIII.4. The color-coded arrows marked by 'A', 'B' and 'C' indicate the time points where the heart signals in the corresponding plots (A), (B) and (C) were acquired. At (A), heart activity is normal and the shape of the 3D attractor remains approximately identical in the

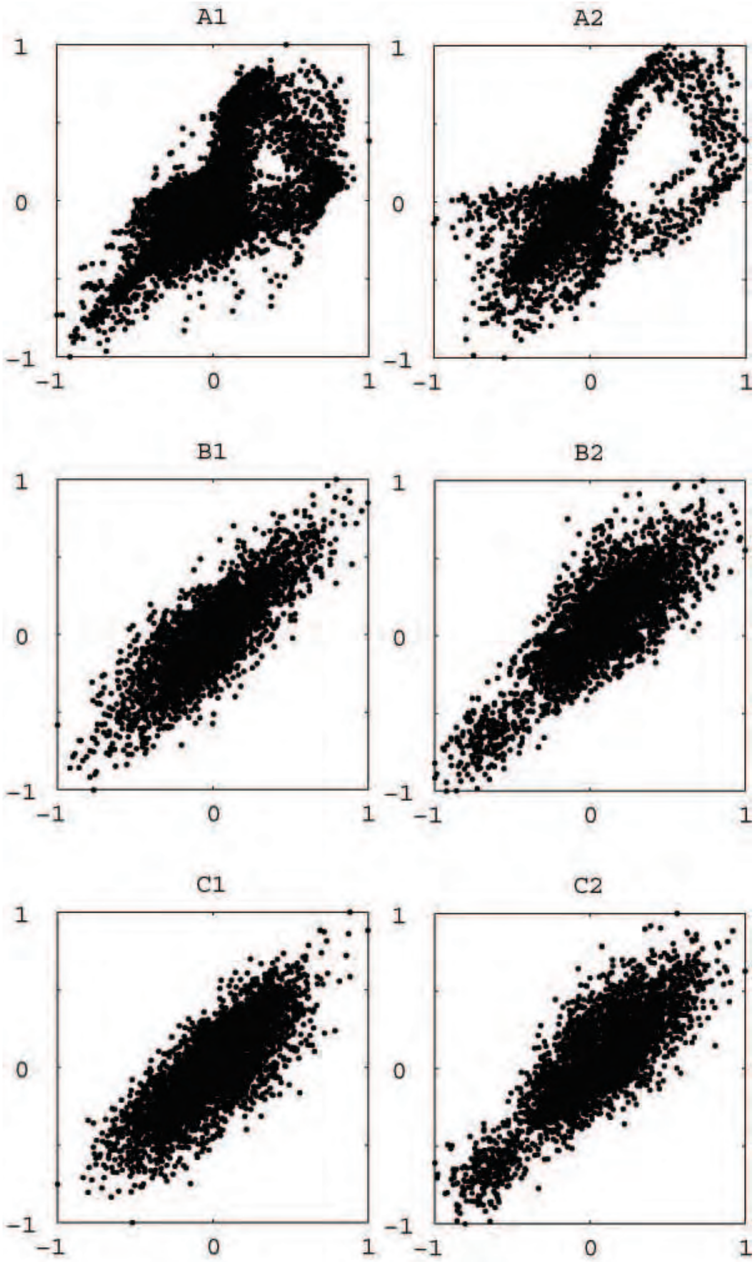

Figure VIII.3: Return maps of healthy (first column) and pathological (second column) signals. The first, second and third rows correspond to the cardiac, gastric and intestinal components, respectively. For ease of comparison, signal normalization was applied so that one common set of axes could be employed for all maps, with limits $x, y \in [-1, +1]$.

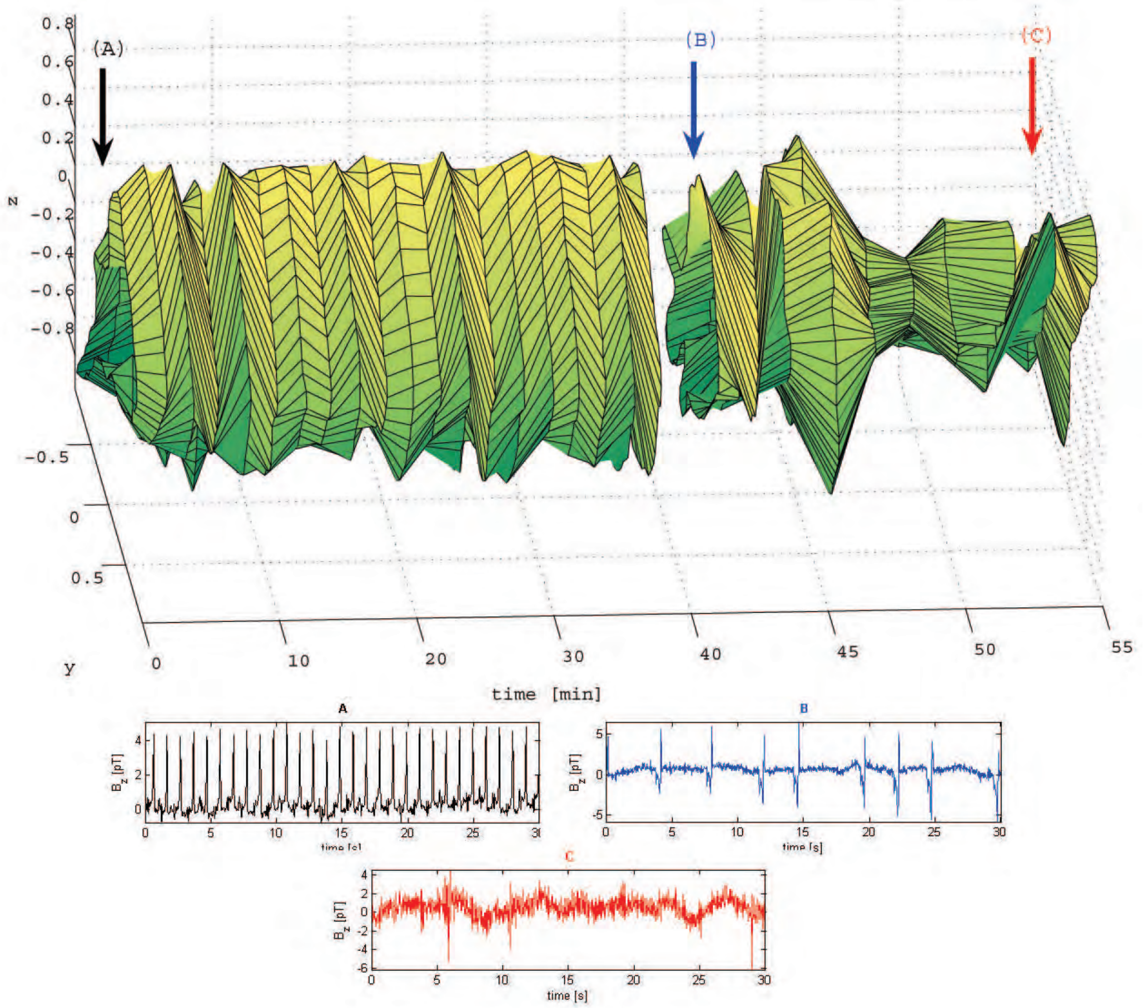

Figure VIII.4: 3D (x, y, t) phase space attractor of cardiac activity evolution in an anesthetized domestic pig across a period of almost one hour of simultaneous MCG/MGG/MENG recordings. The point indicated by arrow (A) corresponds to the data plotted in (A), where cardiac activity is normal. Point (B) corresponds to several minutes after the administration of the euthanasic solution (data plot shown in (B)). At this point, a sharp variation in the chaos content of the system can be seen both from the 3D attractor and from (B) due to cardiac arrhythmia. The amount of chaos varies highly over the ensuing 15 minutes. At (C), cardiac activity has ceased. This makes the S/N ratio drop as a result of heart failure.

time interval between (A) and (B). A few minutes after (B), the euthanizing solution is administered and the resulting arrhythmic cardiac signal leads to large changes in the shape of the 3D attractor. At (C), heart activity has ceased almost entirely and most of the recorded signal consists of environmental noise. In conclusion, our figure demonstrates that, for the example shown, the shape of the 3D attractor is altered significantly when cardiac arrhythmia is present. Similar 3D phase space attractors demonstrating the time evolution of gastric and intestinal signals are shown in Fig. VIII.6. Similarly, while healthy attractors are relatively smooth, large variations in their diameter and shape occur after the onset of arrhythmia.

Before attempting to describe the chaotic content of our acquired signals using the quantitative measures listed in the previous section, we first investigated their convergence behavior as a function of the parameter ϵ. It was thus found that, from among these three measures, the correlation integral $\mathcal{I}$ converged fastest as a function of ϵ. On the other hand, ν and δ were found to best reflect the differences in nonlinear dynamics between the healthy and pathological states that we sought in our study. It was also found that a high degree of correlation existed between the values of ν and δ ($r = 0.996$) whereas hardly any correlation existed between $\mathcal{I}$ and ν ($r = 0.024$) or between $\mathcal{I}$ and δ ($r = 0.021$). Because of this behavior, δ is employed to present our results. The time evolution of this parameter in shown in Fig. VIII.7. Because the purpose of the figure is to demonstrate the common behavior of δ for each animal with respect to time, δ values are shown after normalization, i.e. the normalized quantity $\tilde{\delta} \equiv \delta / \langle \delta_< \rangle$ is plotted, where $\langle \delta_< \rangle$ is the average value of δ before the onset of arrhythmia ($\langle \cdot \rangle$ stands for the average). The average value of δ across all animals ($\langle \delta \rangle$) is also presented in Fig. VIII.7.

It is important to add that, due to experimental protocol issues, each abnormal condition was induced at different times for every subject, such that the moment

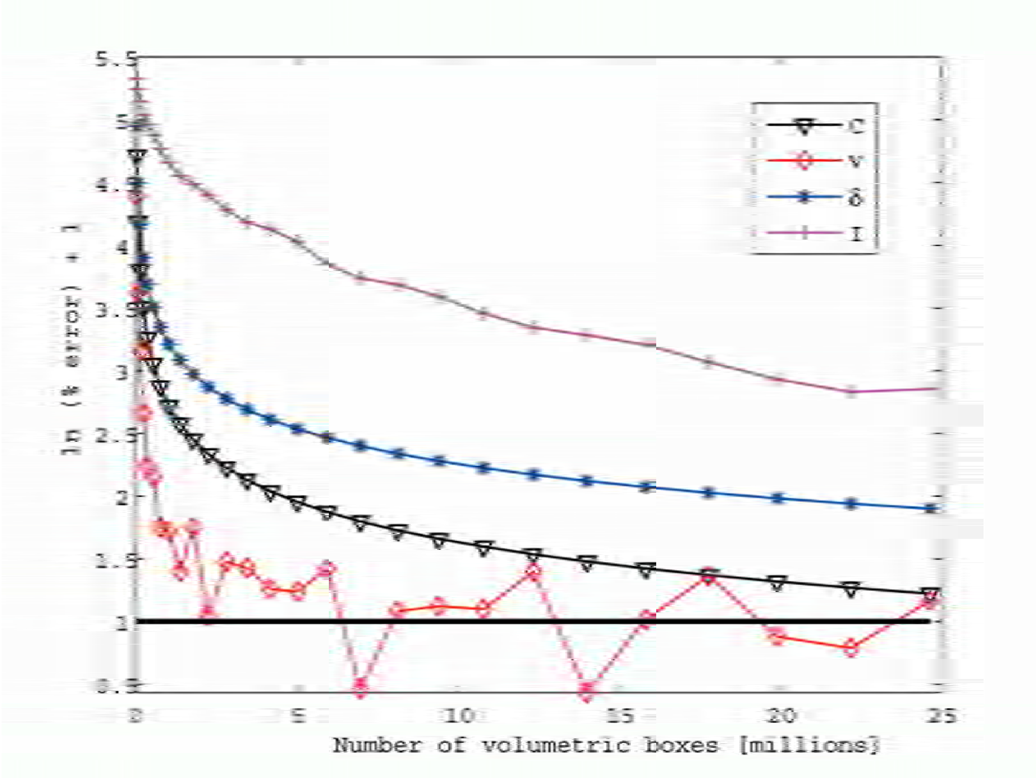

Figure VIII.5: Convergence of the capacity dimension C, information dimension δ, correlation dimension ν and correlation integral $\mathcal{I}$ as a function of the number of volumetric boxes used for their computation (see text for details). The definition used for the percentage error between two successive (previous vs. current) values of each measure was (current - previous) × 100 / max {previous, current}. Values on the abscissa are shown in units of ln (% error) + 1, such that no error (perfect agreement) corresponds to the horizontal line $y = 1$, which is also drawn.

when pathology was established is different for each case. To present all subject data on one plot, time axes were therefore aligned so that the moment when pathology was induced was equal to the time point $t = 0$ min for all data sets. For this reason, each of the plotted functions appears to be of different length since data acquisition periods were different for each subject. From the figure it can be seen that the capacity dimension of the cardiac, gastric and intestinal attractor assumes a relatively constant value during the healthy state. Immediately after the onset of pathology, the value

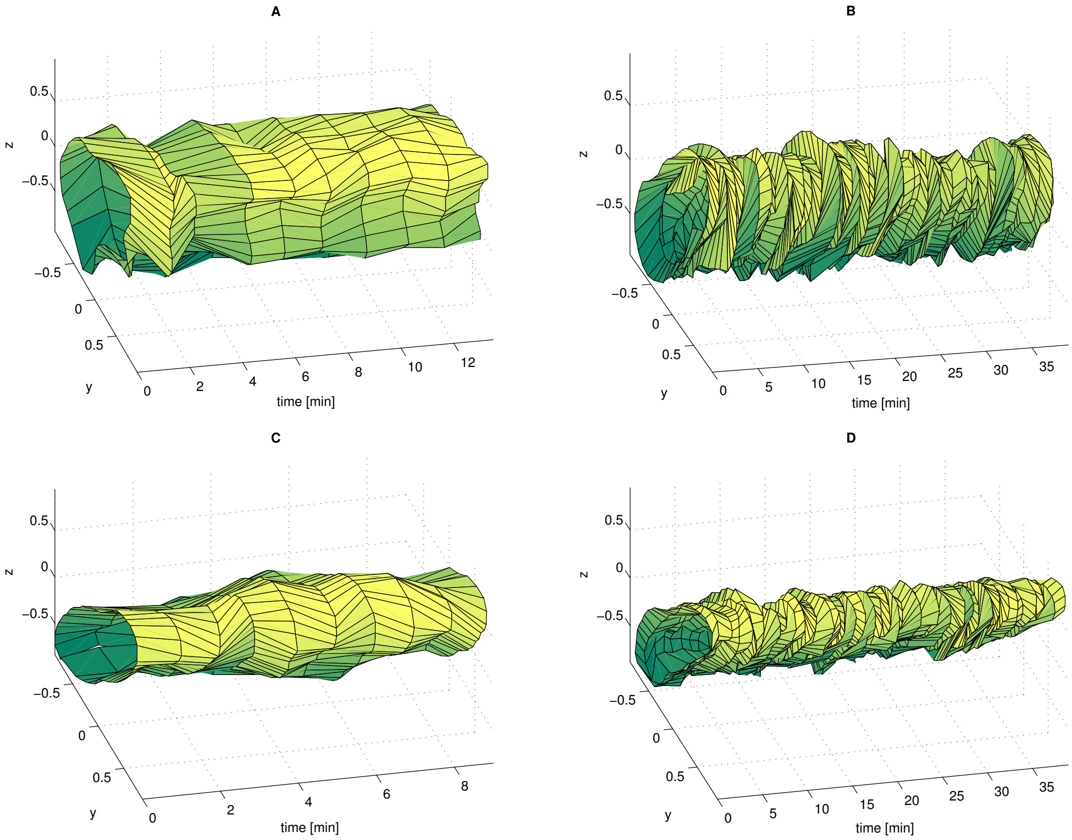

Figure VIII.6: 3D phase space attractors displaying the time evolution of gastric (A, B) and intestinal (C, D) electrical activities in two anesthetized domestic pigs. In the first pig (plots A, B), MGG normal data were first recorded (3D phase space attractor shown in A). The stomach of the first animal was then surgically divided and data were acquired again (attractor shown in B). In the second pig (C, D), MENG normal data were recorded from the bowel (attractor shown in C). Thereafter, intestinal ischemia was induced by ligating the mesenteric artery of the animal and data were acquired again (attractor shown in D). Whereas the diameter of the attractor is relatively time-constant in the healthy state (A and C), it exhibits large variations in the injured state (B, D). The validity of this statement was verified using a statistical confidence test.

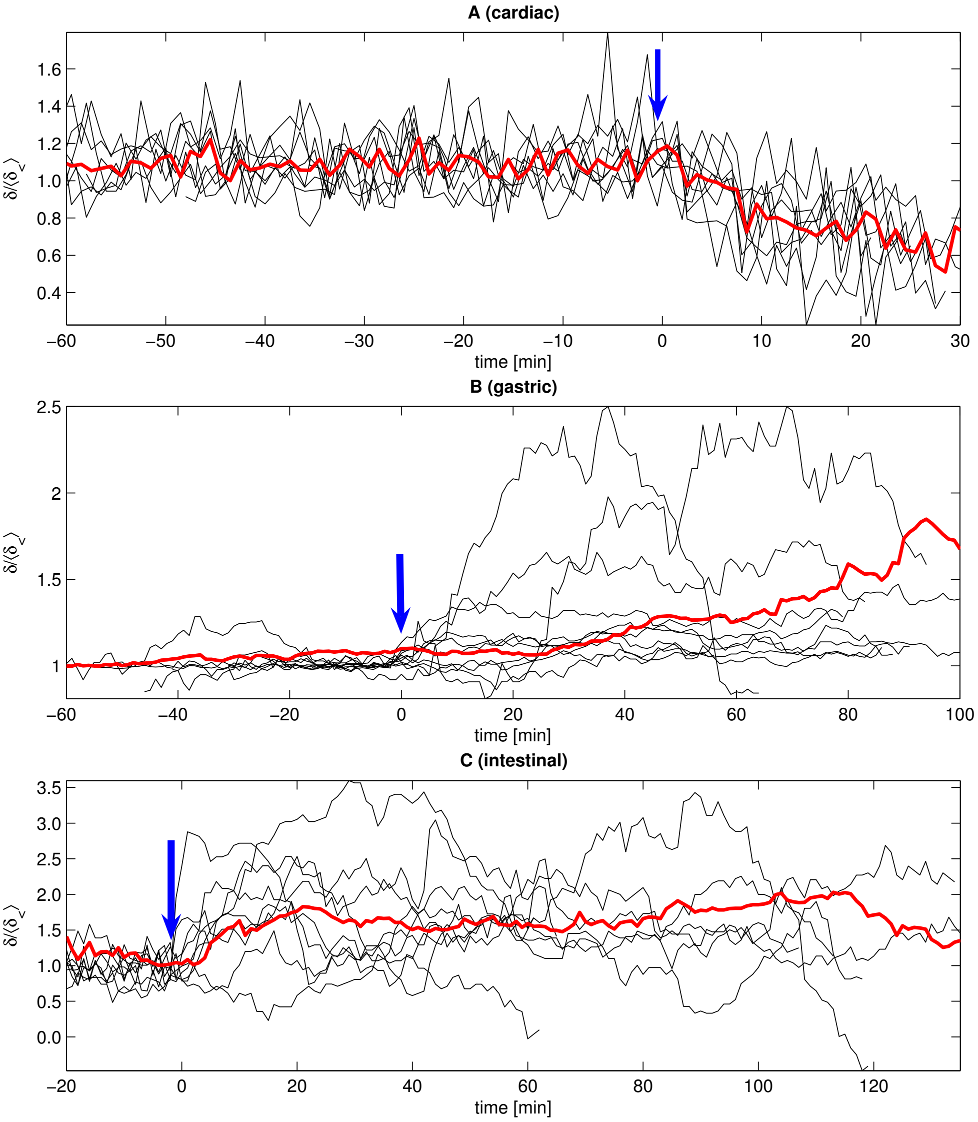

Figure VIII.7: Temporal evolution of the normalized capacity dimension $\tilde{\delta}$ for all subjects (black) and $\langle\delta\rangle$ (red). Changes from normal ($t < 0$ min) to pathological ($t > 0$ min) values of $\tilde{\delta}$ are indicated by blue arrows. These events are euthanasic injection (A), stomach division (B) and mesenteric artery ligation (C). Because experimental recording periods were not equal for each animal, plots are aligned so that the onset of pathology corresponded to the time $t = 0$ min. Nevertheless, recordings from the three organs were acquired *simultaneously* from each animal. Heart rate and $\tilde{\delta}$ values were found to be highly correlated ($r = 0.917$).

of δ fluctuates dramatically such that differences between its pre- and post-operative values become significant. In the case of cardiac activity, as euthanasia is induced and heart activity decreases (see (A)), the capacity dimension decreases to values that are lower than pre-operative ones (this behavior was observed in all subjects).

For most data samples used, δ was found to best reflect the differences between the healthy and pathological states. Because of this, a number of observations regarding the behavior of this parameter are in place. In the case of MGG recordings from normal subjects, because GEA parameters such as frequency and amplitude are approximately constant in time, δ was found to be well behaved, with a normalized variance ($\sigma(\delta)/\langle\delta\rangle$) of 0.12 $\langle\delta\rangle$ across subjects. In the case of pathology, arrhythmia was found to cause abrupt and frequent changes in GEA parameters, which was reflected in the normalized variance of δ having a value of 0.84 $\langle\delta\rangle$ across subjects. These differences in δ were found to be statistically significant ($p < 0.001$). Normalized variances are reported here instead of absolute numbers because the σ statistic was computed across subjects, where large inter-subject differences in δ were found although the time behavior of this parameter was found to be very similar in all cases.

In conclusion, we have presented evidence that−within the framework of a porcine model−cardiac, gastric and intestinal arrhythmias are associated with statistically significant fluctuations in chaotic attractor dimensionality. This phenomenon was described using both visual (attractors) and numerical (capacity dimension time plots) measures. In the case of visual measures, distinguishable differences in attractor shape were made obvious between the healthy and pathological states. In the case of numerical measures, statistically significant differences in $\tilde{\delta}$ were shown to exist between the normal and arrhythmic state of each organ. It appears thus that the ECA-ERA complex−which is somewhat analogous to the PQRST complex of cardiac activity−is excellently suited for investigation via nonlinear analysis methods and it is surprising that chaos theory has received only little attention in this respect. Further study of such differences may one day help to develop novel methods for the noninvasive characterization of gastric disease.

REFERENCES

[1] A Akin and HH Sun (1999) Time-frequency methods for detecting spike activity of stomach *Med Biol Eng Comput* **37** 381-390

[2] A Akin and HH Sun (2002) Non-invasive gastric motility monitor: fast electrogastrogram (fEGG) *Physiol Meas* **23** 505-519

[3] RR Aliev, BN Vasiev (1995) Phase breaks and chaos in a chain of diffusively coupled oscillators *Chaos Solitons & Fractals* **5** 439-445

[4] RR Aliev, WO Richards, JP Wikswo (2000) A simple nonlinear model of electrical activity in the intestine *J Theor Biol* **204** 21-28

[5] SH Allos, DJ Staton, LA Bradshaw, S Halter, JP Wikswo Jr. and WO Richards (1997) Superconducting quantum interference device magnetometer for diagnosis of ischemia caused by mesenteric venous thrombosis *World J Surg* **21** 173-178

[6] WC Alvarez (1921) The electrogastrogram and what it shows *J Amer Med Assoc* **78** 1116-1119

[7] MA Amaris, CP Sanmiguel, DC Sadowski, KL Bowes and MP Mintchev (2002) Electrical activity from colon overlaps with normal gastric electrical activity in cutaneous recordings *Digest Dis Sci* **47** 2480-2485

[8] AA Amini, TE Weymouth and RC Jain (1990) Using dynamic programming for solving variational problems in vision *IEEE Trans Pattern Anal Machine Intel* **12** 855-867

[9] E Atanassova, I Daskalov, I Dotsinsky, I Christov and A Atanassova (1995) Non-invasive electrogastrography Part 1: correlation between the gastric electrical activity in dogs with implanted and cutaneous electrodes *Arch Physiol Biochem* **103** 431-435

[10] E Atanassova, I Daskalov, I Dotsinsky, I Christov and A Atanassova (1995) Non-invasive electrogastrography Part 2: human electrogastrogram *Arch Physiol Biochem* **103** 436-441

[11] A Babloyantz, A Destexhe (1986) Low-dimensional chaos in an instance of epilepsy *Proc Natl Acad Sci USA* **83** 3513-3517

[12] S Baillet, JC Mosher and RM Leahy (2001) *IEEE Signal Proc Mag* **18** 14-30

[13] J Balatoni and A. Rényi (1976) Selected papers of A. Rényi Budapest: Akademiai Budapest.

[14] AJ Bell and TJ Sejnowski (1995) An information maximization approach to blind separation and blind deconvolution *Neural Computation* **7** 1129-1159

[15] D Bonaduce, M Petretta, F Marciano, MLE Vicario, C Apicella, MAE Rao, E Nicolai, M Volpe (1999) Independent and incremental prognostic value of heart rate variability in patients with chronic heart failure *Am Heart J* **138** 273-284

[16] A Bortoff, D Michaels and P Mistretta (1981) Dominance of longitudinal muscle in propagation of intestinal slow waves *Am J Physiol: Cell Physiol* **240** C135-C147

[17] A Bortoff and LF Sillin (1986) Changes in intercellular electrical coupling of smooth muscle accompanying atrophy and hypertrophy *Am J Physiol Cell Physiol* **250** C292-C298

[18] M Bortolotti (1998) Electrogastrography: a seductive promise, only partially kept *Am J Gastroenterol* **93** 1791-1794

[19] E Bozler (1945) The action potentials of the stomach *Am J Physiol* **144** 693-700

[20] LA Bradshaw (1995) Measurement and modeling of gastrointestinal bioelectric and biomagnetic fields *PhD dissertation* Vanderbilt University, Nashville TN

[21] LA Bradshaw, SH Allos, JP Wikswo, Jr. and WO Richards (1997) Correlation and comparison of magnetic and electric detection of small intestinal electrical activity *Am J Physiol: Gastrointest Liver Physiol* **272** G1159-1167

[22] LA Bradshaw, JK Ladipo, DJ Staton, JP Wikswo, Jr. and WO Richards (1999) The human vector magnetogastrogram and magnetoenterogram *IEEE Trans Biomed Eng* **46** 959-971

[23] LA Bradshaw, WO Richards and JP Wikswo Jr. Volume conductor effects on the spatial resolution of magnetic fields and electric potentials from gastrointestinal electrical activity *Med Biol Eng Comput* **39** 35-43

[24] LA Bradshaw, RS Wijesinghe, and JP Wikswo Jr. (2001) Spatial filter approach for comparison of the forward and inverse problems of electroencephalography and magnetoencephalography *Ann Biomedical Eng* **29** 214-226

[25] LA Bradshaw, AG Myers, JP Wikswo Jr. and WO Richards (2003) A spatiotemporal dipole simulation of gastrointestinal magnetic fields *IEEE Trans Biomed Eng* **50** 836-847

[26] LA Bradshaw, A Irimia, JA Sims, RL Palmer, WO Richards (2006) Biomagnetic characterization of spatiotemporal parameters of the gastric slow wave *Neurogastroenterol Motil in press*

[27] C Braun, P Kowallik, A Freking, D Hadeler, KD Kniffki, M Meesmann (1998) Demonstration of nonlinear components in heart rate variability of healthy persons *Am J Physiol Heart Circ Physiol* **44** H1577-H1584

[28] NF Britton (1986) Reaction-diffusion equations and their applications to biology (London: Academic)

[29] RJ Brzana, KL Koch and S Bingaman (1998) Gastric myoelectrical activity in patients with gastric outlet obstruction and idiopathic gastroparesis *Am J Gastroenterol* **93** 1803-1809

[30] ML Buist, LK Cheng, R Yassi, LA Bradshaw, WO Richards and AJ Pullan (2003) An anatomical model of the gastric system for producing bioelectric and biomagnetic fields *Physiol Meas* **25** 849-861

[31] WE Byerly (1893) *An Elementary Treatise on Fourier Series and Spherical, Cylindrical and Ellipsoidal Harmonics, with Applications to Problems in Mathematical Physics.* Ginn & Co., Boston.

[32] M Camilleri, WL Hasler, HP Parkman, EMM Quigley and E Soffer (1998) Measurement of gastrointestinal motility in the GI laboratory *Gastroenterol* **115** 747-762

[33] J-F Cardoso (1998) Blind signal separation: statistical principles *Proc IEEE* **86** 2009-2025

[34] C Chatfield and AJ Collins (1980) Introduction to multivariate analysis *Chapman & Hall*: London, UK

[35] D Cohen (1968) Magnetoencephalography: evidence of magnetic fields produced by alpha-rhythm currents *Science* **161** 784-786

[36] D Cohen, EA Edelsack, JE Zimmerman (1970) Magnetocardiograms taken inside a shielded room with a superconducting point-contact magnetometer *Appl Phys Lett* **16** 278-280

[37] D Cohen (1972) Magnetoencephalography: Detection of the brain's electrical activity with a superconducting magnetometer *Science*, **175**, 664-666.

[38] A Cohen (1988) Biomedical signal processing vol 2 *CRC*: Boca Raton, FL 121-124

[39] TF Coleman and Y Li 1994 *Math. Program.* **67**, 189-224.

[40] TF Coleman and Y Li 1996 *SIAM J. Optimiz.* **6**, 418-445.

[41] S Comani, S Conforto, D di Nuzzo, M Basile, S di Luzio, SN Erné and GL Romani (1996) Non-invasive detection of gastric myoelectrical activity: comparison between results of magnetogastrography and electrogastrography in normal subjects *Phys Med* **12** 35-4

[42] S Comani, D Mantini, A Lagatta, F Esposito, S di Luzio and GL Romani (2004) Time-course reconstruction of fetal cardiac signals from fMCG: independent component analysis versus adaptive maternal beat subtraction *Physiol Meas* **25** 1305-1321

[43] Dassios G. (1981) *J. Accoust. Soc. Am.* **70**, 176-185.

[44] G Dassios and F Kariotou (2003) *J. Math. Phys.* **44**, 220-241.

[45] A Delorme, S Makeig, M Fabre-Thorpe, TJ Sejnowski (2002) From single-trial EEG to brain area dynamics *Neurocomput* **44-46** 1057-1064

[46] D Dechambre and DJ Scheeres (2002) Transformation of spherical harmonic coefficients to ellipsoidal harmonic coefficients *Astron Astrophys* **387** 1114-1122

[47] NE Diamant, A Bartoff (1969) Nature of the intestinal slow wave frequency gradient *American Journal of Physiology*, **216**, 301-307.

[48] L Elden, A Bortoff (1984) Electrical coupling of longitudinal and circular intestinal muscle *Am J Physiol: Gastrointest Liver Physiol* **246** G618-G626

[49] T Elbert, WJ Ray, ZJ Kowalik, JE Skinner, KE Graf and N Birbauer (1994) Chaos and physiology: deterministic chaos in excitable cell assemblies *Physiol Rev* **74** 1-47

[50] JE Everhart (1994) Digestive diseases in the United States: epidemiology and impact. U.S. Department of Heath and Human Services, National Institutes of Health, National Institute of Diabetes and Digestive and Kidney Diseases. U.S. Government Printing Office, Washington D.C.

[51] BS Everitt and G Dunn (1992) Applied multivariate data analysis *Oxford University Press*: New York, NY 45-64

[52] BO Familoni, YJ Kingma and KL Bowes (1987) Noninvasive assessment of human gastric motor function *IEEE Trans Biomed Eng* **34** 30-36

[53] BO Familoni, TL Abell and KL Bowes (1995) A model of gastric electrical activity in health and disease *IEEE Trans Biomed Eng* **42** 647-657

[54] WE Featherstone and MC Dentith (1997) A geodetic approach to gravity data reduction for geophysics *Comput Geosci* **23** 1063-1070

[55] E Frank (1952) Electric potential produced by two point current sources in a homogeneous conducting sphere *J Appl Phys* **23** 1225-1228

[56] J Garcia-Casado, JL Martinez-de-Juan and JL Ponce (2005) Noninvasive measurement and analysis of intestinal myoelectrical activity using surface electrodes *IEEE Trans Biomed Eng* **52** 983-991

[57] A Garfinkel, PS Chen, DO Walter, HS Karagueuzian, B Kogan, SJ Evans, M Karpoukhin, C Hwang, T Uchida, M Gotoh, O Nwasokwa, P Sager, JN Weiss (1997) Quasiperiodicity and chaos in cardiac fibrillation *J Clin Invest* **99** 305-314

[58] RP Gaumond, J-H Lin and DB Geselowitz (1983) Accuracy of dipole localization with a spherical homogeneous model *IEEE Trans Biomed Eng* **30** 29-34

[59] L Glass and MC Mackey (1988) From clocks to chaos: the rhythms of life (Princeton, NJ: Princeton University Press)

[60] AL Goldberger, LAN Amaral, JM Hausdorff, PC Ivanov, CK Peng, HE Stanley (2002) Fractal dynamics in physiology: alterations with disease and aging *Proc Natl Acad Sci USA* vol 99 2466-2472

[61] Gray A in *Modern Differential Geometry of Curves and Surfaces with Mathematica*, 2nd ed., Boca Raton, FL: CRC Press, 108-111.

[62] D Gutiérrez, A Nehorai and H Preissl (2005) Ellipsoidal head model for fetal magnetoencephalography: forward and inverse solutions *Phys Med Biol* **50** 2141-2157

[63] AC Guyton and JE Hall (2006) Textbook of medical physiology *11th edition* Elsevier Inc. Philadelphia PA

[64] MS Hämäläinen and J. Sarvas (1987) Feasibility of the homogeneous head model in the interpretation of neuromagnetic fields *Phys Med Biol* **32** 91-97

[65] MS Hämäläinen and J. Sarvas (1989) Realistic conductivity geometry model of the human head for interpretation of neuromagnetic data *IEEE Trans Biomed Eng* **36** 165-171

[66] MS Hämäläinen, R Hari, RJ Ilmoniemi, J Knuutila and O Lounasmaa (1993) Magnetoencephalography-theory, instrumentation, and applications to noninvasive studies of the working human brain *Rev Mod Phys* **65** 413-497

[67] JW Hamilton, BE Bellahsene, M Reichelderfer, JG Webster and P Bass (1986) Human electrogastrograms: comparison of surface and mucosal recordings *Digest Dis Sci* **31** 33-39

[68] P Hanson, BL Bardakjian, NE Diamant (1990) Chaos in coupled nonlinear gastric oscillators *Mathl Comput Modelling* **14** 586-591

[69] RJ Harris (1975) A primer of multivariate statistics *Academic*: New York, NY 156-204

[70] S He and M Norgren (2000) Magnetostatic image current and its application to an analytic identification of a current dipole inside a conducting sphere *IEEE Trans Biomed Eng* **47** 183-191

[71] SS Hegde, SA Seidel, JK Ladipo, LA Bradshaw, S Halter and WO Richards (1998) Effects of mesenteric ischemia and reperfusion on small bowel electrical activity *J Surg Research* **74** 86-95

[72] Hobson EW 1931 *The Theory of Spherical and Ellipsoidal Harmonics*, Cambridge University Press, Cambridge, U.K.

[73] M Jiménez, JR Borderies, P Vergara, YF Wang and EE Daniel (1999) Slow waves in circular muscle of porcine ileum: structural and electrophysiological studies *Am J Phisiol Gastrointest Liver Physiol* **39** G393-G406

[74] EW Hobson (1955) The theory of spherical and ellipsoidal harmonics *Cambridge University Press* Cambridge UK

[75] K Horiguchi, GSA Semple, KM Sanders and SM Ward (2001) Distribution of pacemaker function through the tunica muscularis of the canine gastric antrum *J Physiol* **537.1** 237-250

[76] B Horowitz, SM Ward and KM Sanders (1999) Cellular and molecular basis for electrical rhythmicity in gastrointestinal muscles *Annu Rev Physiol* **61** 19-43

[77] M Hotokezaka, EP Mentis, BD Schirmer (1996) Gastric myoelectric activity changes following open abdominal surgery in humans *Digest Dis Sci* **41** 864-869

[78] JD Huiziga (2001) Physiology and pathophysiology of the interstitial cells of Cajal: from bench to bedside II. Gastric motility: lessons from mutant mice on slow waves and innervation. *American Journal of Physiology: Gastrointestinal and Liver Physiology*, **281**, G1129-G1134.

[79] A Hyvärinen and E Oja (1997) A fast fixed-point algorithm for independent component analysis *Neural Comput* **9** 1483-1492

[80] A Hyvärinen, E Oja, PO Hoyer and J Hurri (1995) Image feature extraction by sparse coding and independent component analysis in *Proc Int Conf Pattern Recognition (ICPR '98)* Brisbane, Australia 1268-1273

[81] A Hyvärinen (1999) Survey on independent component analysis *Neural Comput Surveys* **2** 94-128

[82] A Hyvärinen (1999) Fast and robust fixed-point algorithms for independent component analysis *IEEE Trans Neural Networks* **10** 626-634

[83] A Hyvärinen and E Oja (2000) Independent component analysis: algorithms and applications *Neural Networks* **13** 411-430

[84] A Irimia, LA Bradshaw (2002) Theoretical models and biomathematical algorithms for identifying multiple gastrointestinal dipoles *Proceedings of the IASTED International Conference on Applied Modeling and Simulation*, ACTA Press, Anaheim, CA, 56-60.

[85] A Irimia, LA Bradshaw (2002) Recursively-applied scanning algorithms for inverse biomagnetic analyses of gastrointestinal biomagnetic fields *Proceedings of the IASTED International Conference on Applied Modeling and Simulation, 2002*, ACTA Press, Anaheim, CA, 51-55.

[86] A Irimia (2002) Three-dimensional simulations of the gastric biomagnetic field using a recursive dipole localization algorithm *Proceedings of the IASTED International Conference on Applied Modeling and Simulation, 2002*, ACTA Press, Anaheim, CA, 45-50.

[87] A Irimia and LA Bradshaw (2003) Theoretical ellipsoidal model of gastric electrical control activity propagation *Phys Rev E* **68** 051905

[88] A. Irimia, JJ Beauchamp, LA Bradshaw (2004) Theoretical and computational multiple regression study of gastric electrical activity using dipole tracing from magnetic field measurements. *Journal of biological physics*, accepted.

[89] A Irimia and LA Bradshaw (2004) Theoretical and computational methods for the noninvasive detection of gastric electrical source coupling *Phys Rev E* **69** 051920

[90] A Irimia, LA Bradshaw (2005) Artifact reduction in magnetogastrography using fast independent component analysis *Physiol Meas* vol 26 1059-1073

[91] A Irimia, WO Richards, LA Bradshaw (2005) Magnetogastrographic detection of gastric electrical response activity in humans *Am J Physiol: Gastrointest Liver Physiol* in press

[92] A Irimia and LA Bradshaw (2005) Ellipsoidal electrogastrographic forward modelling *Phys Med Biol* **50** 4429-4444

[93] A Irimia (2005) Calculation of the magnetic field due to a bioelectric current dipole in an ellipsoid *J Phys A* in press

[94] Irimia A. 2005 *To be submitted.*

[95] PC Ivanov, LAN Amaral, AL Goldberger, S Havlin, MG Rosenblum, ZR Struzik, HE Stanley (1999) Multifractality in human heartbeat dynamics *Nature* vol 399 461-465

[96] WG Jenks, SSH Sadeghi, JP Wikswo Jr. (1997) SQUIDS for nondestructive evaluation. *Journal of Physics D: Applied Physics* **30**, 293-323.

[97] WG Jenks, IM Thomas and JP Wikswo Jr. (1997) SQUIDS in *Encyclopedia of Applied Physics* **19** 457-468.

[98] T-P Jung,S Makeig, C Humphries, T-W Lee, MJ McKeown, V Iragui and TJ Sejnowski (2000) Removing electroencephalographic artifacts by blind source separation *Psychophysiol* **37** 163-178

[99] F Kariotou (2004) Electroencephalography in ellipsoidal geometry *J Math Anal Appl* **290** 324-342

[100] KL Koch (1999) Diabetic gastropathy: gastric neuromuscular dysfunction in diabetes mellitus. A review of symptoms, pathophysiology and treatment. *Digestive Diseases and Sciences* **44**, 1061-1075.

[101] KL Koch (2001) Electrogastrography: physiological basis and clinical application in diabetic gastropathy *Diabetes Tech Therap* **3** 51-62

[102] L de Lathauwer, B de Moor and J Vandewalle (2000) Fetal electrocardiogram extraction by blind source subspace separation *IEEE Trans Biomed Eng* **47** 567-572

[103] J Liang, JDZ Chen (1997) What can be measured from surface electrogastrography - computer simulations *Digest Dis Sci* **42** 1331-1343

[104] H Liang (2005) Extraction of gastric slow waves from electrogastrograms: combining independent component analysis and adaptive signal enhancement *Med Biol Eng Comput* **43** 245-251

[105] X Lin, J Hayes, LJ Peters and JDZ Chen (2000) Entrainment of intestinal slow waves with electrical stimulation using intraluminal electrodes *Ann Biomed Eng* **28** 582-587

[106] Z Lin, JDZ Chen, BD Schirmer and RW McCallum (2000) Postprandial response of gastric slow waves: correlation of serosal recordings with the electrogastrogram *Digest Dis Sci* **45** 645-651

[107] D Luenberger (1969) Optimization by vector space methods *Wiley* 1969

[108] S Makeig, AJ Bell, T-P Jung and TJ Sejnowski (1996) Independent component analysis of electroencephalographic data *Adv Neural Info Proc Sys* **8** 145-151

[109] S Makeig, T-P Jung, AJ Bell, D Ghahremani and TJ Sejnowski (1997) Blind separation of auditory event-related brain responses into independent components *Proc Natl Acad Sci USA* **94** 10979-10984

[110] TH Mäkikallio, J Koistinen, L Jordaens, MP Tulppo, N Wood, B Golosarsky, CK Peng, AL Goldberger, HV Huikuri (1999) Heart rate dynamics before spontaneous onset of ventricular fibrillation in patients with healed myocardial infarcts *Am J Cardiol* **83** 880-884

[111] J Malmivuo and R Plonsey (1995) Bioelectromagnetism *Oxford University Press* New York, NY

[112] MP Mintchev, SJ Otto and KL Bowes (1997) Electrogastrography can recognize gastric electrical uncoupling in dogs *Gastroenterol* **112** 2006-2011

[113] T Miloh (1973) Forces and moments on a triaxial ellipsoid in potential flow *Israel J Tech* **11** 63-74.

[114] M.P. Mintchev and K.L. Bowes, Med. Biol. Eng. Comput. **33**, (1995) 179-184.

[115] MP Mintchev, SJ Otto, KL Bowes (1997) Electrogastrography can recognize gastric electrical uncoupling in dogs *Gastroenterology* **112**, 2006-2011.

[116] MP Mintchev, A Stickel, SJ Otto, KL Bowes (1997) Reliability of percent distribution of power of the electrogastrogram in recognizing gastric electrical uncoupling *IEEE Transactions on Biomedical Engineering* **44**, 1288-1291.

[117] MP Mintchev and KL Bowes (1998) Computer simulation of the impact of different dimensions of the stomach on the validity of electrogastrograms *Med Biol Eng Comput* **36** 95-100

[118] MP Mintchev, A Stickel, KL Bowes (1998) Dynamics of the level of randomness in gastric electrical activity *Digest Dis Sci* **43** 953-956

[119] MP Mintchev, A Girard, KL Bowes (2000) Nonlinear adaptive noise compensation in electrogastrograms recorded from healthy dogs *IEEE Transactions on Biomedical Engineering* **47**, 239-248.

[120] N Mirizzi and U Scafoglieri (1983) Optimal direction of the elegrogastrographic signal in man *Med Biol Eng Comput* **21** 385-389

[121] N Mirizzi, R Stella, U Scafoglieri (1985) A model of extracellular waveshape of the gastric electrical activity *Med Biol Eng Comput* **23** 33-37

[122] N Mirizzi, R Stella, U Scafoglieri (1986) Model to simulate the gastric electrical control and response activity on the stomach wall and on the abdominal surface *Medical & Biological Engineering and Computing*, **24**, 157-163.

[123] DF Morisson (1967) Multivariate statistical methods *McGraw-Hill*: New York, NY

[124] P.M. Morse and H. Feschbach 1953 *Methods of Theoretical Physics, Part 1*, McGraw-Hill: New York, pp. 663.

[125] JC Mosher, RM Leahy and PS Lewis (1992) Multiple dipole modeling and localization from spatiotemporal MEG data *IEEE Trans Biomed Eng* **42** 541-557

[126] JC Mosher (1993) Localization from near-source quasi-static electromagnetic fields *PhD thesis* University of Southern California 16-19

[127] TS Nelsen, JC Becker (1968) Simulation of the electrical and mechanical gradient of the small intestine *American Journal of Physiology* **214** 749-757.

[128] Niven W.D. 1891 *Phil. Trans.* **187**, 231.

[129] G Nolte and G Curio (1999) The effect of artifact rejection by signal-space projection on source localization accuracy in MEG measurements *IEEE Trans Biomed Eng* **46** 400-408

[130] D O'Donovan, C Feinle-Bisset, K Jones, M Horowitz (2003) Idiopathic and diabetic gastroparesis. *Current Treatment Options in Gastroenterology* **6** 299-309.

[131] YC Okada, M Lauritzen and C Nicholson (1987) *Phys Med Biol* **32** 43-51

[132] VE Orel, AV Romanov, NN Dzyatkovskaya, YI Melnik (2002) An algorithm for estimating chaos in mechanoemission of blood and magnetic resonance imaging in patients with gastric cancer *Ann N Y Acad Sci* **972** 144-150

[133] H Ouyang, J Yin, ZS Wang, PJ Pasricha and JDZ Chen (2002) Electroacupuncture accelerates gastric emptying in association with changes in vagal activity *Am J Physiol Gastrointest Liver Physiol* **282** G390-G396

[134] RL Palmer (2005) Characterization of gastric electrical activity using a noninvasive SQUID magnetometer *PhD Thesis, Vanderbilt University*

[135] HP Parkman, WL Hasler, JL Barnett and EY Eaker (2003) Electrogastrography: a document prepared by the gastric section of the American Motility Society Clinical GI Motility Testing Task Force *Neurogastroenterol Motil* **15** 89-102

[136] JW Phillips, RM Leahy, JC Mosher and B Timsari (1997) *IEEE Eng Med Biol 0739-5157* 34-42

[137] NG Publicover and KM Sanders (1989) Are relaxation oscillators an appropriate model of the gastrointestinal electrical activity? *Am J Physiol* pt.1 **256** G265-G274

[138] A Pullan, LK Cheng, R Yassi, M Buist (2004) Modeling gastrointestinal bioelectric activity. Progress in Biophysics and Molecular Biology, **85**, 523-550.

[139] C Purcell, T Mashiko, K Okada and K Ueno (1991) Describing head shape with surface harmonic expansions *IEEE Trans Biomed Eng* **38** 303-306

[140] LW Qian, PJ Pasricha and JDZ Chen (2003) Origins and patterns of spontaneous and drug-induced canine gastric myoelectrical dysrhythmia *Digest Dis Sci* **48** 508-515

[141] R Quian Quiroga, A Kraskov, T Kreuz, P Grassberger (2002) Performance of different synchronization measures in real data: a case study on electroencephalographic signals *Phys Rev E* **65** 041903

[142] PZ Rashev, MP Mintchev and KL Bowes (2000) Application of an object-oriented programming paradigm in three-dimensional computer modeling of mechanically active gastrointestinal tissues *IEEE Trans Info Technol Biomed* **4** 247-258

[143] PZ Rashev, KL Bowes, and M.P. Mintchev (2002) Three-dimensional object-oriented modeling of the stomach for the purpose of microprocessor-controlled functional stimulation *IEEE Trans Info Technol Biomed* **6** 296-309

[144] WO Richards, CL Garrard, SH Allos, LA Bradshaw, DJ Staton and JP Wikswo (1995) *Ann Surg* **221** 696-705

[145] S Ritter (1995) A sum-property of the eigenvalues of the electrostatic integral operator *J Math Anal Appl* **196** 120-134

[146] S Ritter (1997) On the magnetostatic integral operator for ellipsoids *J Math Anal Appl* **207** 12-28

[147] S Ritter (1998) The nullfield method for the ellipsoidal Stokes problem *J Geodesy* **72** 101-106

[148] S Ritter (1998) On the computation of Lamé functions, of eigenvalues and eigenfunctions of some potential operators *ZAMM - Z Angew Math Mech* **78** 66-72

[149] G Romain and JP Barriot (2001) Ellipsoidal harmonic expansions of the gravitational potential: theory and application *Celest Mech Dyn Astr* **79** 235-275

[150] RD Rothstein, A Alavi and JC Reynolds (1993) Electrogastrography in patients with gastroparesis and effect of long-term cisapride *Digest Dis Sci* **35** 1518-1524

[151] EB Saff, AD Snider (2003) Fundamentals of complex analysis with applications to engineering, science, and mathematics (3rd edition) Prentice Hall, NJ

[152] KM Sanders (1996) A case for interstitial cells of Cajal as pacemakers and mediators of neurotransmission in the gastrointestinal tract *Gastroenterol* **111** 492-515

[153] DT Sandwell (1987) Biharmonic spline interpolation of GEOS-3 and SEASAT altimeter data *Geophys Research Lett* **2** 139-142

[154] SK Sarna, EE Daniel, YJ Kingma (1971) Simulation of slow-wave electrical activity of small intestine *Am J Physiol* **221** 166-175

[155] SK Sarna, EE Daniel, YJ Kingma (1972) Simulation of the electric-control activity of the stomach by an array of relaxation oscillators *Digest Dis Sci* **17** 299

[156] SK Sarna, EE Daniel, YJ Kingma (1972) Premature control potentials in the dog stomach and in the gastric computer model *Am J Physiol* **222** 1518-1513

[157] SK Sarna, KL Bowes, EE Daniel (1976) Gastric pacemakers *Gastroenterology* **70** 226-231.

[158] J Sarvas (1987) Basic mathematical and electromagnetic concepts of the biomagnetic inverse problem *Phys Med Biol* **32** 11-22

[159] JA Schmidt and TC Pilkington (1991) The volume conductor effects of anisotropic muscle on body surface potentials using an eccentric spheres model *IEEE Trans Biomed Eng* **38** 300-303

[160] R Serio, C Barajas-Lopez, EE Daniel, I Berezin and JD Huizinga (1991) Slow-wave activity in colon: role of network of submucosal interstitial cells of Cajal *Am J Physiol* **260** G636-645

[161] TY Sharkawi, KG Morgan and JH Szurszewski (1978) Intracellular electrical activity of canine and human gastric smooth muscle *J Physiol London* **279** 291

[162] DS Smith, CS Williams and CD Ferris (2003) Diagnosis and treatment of chronic gastroparesis and chronic intestinal pseudo-obstruction *Gastroenterol Clin North Am* **32** 618-+

[163] AJPM Smout, EJ van der Scee, JL Grashuis (1980) What is measured in electrogastrography? *Digestive Diseases and Sciences* **25** 179-187.

[164] A Sommerfeld (1952) Electrodynamics *Academic Press* New York, NY

[165] G Sona (1995) Numerical problems in the computation of ellipsoidal harmonics *J Geodesy* **70** 117-126

[166] CJ Stam (2005) Nonlinear dynamical analysis of EEG and MEG: review of an emerging field *Clin Neurophysiol* vol 116 2266-2301

[167] D Staton, J Golzarian, JP Wikswo, RN Friedman and WO Richards (1995) Measurements of small bowel electrical activity in vivo using a high-resolution SQUID magnetometer *Biomagnetism: fundamental research and clinical applications Elsevier: Boston, MA* 748-752

[168] G Sugihara, W Allan, D Sobel, KD Allan (1996) Nonlinear control of heart rate variability in human infants *Proc Natl Acad Sci USA* **93** 2608-2613

[169] F Takens (1981) Detecting strange attractors in turbulence *Lecture Notes Math* **898** 366-381

[170] AC Tang, BA Pearlmutter, NA Malaszenko, DB Phung and BC Reeb (2002) Independent components of magnetoencephalography: localization *Neural Comput* **14** 1827-1858

[171] AC Tang, BA Pearlmutter, NA Malaszenko, DB Phung and BC Reeb (2002) Independent components of magnetoencephalography: single-trial response onset times *NeuroImage* **17** 1773-1789

[172] D Terasaka, A Bortoff and LF Sillin (1989) Postprandial changes in intestinal slow-wave propagation reflect a decrease in cell coupling *Am J Physiol: Gastrointest Liver Physiol* **257** G463-G469

[173] JH Tripp (1983) Biomagnetism: an interdisciplinary approach *Williamson, Romani, Kaufman & Modena, eds* NATO ASI Series A: Life Sciences **66** 101-140

[174] Tristan Technologies, Inc. (2004) *Intestinal ischemia system - Model 637.* http:www.tristantech.comprod_gut.html, accessed on July 10, 2004.

[175] GK Turnbull, SP Ritcey, G Stroink, B Brandts and P van Leeuwen (1999) Spatial and temporal variations in the magnetic fields produced by human gastrointestinal activity *Med Biol Eng Comput* **37** 549-554

[176] MAMT Verhagen, M Samson and AJPM Smout (1998) Gastric myoelectrical and antroduodenal motor activity in patients with achalasia *Neurogastroenterol Mot* **10** 211-218

[177] R Vigário, V Jousmäki, M Hämäläinen, R Hari and E Oja (1996) Independent component analysis for identification of artifacts in magnetoencephalographic recordings *Adv Neural Info Proc Sys* **10** 229-235

[178] RN Vigario (1997) Extraction of ocular artefacts from EEG using independent component analysis *Electroencephalogr Clin Neurophysiol* **103** 395-404

[179] R Vigário, J Särelä, V Jousmäki, M Hämäläinen and E Oja (2000) Independent component approach to the analysis of EEG and MEG recordings *IEEE Trans Biomed Eng* **47** 589-593

[180] J Vrba and SE Robinson (2001) Signal processing in magnetoencephalography *Methods* **25** 249-271

[181] J Vrba, SE Robinson, J McCubbin, P Murphy, H Eswaran, JD Wilson, H Preissl and CL Lowery (2004) Human fetal brain imaging by magnetoencephalography: verification of fetal brain signals by comparison with fetal brain models *Neuroimage* **21** 1009-1020

[182] ZS Wang and JDZ Chen (2001) Blind separation of slow waves and spikes from gastrointestinal myoelectrical recordings *IEEE Trans Info Tech Biomed* **5** 133-137.

[183] ZS Wang, Z He and JDZ Chen (2004) Chaotic behavior of gastric migrating myoelectrical complex *IEEE Trans Biomed Eng* **51** 1401-1406

[184] ZS Wang, Z He and JDZ Chen (2005) Robust time delay estimation of bioelectric signals using least absolute deviation neural network *IEEE Trans Biomed Eng* **52** 454-462

[185] N Weisbrodt (1987) Motility of the small intestine, *Physiology of the Gastrointestinal tract*, Raven Press, New York.

[186] JP Wikswo, A Gevins and SJ Williamson (1993) The future of EEG and MEG *Electroencephalogr Clin neurophysiol* **87** 1-9

[187] JP Wikswo, Jr. (1995) SQUID magnetometers for biomagnetism and nondestructive testing: important questions and initial answers. *IEEE Trans. Applied Supercond.* **5**, 74-80.

[188] S.J. Williamson and L. Kaufman 1981 *J. Magn. Magn. Mat.* **22** 129-201.

[189] SJ Williamson, G Romani, L Kaufman and I Modena (1983) Biomagnetism - an interdisciplinary approach *NATO ASI Series* **66** 129-139

[190] X Xu, D Brining, A Rafiq, J Hayes and JDZ Chen (2005) Effects of enhanced viscosity on canine gastric and intestinal motility *J Gastroenterol Hepatol* **20** 387-394

[191] H Zhu and JDZ Chen (2004) Gastric distension alters frequency and regularity but not amplitude of the gastric slow wave *Neurogastroenterol Motil* **16** 745-752